

**Regionalization of a Global Climate Change  
Scenario for the Bay of Bengal under Special  
Consideration of Rossby Waves and Coastal  
Kelvin Waves**

Dissertation  
with the aim of achieving a doctoral degree  
at the Faculty of Mathematics, Informatics and Natural Sciences  
Department of Earth Sciences  
at Universität Hamburg

Submitted by Zheen Zhang

Hamburg, 2020

Accepted as Dissertation at the Department of Earth Sciences

Day of oral defense: 14.10.2020

Reviewers: PD Dr. Thomas Pohlmann  
Dr. Bernhard Mayer

Chair of the Subject Doctoral Committee: Prof. Dr. Gajewski  
Dean of Faculty of MIN: Prof. Dr. Heinrich Graener

## Abstract

A projected forecast of hydrographic physical parameters and their variabilities in the Bay of Bengal (BoB) is performed for the 21st century by employing a dynamic downscaling approach using the Hamburg Shelf Ocean Model (HAMSOM). The investigation is based on the high emissions pathway, RCP8.5 scenario. In order to evaluate the impact of climate change caused by anthropogenic factors, a supplementary experiment under a pre-industrial control scenario is also performed. The HAMSOM model is driven by outputs from the MPI-ESM, the Earth System Model developed at the Max-Planck-Institute for Meteorology. The open boundary forces, in terms of lateral open boundary forcing, atmospheric forcing, and river discharge, are bias corrected on the monthly climatological scale relative to the World Ocean Atlas (WOA18) climatology, ERA5 of ECMWF, and the global hydrological model WaterGap, respectively. The overall simulation period is from 1951 to 2099, applying the RCP8.5 scenario from 2006 onwards.

The analysis focuses on three aspects of the hydrodynamic conditions in the BoB, i.e., the mechanism of remote forcing modulating interior properties, the oceanic climate change under the RCP8.5 scenario, and the anthropogenic contribution to projected changes. Based on the HAMSOM results under the historical scenario from 1951 to 2005 and other third-party data sets, it is demonstrated that coastal Kelvin waves and associated westward moving Rossby waves play a crucial role in the teleconnection of variations between the equatorial Indian Ocean and the interior BoB. According to the HAMSOM forecast under the RCP8.5 scenario, climate changes of hydrographic parameters generally exhibit significant spatial differences. Compared to the current climate state of 1980-2009, the sea surface temperature in the BoB will rise by 2.55 to 2.91°C on the climatological scale, while the subsurface temperature at a depth of 100m will rise by 0.39 to 1.52°C. The seasonality of temperature will be enhanced both at the surface and subsurface. In contrast, the seasonality of salinity will be enhanced at the surface, but weakened in the subsurface. As a consequence of climate change in temperature and salinity, the stratification strength is enhancing and the pycnocline depth is getting shallower in most areas of the BoB. For the upper ocean circulation, one notable change is the weakening of East Indian Coastal Current in winter, leading in turn also to a weakening of the seasonal variability.

Interestingly, the variabilities of internal coastal Kelvin waves (CKWs) along the coasts show remarkable changes under the RCP8.5 scenario. The occurrence of significant CKWs will generally become more frequent. Correlations between the CKWs and other variables indicate that the intraseasonal variability from the equator is losing influence on the internal CKWs along the eastern boundary, while the local wind is gaining influence. In addition, the HAMSOM results under the pre-industrial control scenario prove that these predicted changes are mainly attributed to the anthropogenic activities.

## Zusammenfassung

Es wurde eine Projektion der hydrografisch-physikalischen Parameter und ihrer Variabilität im Golf von Bengalen (BoB) für das 21. Jahrhundert durchgeführt. Hierfür wurde ein dynamischer Downscaling-Ansatz unter Verwendung des regionalen Hamburg Shelf Ocean Models (HAMSOM) verwendet. Die Untersuchung basiert auf dem RCP8.5-Szenario. Um die Auswirkungen des durch anthropogene Faktoren verursachten Klimawandels zu bewerten, wird ein zusätzliches Experiment unter Verwendung eines vorindustriellen Kontrollszenarios durchgeführt. HAMSOM wird von den Ergebnissen des globalen Erdsystemmodells MPI-ESM angetrieben, einem gekoppeltes Ozean-Atmosphäre-Modell, das am Max-Planck-Institut für Meteorologie entwickelt wurde. Die Bedingungen an den lateralen offenen Rändern, der atmosphärische Antrieb und die Abflussraten von Flüssen werden auf der monatlichen klimatologischen Skala mit Hilfe der Klimatologie des World Ocean Atlas (WOA18), der meteorologischen ERA5-Daten des ECMWF und der Abflussraten des globalen hydrologischen Modells WaterGap bias-korrigiert. Der gesamte Simulationszeitraum reicht von 1951 bis 2099, wobei das RCP8.5-Szenario ab 2006 verwendet wird.

Die Analyse konzentriert sich auf drei Aspekte der hydrodynamischen Bedingungen im BoB: (a) den Mechanismus der Modulation der internen Charakteristika durch Remote-Steuerung, (b) den ozeanischen Anteil des Klimawandels im RCP8.5-Szenario und (c) den anthropogenen Beitrag zu den projizierten Veränderungen. Basierend auf den HAMSOM-Ergebnissen im historischen Szenario von 1951 bis 2005 und anderen Datensätzen von Drittanbietern wird gezeigt, dass die Küsten-Kelvinwellen (CKWs) und die damit verbundenen nach Westen gerichteten Rossby-Wellen eine entscheidende Bedeutung für die Remote-Steuerung von Variationen zwischen dem äquatorialen Indischen Ozean und dem Inneren des BoB haben. Gemäß der HAMSOM-Prognose unter dem RCP8.5-Szenario weisen die Klimaänderungen für verschiedene hydrografische Parameter im Allgemeinen signifikante räumliche Unterschiede auf. Im Vergleich zum aktuellen Klimazustand von 1980-2009 wird die Meeresoberflächentemperatur im BoB im klimatologischen Mittel um  $2,55$  bis  $2,91^{\circ}\text{C}$  steigen, während sich die Temperatur in einer Tiefe von  $100\text{m}$  um  $0,39$  bis  $1,52^{\circ}\text{C}$  erhöhen wird. Die Saisonalität der Temperatur verstärkt sich sowohl an der Meeresoberfläche als auch unterhalb der Oberfläche. Im Gegensatz dazu erhöht sich die Saisonalität des Salzgehalts zwar ebenfalls an der Oberfläche, während sie sich jedoch in der Tiefe abschwächt. Infolge der klimawandelbedingten vertikal unterschiedlichen Änderungen der Temperatur und des Salzgehaltes nimmt die Schichtungsintensität zu und die Pycnoclinitiefe wird in den meisten Bereichen des BoB geringer. Die Zirkulation des oberen Ozeans erfährt ebenfalls eine signifikante Modifikation. Der Ostindische Küstenstrom schwächt sich im Winter ab, was auch zu einer Abschwächung seiner saisonalen Variabilität führt.

Auch die Variabilität der internen CKWs zeigen entlang der Küsten im RCP8.5-Szenario auffällige Veränderungen. Das Auftreten signifikanter CKWs erfolgt im Allgemeinen häufiger. Korrelationen zwischen den CKWs und anderen Variablen deuten darauf hin, dass für die intrasaisonale Variabilität der internen CKWs vom Äquator stammende Signale an Bedeutung verlieren, wenn die Welle entlang der östlichen Berandung nach Norden fortschreitet, während der lokale Wind an Einfluss gewinnt. Die HAMSOM-Ergebnisse für das vorindustrielle Kontrollszenario belegen, dass diese vorhergesagten Veränderungen hauptsächlich auf den anthropogenen

Einfluss auf den Klimawandel zurückzuführen sind.



# Contents

<b>1</b>	<b>Introduction</b>	<b>1</b>
1.1	Motivation and Objectives . . . . .	1
1.2	Physics in the Bay of Bengal . . . . .	2
1.2.1	Meteorology . . . . .	2
1.2.2	General Circulation . . . . .	3
1.2.3	Eddies . . . . .	4
1.2.4	Thermohaline Structure . . . . .	5
1.3	IPCC . . . . .	6
<b>2</b>	<b>Theory and Methods</b>	<b>11</b>
2.1	HAMSOM . . . . .	11
2.1.1	Model Descriptions . . . . .	11
2.1.2	Model Configuration . . . . .	13
2.2	MPI-ESM . . . . .	14
2.3	Forcing Data and Bias Correction . . . . .	16
2.3.1	Lateral Open Boundaries . . . . .	17
2.3.2	Air-sea Interface . . . . .	21
2.3.3	River Discharge . . . . .	27
<b>3</b>	<b>Model Evaluation</b>	<b>33</b>
3.1	Sea Level Anomaly . . . . .	33
3.2	Thermodynamics . . . . .	34
3.3	Flow Field . . . . .	44
<b>4</b>	<b>Results and Discussion</b>	<b>51</b>
4.1	Correlation with External Forcing of Historical Scenario . . . . .	51
4.2	Long-term Trend of RCP8.5 Scenario . . . . .	59
4.2.1	Sea Level Height . . . . .	59
4.2.2	Water Temperature . . . . .	63
4.2.3	Salinity . . . . .	67
4.2.4	Stratification . . . . .	69
4.2.5	Circulation . . . . .	73
4.2.6	Coastal Kelvin Wave . . . . .	74

4.3 Climate Change and Natural Variability . . . . .	85
<b>5 Summary and Conclusions</b>	<b>93</b>
<b>Acknowledgements</b>	<b>96</b>
<b>Bibliography</b>	<b>97</b>

# Chapter 1

## Introduction

### 1.1 Motivation and Objectives

The ocean is an essential component of the Earth's climate system and plays an important role in climate change. Water has a much higher heat capacity than air, and hence, the ocean stores most of the heat energy. The ocean is also a natural carbon sink, absorbing a large amount of human emissions of carbon dioxide. The ability of the ocean to store and transport large amounts of heat, water, and carbon dioxide, in turn, affects properties in the atmosphere via extensive surface processes. Therefore, the investigation of hydrographic physical parameters and oceanic processes is of great importance to climate change studies.

The Bay of Bengal (BoB) and the Andaman Sea are located in the northern Indian Ocean. For simplicity, this region is referred to as BoB in this investigation. One unique geographic feature of this region is that it borders to the east by the Sumatra-Java islands and to the north by a wide continental shelf, which makes it susceptible to equatorial signals carried by Kelvin waves and associated Rossby waves. The BoB is also a well-known region that is significantly affected by the monsoon of South Asia. The oceanic state of the BoB in turn affects the local monsoon system, and further affects the global climate. Wet and dry seasons caused by the monsoon also influence the seasonal freshwater variability of the bay, reflecting a strong link between the ocean and the continent by river discharges. In summary, the unique geographic feature of the BoB, as well as the internal connection between the ocean, the atmosphere, and the land, inspire the investigation of this region from the perspective of geoscience.

More than one billion people live along the coastline of the BoB, and the coastal population density is increasing. Compared to the seas near developed countries, the research on the BoB is relatively scarce, especially with respect to regional climate change projections. Although man-made global warming is already an established fact, and the scientific community generally believes that greenhouse gas emissions need to be controlled to slow down the rate of warming, the current emissions are still at a high level and may continue to rise due to various reasons. For people living in this area, a comprehensive study of hydrographic physical parameters and their variabilities, especially for the oceanic response under the high emissions pathway, is required.

The major objective of this investigation is to answer three questions. First, how do the equa-

torial signals modulate variabilities of oceanic parameters in the BoB? Due to the geographic configuration of the bay, the hydrodynamic conditions in this region should consider the coastal Kelvin waves and associated Rossby waves. The study of the first question helps to understand the mechanism related to observed variabilities. Second, what is the projected climate change in the BoB under the high emissions pathway, in terms of sea level height, temperature, salinity, stratification, flow field, as well as coastal Kelvin waves? It is predicted that the ocean is warming on the global scale under the high emissions pathway. However, the spatial differences under climate change of hydrodynamic variables, as well as the vertical structure and the seasonality, remain unclear. This investigation is therefore expected to comprehensively describe the projected hydrodynamic conditions of the BoB. Third, is the projected climate change a man-made or natural phenomenon? A common argument of climate skeptics is that climate change is a natural process, rather than a consequence induced by human activities. And thus, it is also an important goal of this investigation to evaluate the natural variability of the BoB climate system.

## 1.2 Physics in the Bay of Bengal

### 1.2.1 Meteorology

The monsoon of South Asia is one of the most anticipated weather phenomena for the Indian subcontinent and the BoB. Satellite and conventional observations support that the monsoon is a manifestation of seasonal migration of the Intertropical Convergence Zone (ITCZ; [Sikka and Gadgil, 1980](#); [Gadgil, 2003](#)). A model study indicates that the thermal and momentum forcing of the Tibetan Plateau significantly influences the transition of the Indian monsoon precipitation by modulating the mid-tropospheric circulation ([Sato and Kimura, 2007](#)).

The Indian summer monsoon originates from the southern Indian Ocean and bifurcates into the Arabian Sea branch and the BoB branch, bringing a lot of rain to the Indian subcontinent. The spatial feature on the intraseasonal scale of rainfall during the summer season is significantly affected by the low-pressure systems ([Goswami, 1987](#); [Hunt and Fletcher, 2019](#)), the stratosphere-troposphere interaction ([Fadnavis and Chattopadhyay, 2017](#)), the Madden Julian Oscillation ([Pai et al., 2011](#); [Mishra et al., 2017](#)), and the occurrence of active and break phases of the Indian summer monsoon ([Krishnamurthy and Shukla, 2000](#); [Rajeevan et al., 2010](#)). The variability of the Indian summer monsoon is influenced by the El Nino-Southern Oscillation (ENSO) via the Walker circulation ([Webster and Yang, 1992](#)). The relationship between the Indian summer monsoon and ENSO exhibits decadal changes ([Krishnamurthy and Goswami, 2000](#); [Wang et al., 2001](#); [Wu et al., 2012](#)). Historical records show a weakening in the relationship between the Indian summer monsoon and ENSO since the 1970s ([Kumar et al., 1999](#)). The Indian Ocean Dipole (IOD) mode plays a remarkable role in the relationship between the Indian monsoon rainfall and ENSO ([Ashok et al., 2001, 2003, 2004](#)), resulting in more complicated interannual features of the monsoon system. Besides the ENSO and IOD, the surface temperature/pressure pattern in the South China Sea also plays an important role for the spatial distribution of Indian summer monsoon rainfall ([Sinha et al., 2019](#)). In summary, the Indian monsoon is coupled with the climate system of many regions of the world, and hence is an important component of the

global climate system.

The hydrographic conditions of the BoB are significantly affected by the monsoon system. The monsoon has a large impact on the thermohaline structure of the northern BoB through the air-sea interaction (Bhat et al., 2001). The formation of the barrier layer in the northern bay is highly correlated with the arrival of a monsoon-associated freshwater plume (Vinayachandran et al., 2002). Upper ocean circulation, vertical exchange, and water characteristics in the BoB are significantly influenced by momentum input from the monsoon (Shetye et al., 1991, 1996; Vecchi and Harrison, 2002; Li et al., 2017a,b). Monsoon-induced currents will be introduced in detail in the next subsection.

### 1.2.2 General Circulation

The surface circulation system in the BoB consists of the northwestern gyre, the large gyre in the southern BoB, and the Andaman gyre (Varkey et al., 1996). The upper ocean circulation in the BoB exhibits seasonal variations due to the monsoon system (Potemra et al., 1991; Schott and McCreary, 2001; Schott et al., 2009; Paul et al., 2009). Hydrographic investigations off the east coast of India revealed the East Indian Coastal Current (EICC), which is the western boundary current of the BoB (Shetye et al., 1991, 1993, 1996). A model simulation driven by climatological monthly wind stress indicates that the prominent features of the BoB circulation are an anticyclonic gyre with a poleward EICC during February-May, and an equatorward EICC during October-December (Vinayachandran et al., 1996). In addition to the seasonal feature induced by the monsoon momentum transfer, the monsoon precipitation also modulates the circulation in the BoB. During the monsoon season from July to September, an enormous quantity of freshwater is discharged at the head bay region (Varkey et al., 1996). The freshwater plume along the coast significantly modulates the salinity gradients in the northern bay, affecting the surface current structure (Chamarthi et al., 2008; Jana et al., 2018; Dandapat et al., 2020). In summary, the upper ocean circulation in the BoB is a comprehensive result of the interaction between wind driven circulation and density driven circulation.

Numerical experiments for the Indian Ocean show that the circulation at any point is decided by both, local forcing and remote forcing (Shankar et al., 2002). In addition to the local monsoon, remote forcing from the equator impacts the ocean circulation in the BoB, due to signals passing through the Andaman Sea, revealing the importance of Rossby waves and coastal Kelvin waves on the interannual variability of BoB currents (Potemra et al., 1991; Yu et al., 1991; McCreary et al., 1993, 1996). The seasonal reversal of the EICC is significantly influenced by remotely forced planetary waves, resulting in possible lags between the EICC and the local monsoon (Eigenheer and Quadfasel, 2000). In addition, the Andaman and Nicobar Islands, as well as the eastern border of the Andaman Sea, significantly alter the circulation in the BoB (Chatterjee et al., 2017).

During the summer monsoon, the Southwest Monsoon Current brings saltier water from the evaporative Arabian Sea into the BoB, in contrast, during the winter monsoon, the Northeast Monsoon Current transports fresher water from the BoB to the Arabian Sea, maintaining the salinity balance of the northern Indian Ocean (Vinayachandran et al., 1999; Jensen, 2001; Lee et al., 2016; Sanchez-Franks et al., 2019). Subsurface flow from the Arabian Sea to the BoB

during the winter monsoon is proven by model works and observations (Wijesekera et al., 2015; Gordon et al., 2016). Noteworthy, the equatorial undercurrent also contributes to the water exchange between the BoB and the western equatorial Indian Ocean (Todd, 2020).

### 1.2.3 Eddies

Mesoscale eddies are ubiquitous in the oceans and play a crucial role in water property transport and energy cascading (Chelton et al., 2011). Rich mesoscale eddy activities in the BoB are detected by in situ observations (Hacker et al., 1998; Babu et al., 2003; Kumar et al., 2004, 2007; Vidya and Kumar, 2013; Gordon et al., 2017). The features and variabilities of BoB eddies are also widely discussed by using satellite data (Nuncio and Kumar, 2012; Chen et al., 2012, 2018; Cheng et al., 2013; Dandapat and Chakraborty, 2016; Busireddy et al., 2018). Chen et al. (2012) statistically assessed eddy activities in the BoB, showing that eddies tend to propagate southwestward, quasi-westward, and northwestward in the northern, central, and southern BoB. Eddies formed in the north have a longer lifetime and a smaller radius than eddies formed in the south (Chen et al., 2012). Cheng et al. (2013) revealed that intraseasonal variability of sea surface height in the central BoB is to some extent attributed to eddy activities.

The generation mechanism of eddies is related to their formation places, which reflects different eddy features in different places of the BoB. The eddy generation near the western boundary is believed to be related to the EICC baroclinic instability (Kurien et al., 2010; Cheng et al., 2013; Chen et al., 2018). In contrast, in the eastern and central basin, westward moving Rossby waves and coastal Kelvin waves play a dominant role in the eddy generation (Sreenivas et al., 2012; Chatterjee et al., 2017; Cheng et al., 2018). External signals from the equatorial ocean carried by coastal Kelvin waves and associated westward moving Rossby waves alter the variabilities of sea level height and thermocline depth in the BoB by affecting the mesoscale eddy generation (Sreenivas et al., 2012). Besides, the Ekman pumping induced by local wind also significantly contributes to the eddy kinetic energy in the eastern basin (Chen et al., 2018).

Mesoscale eddies exhibit extensive connections and interactions with other geophysical processes and variables. A previous study using satellite altimetry and Argo floats revealed that mesoscale eddies have a significant impact on the temperature and salinity structure in both the horizontal and the vertical (Dandapat and Chakraborty, 2016). Nuncio and Kumar (2012) reported an undulating vertical thermohaline structure along the western boundary of the BoB, which is caused by eddies rather than internal waves. Eddies play an important role in the heat and salt transport in the BoB, especially for the depth range from 200m to 400m (Gonaduwege et al., 2019). According to satellite altimeter observations, eddies in the BoB tend to propagate to the western basin (Chen et al., 2012), implying a potential interaction between the western-boundary current and mesoscale eddies. The EICC is also found to be an important contributor to the seasonal modulation of the eddy-induced transport in the western BoB (Gonaduwege et al., 2019). A regional coupled model simulation indicated the southwestern BoB is a hot spot for the momentum exchange between the monsoonal winds and the surface currents, which is significantly affected by local eddy activities (Seo et al., 2019). Gordon et al. (2017) reported that a surface eddy dived into the thermocline under the influence of a tropical cyclone, demonstrating the role of eddies for vertical motions. Eddies affect tropical cyclones in reverse. They

will be enhanced after interacting with a warm eddy, while weakened when affected by a cold gyre (Anandh et al., 2020).

#### 1.2.4 Thermohaline Structure

The vertical thermohaline structure in the BoB is significantly affected by abundant freshwater carried by the summer monsoon, especially in the northern bay (Sprintall and Tomczak, 1992; Murty et al., 1992, 1996; Bhat et al., 2001; Vinayachandran et al., 2002; Shroyer et al., 2020). The effects of a large amount of rain and river discharge are gradually reversed before the next summer monsoon, resulting in a notable annual cycle in the thermohaline fields. According to the Bay of Bengal Monsoon Experiment (Bhat et al., 2001), in the northern bay, the upper layer can be divided into a mixed layer, a barrier layer, and a thermocline. In contrast, the upper layer above 60m in the southern bay is relatively well mixed. Low salinity water induced by freshwater input in the northern bay is of great importance for determining the local ocean barrier layer and mixed layer depth, further influencing the ocean-atmosphere coupling (Lukas and Lindstrom, 1991; Howden and Murtugudde, 2001; Vinayachandran et al., 2002; Montégut et al., 2007; Li et al., 2018; Kido and Tozuka, 2017; Kido et al., 2019b,a). Vertical processes play a prominent role in the near surface salinity budget in the BoB (Wilson and Riser, 2016). In the coastal regions under the influence of freshwater plumes, the thin mixed layer occasionally results in a temperature inversion (Vinayachandran and Kurian, 2007). The freshwater persists in the northern bay for 3-5 months starting around July, suppressing the mixing for several months (Thakur et al., 2019).

The overall thermohaline fields are highly associated with the cyclonic and anticyclonic circulation patterns, and in turn to the local monsoon system. Field measurements show continuous upsloping/downsloping patterns of thermohaline structures in the BoB, suggesting the effect of propagating waves and eddies (Kumar et al., 2013). Thermohaline fronts that sometimes form in the northern bay during the summer monsoon also show influences of local wind forcing, which is reflected by an offshore transport and thinning of warm and less saline water following the Ekman dynamics (Gopalakrishna et al., 2002). Monsoon-related currents separate the low saline water of the northern bay from the saltier water of the southern bay and thus regulates the near surface stratification (Vinayachandran and Kurian, 2007). The salinity exchange between the BoB and the equatorial Indian Ocean also shows a seasonality associated with the monsoon (Jensen et al., 2016; Trott et al., 2019).

Remote forcing from equatorial oceans also modulates the thermocline variations in the BoB via planetary waves (McCreary et al., 1993, 1996; Girishkumar et al., 2013). Baroclinic Kelvin waves and Rossby waves that are generated remotely by winds in the equatorial Indian Ocean and the eastern BoB, contribute to the intraseasonal oscillations of the thermocline in the central basin (Girishkumar et al., 2013). On the interannual scale, a recent numerical study suggests that the equatorial forcing plays a dominant role in the thermocline variability in the BoB during IOD and ENSO events, especially with respect to their spatial patterns (Pramanik et al., 2019).

### 1.3 IPCC

The Intergovernmental Panel on Climate Change (IPCC; <https://www.ipcc.ch>) is the world leading authority on climate change, producing reports that contribute to the work of the United Nations Framework Convention on Climate Change. In this investigation, the Working Group I contribution to the Fifth Assessment Report of the IPCC “Climate Change 2013: The Physical Science Basis” (IPCC, 2013), is the primary guidelines for climate change related subjects. In this section, information related to this investigation from the IPCC is introduced. Unless otherwise stated, the information is summarized from IPCC (2013).

Global warming is unequivocal. Since the 1950s, many of the observed changes in atmosphere, ocean, and cryosphere are unprecedented over the last centuries to millennia. The values of anthropogenic carbon dioxide, global mean sea level, upper ocean heat content, and the salinity contrast between regions have increased since the 1950s (Figure 1.1; Khatiwala et al., 2009; Church et al., 2011; Domingues et al., 2008). It is virtually certain that the upper ocean above 700m has warmed from 1971 to 2010 (Gouretski and Koltermann, 2007; Levitus et al., 2009). Ocean warming accounts for about 93% of the increase in the Earth’s energy inventory between the 1950s and the 2000s (Church et al., 2011; Levitus et al., 2012). Noteworthy, human influence has been detected in global ocean warming (Gleckler et al., 2012). It could be shown that human activity is the dominant cause of observed warming since the mid-20th century with 95% certainty.

The atmospheric concentrations of greenhouse gases have increased to levels unprecedented in at least the last eight hundred thousand years. For example, carbon dioxide concentrations have increased by 40% since the pre-industrial time principally caused by fossil fuel emissions and net land use change emissions. Continuous emissions of greenhouse gases will cause further warming and changes in all components of the climate system. The greenhouse gas concentration scenarios called Representative Concentration Pathways (RCPs) are adopted in the Coupled Model Intercomparison Project Phase 5 (CMIP5; Moss et al., 2010; van Vuuren et al., 2011). RCP scenarios include assumptions of future emissions and concentrations of greenhouse gases, aerosols, and chemically active gases, as well as land use. Four RCPs (Figure 1.2 top left) produced from Integrated Assessment Models were selected and used in the fifth IPCC assessment as a basis for climate predictions and projections.

- RCP2.6: One pathway where radiative forcing peaks at approximately  $3Wm^{-2}$  before 2100 and then declines;
- RCP4.5: One intermediate stabilization pathway where radiative forcing is stabilized at approximately  $4.5Wm^{-2}$  after 2100;
- RCP6.0: One intermediate stabilization pathway where radiative forcing is stabilized at approximately  $6.0Wm^{-2}$  after 2100;
- RCP8.5: One high emissions pathway where radiative forcing reaches values greater than  $8.5Wm^{-2}$  by 2100.

Surface air temperature changes simulated by CMIP5 concentration-driven experiments are shown in Figure 1.2 (bottom left and maps). Climate models have improved since the fourth

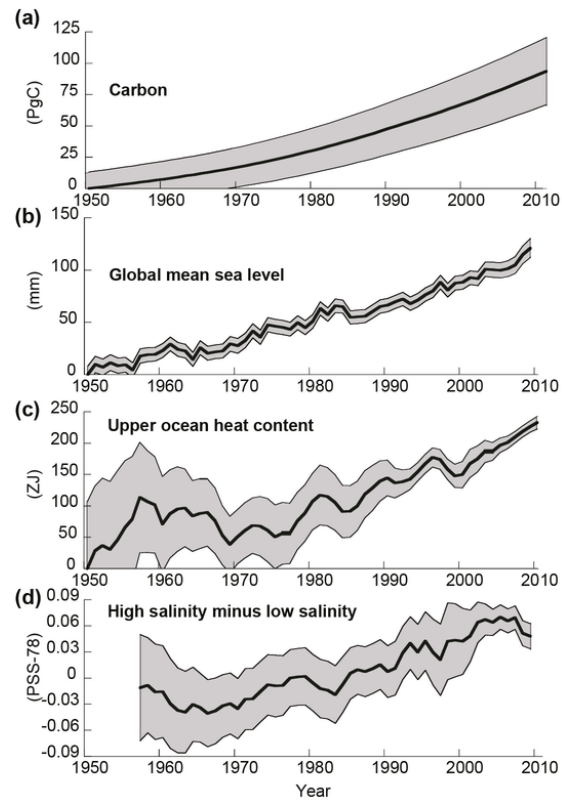


Figure 1.1: Times series of observed changes in large-scale ocean climate properties. Reprinted from the [IPCC \(2013\)](#)

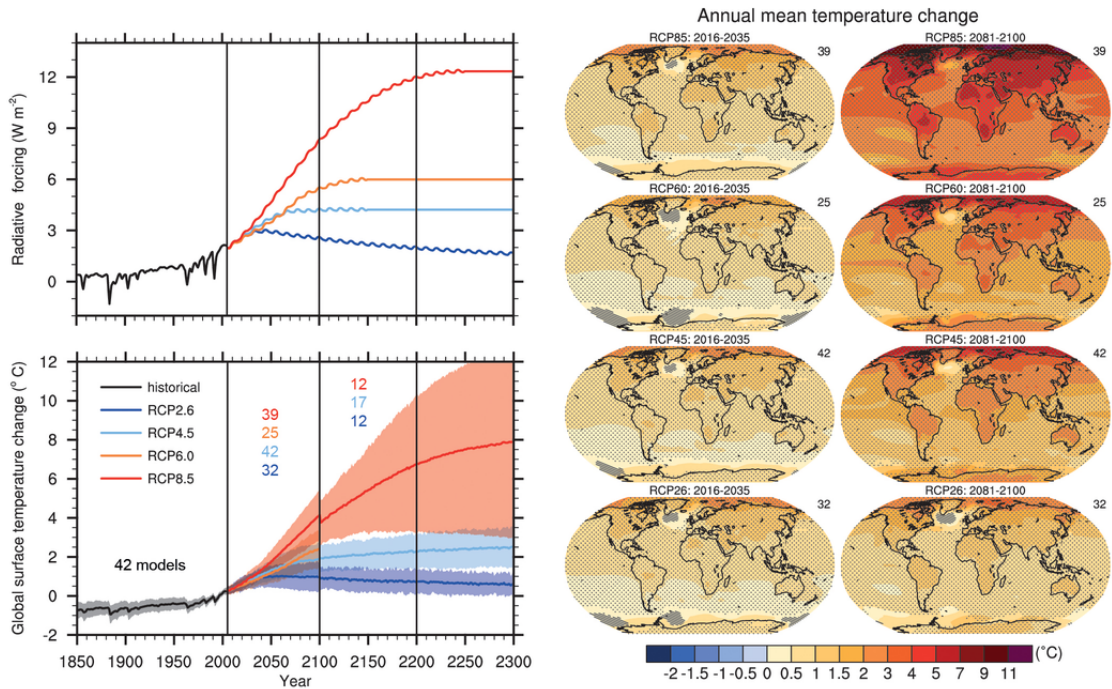


Figure 1.2: Total global mean radiative forcing for the four RCP scenarios (top left). Time series of global annual mean surface air temperature anomalies relative to 1986-2006 from CMIP5 experiments (bottom left). Multi-model ensemble average of annual mean surface air temperature change compared to 1986-2006 (right). Hatching indicates regions where the multi-model mean signal is less than one standard deviation of internal variability. Reprinted from the [IPCC \(2013\)](#)

Assessment Report. For instance, the more rapid warming since the mid-20th century and the cooling immediately following large volcanic eruptions are now well reproduced. The projected warming of the global mean surface for 2081-2100 relative to 1986-2005 is  $0.3^{\circ}\text{C}$  to  $1.7^{\circ}\text{C}$  for RCP2.6,  $1.1^{\circ}\text{C}$  to  $2.6^{\circ}\text{C}$  for RCP4.5,  $1.4^{\circ}\text{C}$  to  $3.1^{\circ}\text{C}$  for RCP6.0, and  $2.6^{\circ}\text{C}$  to  $4.8^{\circ}\text{C}$  for RCP8.5, respectively. With respect to the global water cycle, changes in response to the warming over the 21st century will not be uniform and the contrast in precipitation between wet and dry regions and between wet and dry seasons will increase in most regions.

Looking at the future regional climate change, CMIP5 models project an increase in mean precipitation and its interannual variability and extremes for Southern Asia. The monsoon circulation in India is projected to be weakened in the future. In the BoB, enhanced summer monsoon precipitation and increased rainfall extremes by landfalling cyclones are projected. However, the interannual variance of the IOD mode remains nearly unchanged as atmospheric feedback and zonal wind variance weaken ([Zheng et al., 2013](#)).



# Chapter 2

## Theory and Methods

### 2.1 HAMSOM

#### 2.1.1 Model Descriptions

The Hamburg Shelf Ocean Model (HAMSOM; [Backhaus, 1985](#); [Pohlmann, 1996, 2006](#); [Große et al., 2015](#)) is used to perform the dynamical downscaling run in the BoB from 1951 to 2099. The HAMSOM is a three-dimensional baroclinic primitive equation model based upon a semi-implicit numerical scheme. In contrast to an explicit scheme, the semi-implicit scheme is faster and allows the simulation of the shelf and the deep ocean regions together without being limited by stability considerations for the free surface ([Backhaus, 1985](#)). The underlying primitive equations are defined in  $z$ -coordinates on an Arakawa C-grid.

The basic equations are as follows,

$$\frac{\partial u}{\partial t} + u \frac{\partial u}{\partial x} + v \frac{\partial u}{\partial y} + w \frac{\partial u}{\partial z} - fv + \frac{1}{\rho} \frac{\partial p}{\partial x} = \frac{\partial}{\partial x} \left( A_{Ih} \frac{\partial u}{\partial x} \right) + \frac{\partial}{\partial y} \left( A_{Ih} \frac{\partial u}{\partial y} \right) + \frac{\partial}{\partial z} \left( A_{Iv} \frac{\partial u}{\partial z} \right) + F_x \quad (2.1)$$

$$\frac{\partial v}{\partial t} + u \frac{\partial v}{\partial x} + v \frac{\partial v}{\partial y} + w \frac{\partial v}{\partial z} + fu + \frac{1}{\rho} \frac{\partial p}{\partial y} = \frac{\partial}{\partial x} \left( A_{Ih} \frac{\partial v}{\partial x} \right) + \frac{\partial}{\partial y} \left( A_{Ih} \frac{\partial v}{\partial y} \right) + \frac{\partial}{\partial z} \left( A_{Iv} \frac{\partial v}{\partial z} \right) + F_y \quad (2.2)$$

$$\frac{\partial p}{\partial z} + g\rho = 0 \quad (2.3)$$

$$\frac{\partial u}{\partial x} + \frac{\partial v}{\partial y} + \frac{\partial w}{\partial z} = 0 \quad (2.4)$$

$$\frac{\partial S}{\partial t} + u \frac{\partial S}{\partial x} + v \frac{\partial S}{\partial y} + w \frac{\partial S}{\partial z} = \frac{\partial}{\partial x} \left( A_{Mh} \frac{\partial S}{\partial x} \right) + \frac{\partial}{\partial y} \left( A_{Mh} \frac{\partial S}{\partial y} \right) + \frac{\partial}{\partial z} \left( A_{Mv} \frac{\partial S}{\partial z} \right) + R_S \quad (2.5)$$

$$\frac{\partial T}{\partial t} + u \frac{\partial T}{\partial x} + v \frac{\partial T}{\partial y} + w \frac{\partial T}{\partial z} = \frac{\partial}{\partial x} \left( A_{Mh} \frac{\partial T}{\partial x} \right) + \frac{\partial}{\partial y} \left( A_{Mh} \frac{\partial T}{\partial y} \right) + \frac{\partial}{\partial z} \left( A_{Mv} \frac{\partial T}{\partial z} \right) + R_T \quad (2.6)$$

where  $u$ ,  $v$ , and  $w$  are the velocity in  $x$ ,  $y$ , and  $z$  direction, respectively;  $g$  is the gravitational acceleration;  $p$  the the pressure;  $\rho$  is the seawater density calculated by the UNESCO equation of state ([Fofonoff and Millard, 1983](#));  $S$  is the salinity and  $T$  is the temperature.  $F_x$  and  $F_y$  mean external forces in  $x$  and  $y$  direction, respectively.  $R_S$  means external sources of salinity.

$R_T$  means external sources of temperature.  $f = 2\Omega\sin(\phi)$  is the Coriolis parameter, where  $\Omega$  is the angular velocity of earth and  $\phi$  is the latitude.  $A_{Ih}$  and  $A_{Iv}$  are the horizontal and vertical momentum exchange coefficients.  $A_{Mh}$  and  $A_{Mv}$  are the the horizontal and vertical eddy diffusion coefficients.

The advection of temperature and salinity is performed in the interior domain by applying the Lax-Wendroff method. The horizontal and vertical eddy viscosity are defined according to the Smagorinsky diffusivity and the Kochergin scheme as follows (Pohlmann, 1996, 2006; Kochergin, 2013),

$$A_{Mh} = c_0 \Delta x \Delta y \sqrt{\left(\frac{\partial u}{\partial x}\right)^2 + 0.5 \left(\frac{\partial v}{\partial x} + \frac{\partial u}{\partial y}\right)^2 + \left(\frac{\partial v}{\partial y}\right)^2} \quad (2.7)$$

$$A_{Mv} = \left( c_m^2 h_m^2 \sqrt{\left(\frac{\partial u}{\partial x}\right)^2 + \left(\frac{\partial v}{\partial z}\right)^2 + \frac{1}{S_M} \frac{g}{\rho} \frac{\partial \rho}{\partial z}} \right) / S_M \quad (2.8)$$

where  $c_0 = 0.15$  is a non-dimensional parameter,  $\Delta x$  and  $\Delta y$  are the grid distance at  $x$  and  $y$  direction respectively;  $c_m = 0.05$  is a free constant;  $h_m$  is the mixed layer thickness;  $S_M$  is the Schmidt-Prandtl number.

Heat and freshwater fluxes through the air-sea interface significantly affect water properties in the BoB, for instance, high-frequency variations in the BoB are largely induced by the atmospheric forcing. For the air-sea heat flux, parametrizations used in HAMSOM are as follows,

$$Q_{sw} = Q_{sw0}(1 - \alpha_c - \beta_c C^2)(1 - \alpha_{alb}) \quad (2.9)$$

$$Q_{lw} = e_w \sigma T_w^4 - e_a \sigma T_a^4 \quad (2.10)$$

$$Q_s = \rho_a C_a C_s \left| \vec{W} \right| (T_a - T_w) \quad (2.11)$$

$$Q_l = C_l I_v \left| \vec{W} \right| (q_a - q_s) \quad (2.12)$$

where  $Q_{sw}$ ,  $Q_{lw}$ ,  $Q_s$ , and  $Q_l$  represent short-wave radiation, long-wave radiation, sensible heat flux, and latent heat flux, respectively.

The actual total short-wave radiation  $Q_{sw}$  is mainly determined by the short-wave radiation without cloudiness, the effect of cloudiness, and the surface albedo (Budyko, 1974).  $Q_{sw0}$  is the clear-sky short-wave radiation at sea surface depending on latitude and geographic local time.  $C$  is the cloud cover in fractions of one unit.  $\alpha_c = 0.4$  and  $\beta_c = 0.38$  are dimensionless coefficients.  $\alpha_{alb} = 0.06$  is the surface albedo of seawater.

The outgoing long-wave radiation  $Q_{lw}$  follows Stefan-Boltzmann law.  $\sigma = 5.6704 \times 10^8 \text{ W m}^{-2} \text{ K}^{-4}$  is the Stefan-Boltzmann constant.  $e_w = 0.97$  is the emissivity of water,  $e_a = 0.7855(1 + 0.2232C^{2.75})$  is the emissivity of air considering the effect of cloud cover  $C$  (Maykut and Church, 1973).  $T_w$  and  $T_a$  are the absolute temperature of surface seawater and air, respectively.

The sensible heat flux  $Q_s$  is estimated by an aerodynamic parametrization (Friehe and Schmitt, 1976).  $\rho_a$  is the air density.  $C_a = 1015 \text{ J/kgK}$  is the specific heat capacity of air.  $C_s$  is the exchange coefficient for sensible heat, which is calculated by an empirical function (Kondo, 1975; Pettenuzzo et al., 2010).  $\vec{W}$  is the wind vector.

The latent heat flux basically is the heat transfer due to vaporization and condensation at the sea surface (Gill, 1982).  $C_l$  is the exchange coefficient for latent heat, which is calculated by

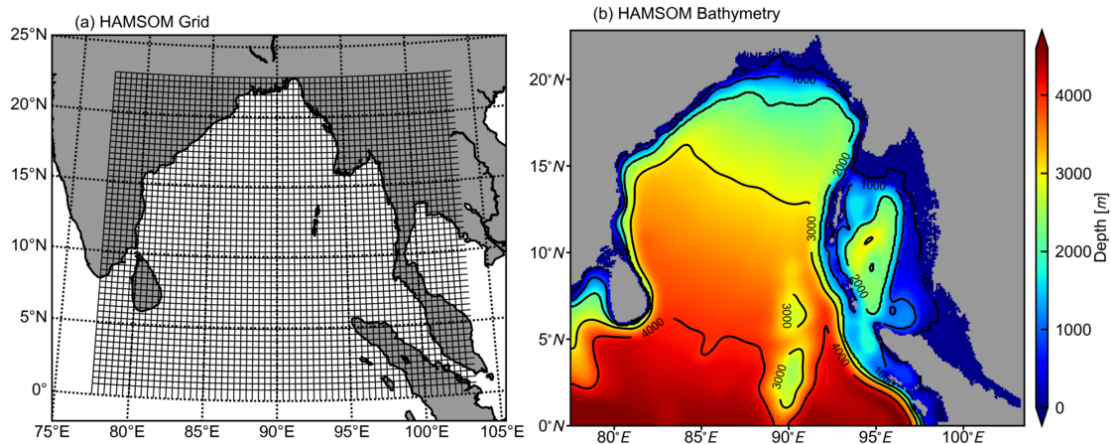


Figure 2.1: The grid configuration (a) and the bathymetry used in HAMSOM experiments. Every 5th grid line is shown.

bulk empirical formulas (Kondo, 1975; Pettenuzzo et al., 2010).  $I_v$  is the heat of vaporization of water.  $q_a$  and  $q_s$  are the absolute humidity of air and the saturated absolute humidity of sea surface water, respectively.

The net surface heat flux from air to sea is  $Q_{net} = Q_{sw} - Q_{lw} + Q_s + Q_l$ .

### 2.1.2 Model Configuration

The model domain (Figure 2.1) covers the Bay of Bengal and the Andaman Sea, ranging zonally from 77.5°E to 103.5°E and meridionally from 0 to 22.83°N. The horizontal resolution is set to 5°x5'. The model assumes an  $\beta$ -plane in horizontal, and the horizontal distance between grid points is approximately 9km in the research region (Figure 2.1a). The first baroclinic Rossby radius of deformation is approximately 60km-150km, which means the model is eddy-permitting. The bathymetry (Figure 2.1b) is derived from SRTM30\_PLUS (Becker et al., 2009). A total of 58 model layers are specified in vertical. The vertical resolution gradually changes from 5m in the upper ocean to 200m in the deep ocean (Figure 2.2).

External forcing data employed in HAMSOM in this study are as follows. Sea surface height, water temperature, and salinity, are monthly prescribed at the open lateral boundaries. Air temperature, cloud cover, precipitation, specific humidity, air pressure, wind stress, and wind speed, are six-hourly prescribed at the air-sea interface. The freshwater of rivers is also six-hourly prescribed by adding an additional water volume to the river points. Tides are not included.

To investigate the future ocean state and related processes of the BoB under a high emissions pathway, an experiment (named as RCP85) is run with the RCP8.5 scenario forcing of MPI-ESM. To further isolate the impact of climate change caused by high emissions, a supplementary experiment (named as piCon) under the pre-industrial control scenario is also performed. The MPI-ESM is the outer model in this investigation and will be described in detail in the following chapter. These two experiments are run from 1951 to 2099 with 3 minutes time step and daily averaged output. For the RCP85 run, it should be noted that before 2006, the model is driven by

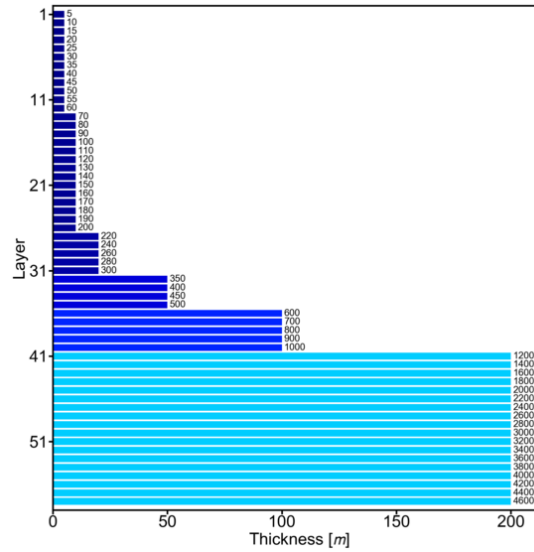


Figure 2.2: The vertical layer configuration used in HAMSOM experiments. Numbers on the right side of bars indicate the cumulative depth.

the historical scenario. However, to simplify the naming, this run is uniformly named as RCP85.

## 2.2 MPI-ESM

For the regional downscaling investigation, the outer global model is MPI-ESM, the Earth System Model developed at the Max-Planck-Institute for Meteorology (Mauritsen et al., 2012; Giorgetta et al., 2013). The MPI-ESM couples the atmosphere, ocean, and land surface through the exchange of energy, momentum, water, and carbon dioxide, and is used in the CMIP5 study in a series of climate change experiments (Figure 2.3). The results of MPI-ESM indicate that the global warming starting from climatological conditions of 1850 to that of 2080-2100 ranges from  $1.5^{\text{circ}}C$  under the RCP2.6 scenario to  $4.4^{\text{circ}}C$  under the RCP8.5 scenario, while the patterns of temperature and precipitation change are nearly independent of the global warming (Giorgetta et al., 2013). This model system has various configurations differing in resolution. This investigation uses the results of the mixed resolution version (MPI-ESM-MR). The MPI-ESM data can be accessed on the Earth System Grid Federation website (<https://esgf-node.llnl.gov/projects/cmip5/>).

The atmosphere component of MPI-ESM, ECHAM6, is the sixth generation of the atmospheric general circulation model ECHAM (Stevens et al., 2013). A brief historical overview of ECHAM can be found in Stevens et al. (2013). ECHAM6 is configured to run at different resolutions. The mixed resolution ECHAM6 runs at an operational resolution of T063, denoting a triangular truncation of the spherical harmonics to 63 wavenumbers in horizontal. The mixed resolution version has 95 hybrid layers in vertical (Figure 2.4). This higher vertical resolution configuration systematically reduces temperature biases in the upper troposphere.

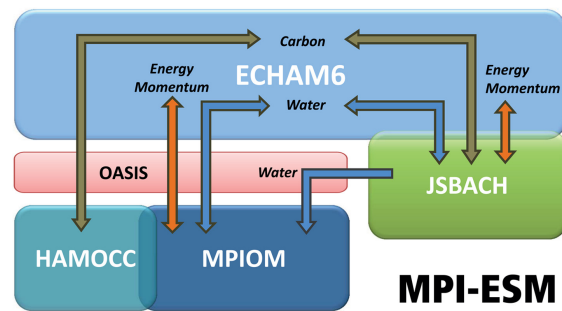


Figure 2.3: Schematic view of MPI-ESM. Reprinted from “Climate and carbon cycle changes from 1850 to 2100 in MPI-ESM simulations for the Coupled Model Intercomparison Project phase 5” by [Giorgetta et al. \(2013\)](#)

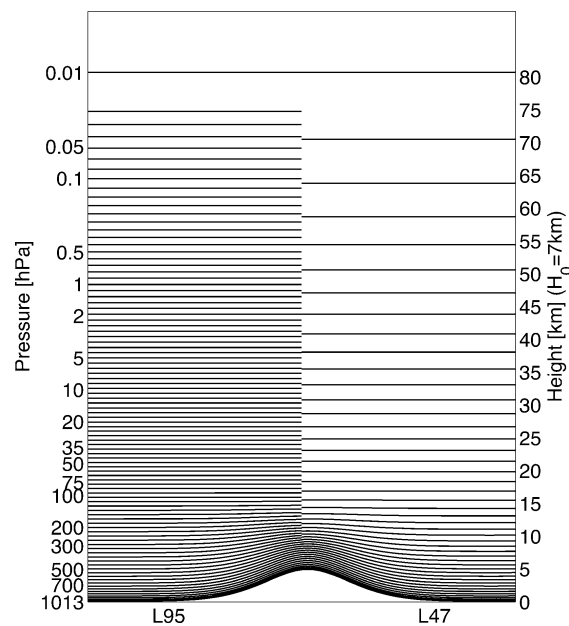


Figure 2.4: The vertical coordinate used in ECHAM6. Reprinted from “Atmospheric component of the MPI-M Earth System Model: ECHAM6” by [Stevens et al. \(2013\)](#)

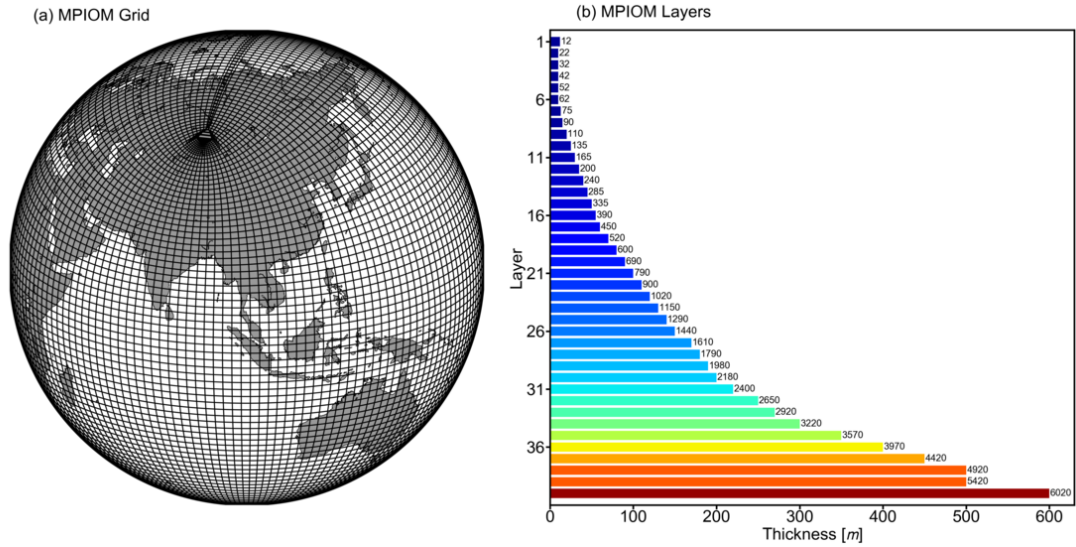


Figure 2.5: The grid configuration (a) and vertical layer configuration (b) used in the mixed resolution version of MPIOM. Numbers on the right side of bars indicate the cumulative depth.

The ocean component of MPI-ESM, MPIOM, is a primitive equation model (Marsland et al., 2003; Jungclaus et al., 2013). The model uses an Arakawa C-grid and z-coordinate with the free surface. One feature of MPIOM is that the model uses a curvilinear orthogonal grid, which allows for a variety of configurations. By selecting different polar locations, the grid size near the poles can become finer. For this mixed resolution configuration, triple poles are set over North America, Antarctica, and Siberia (Figure 2.5a). Forty layers are set in vertical (Figure 2.5b).

## 2.3 Forcing Data and Bias Correction

The forcing used to drive the regional downscaling model HAMSOM is extracted from MPI-ESM-MR. As stated earlier, two experiments are performed. Therefore, the related forcing data are extracted from the corresponding scenario of MPI-ESM-MR. For the RCP85 run, the forcing of the period 1951-2005 is extracted from the historical scenario, while the period 2006-2099 is extracted from the RCP8.5 scenario. For the piCon run, the forcing of the whole period 1951-2099 is extracted from the pre-industrial control scenario. In this chapter, the forcing extracted from MPI-ESM-MR for these two experiments will be directly labeled as RCP85 and piCon, respectively. In order to correct the systematic error in the MPI-ESM-MR results, A bias correction is applied on the monthly climatology scale for these forcing data. In the following, the bias-corrected results will be labeled as RCP85\_cor and piCon\_cor, respectively.

### 2.3.1 Lateral Open Boundaries

The simulated domain is surrounded by Sri Lanka, India, Bangladesh, Myanmar, Thailand, and Malaysia. In the east, the Andaman Sea connects the South China Sea through the Strait of Malacca. However, this strait is not regarded as an open boundary in our modeling because it is narrow and shallow, and the water exchange through this strait is negligible. The deep tropical Indian Ocean affects the simulated domain through the southern boundary. The western boundary is the passage connecting the BoB and the Arabian Sea. There is a natural bridge called Adam Bridge or Rama's Bridge between Sri Lanka and India, which hinders the water exchange between the BoB and the Arabian Sea through the Palk Strait, so this strait is also closed in the configuration. Therefore, the simulated domain can only receive oceanic information from the equatorial Indian Ocean and the Arabian Sea through the southern and western boundaries.

Sea level height, temperature, and salinity at lateral boundaries are prescribed monthly and derived from the oceanic part MPIOM (Jungclaus et al., 2013) of MPI-ESM-MR. The MPIOM output is first linearly interpolated to meet the resolution of HAMSOM. Sea level height given by the outer model provides the large-scale barotropic flow field and associated mesoscale eddies. Temperature and salinity prescribed at the lateral boundaries affect the large-scale thermohaline circulation.

Because the climatological seasonal variability of the mesoscale eddy distribution is unstable, the prescribed sea level height is not bias-corrected during forcing data preparation. The dynamic height is calculated during the model run, which is helpful for stabilizing the model by balancing the sea surface height inside and outside the model. Figure 2.6 shows the comparison of the multi-year monthly mean of sea level anomalies at lateral boundaries among AVISO (<https://icdc.cen.uni-hamburg.de/en/ssh-aviso.html>), RCP85, and piCon. It can be seen that on the scale of multi-year monthly mean, the sea level anomalies given by MPI-OM show a good agreement with the observations in spatial patterns. In January and April, there is a certain difference in the value of anomalies, but the barotropic flow field still keeps consistent with the observations because these differences are imposed at both lateral boundaries, keeping the sea level gradient in a comparable range. Meanwhile, as can be seen from the standard deviation, the intensity of the interannual variability of sea level anomalies given by MPI-OM is also in line with the observations.

Figure 2.7 shows the time-longitude/latitude evolution of the three data sets from 1993 to 2013 along the two boundaries, as well as their corresponding spatial averaged time series. All three data sets exhibit similar seasonal changes. From 1997 to 1998, that is, under the historical scenario, the RCP85 well simulated the peak changes that match very well with the observations (Figure 2.7a, c, g). In general, these comparisons indicate that the sea level height derived from the MPIOM is reliable.

For the temperature and salinity, the World Ocean Atlas (WOA18) climatology is used as a basis for the bias correction. Figure 2.8 shows the comparison of the climatological monthly average of temperature and salinity among the WOA18, RCP85, and piCon at the southern boundary. All three data sets reflect the feature that the salinity is decreasing from west to east in the upper equatorial ocean. Beneath 100m depth, the salinity given by RCP85 is slightly higher than that of WOA18. Overall, this comparison shows that the salinity distribution given

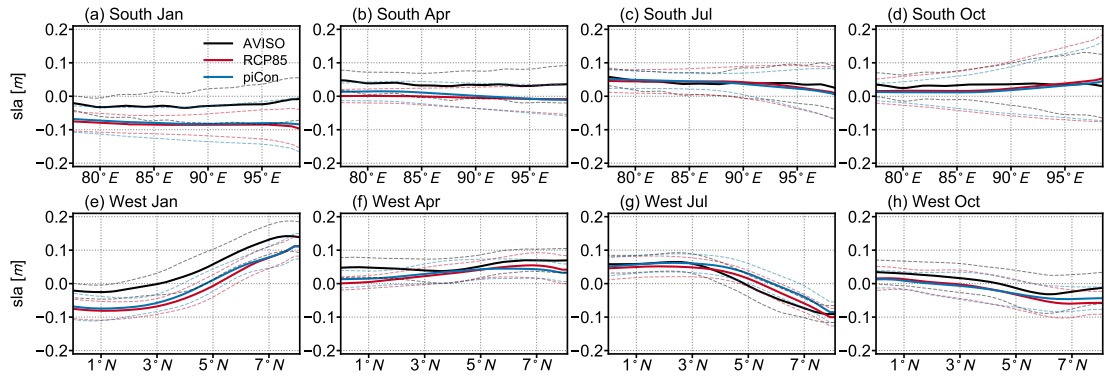


Figure 2.6: Comparison of multi-year (1993-2012) monthly mean of sea level anomalies at southern (a, b, c, d) and western (e, f, g, h) boundaries for AVISO, RCP85, and piCon. Dashed lines with corresponding colors mean their standard deviation.

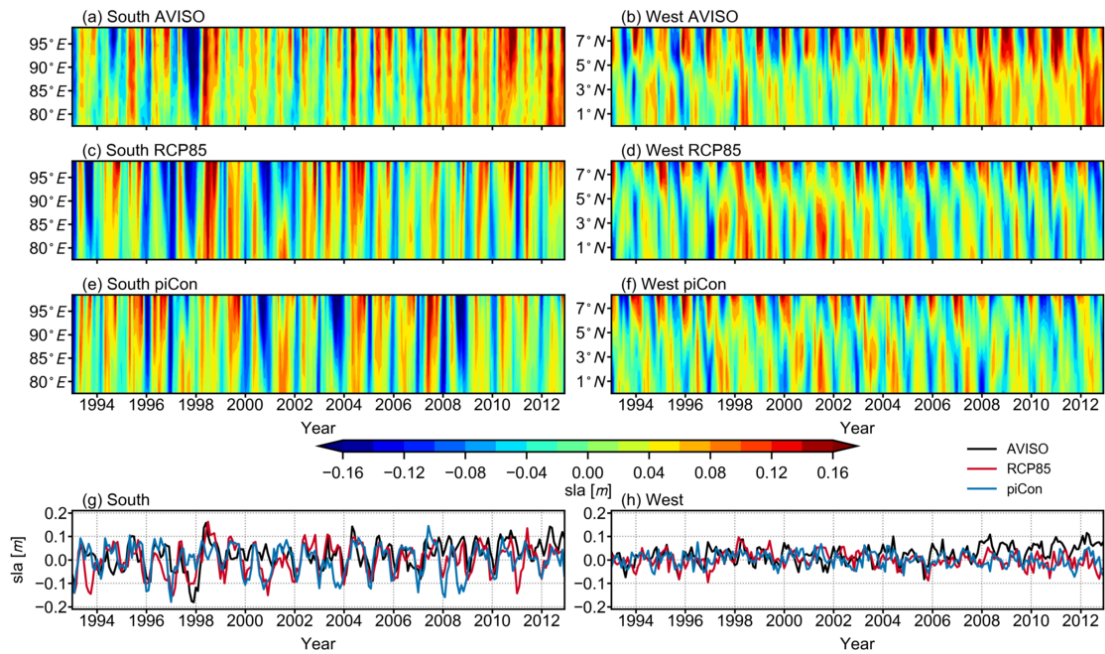


Figure 2.7: Comparison of time-longitude/latitude diagrams of sea level anomalies for AVISO (a, b), RCP85 (c, d), and piCon (e, f). The spatial average is shown in (g) for southern boundary and in (h) for western boundary, respectively.

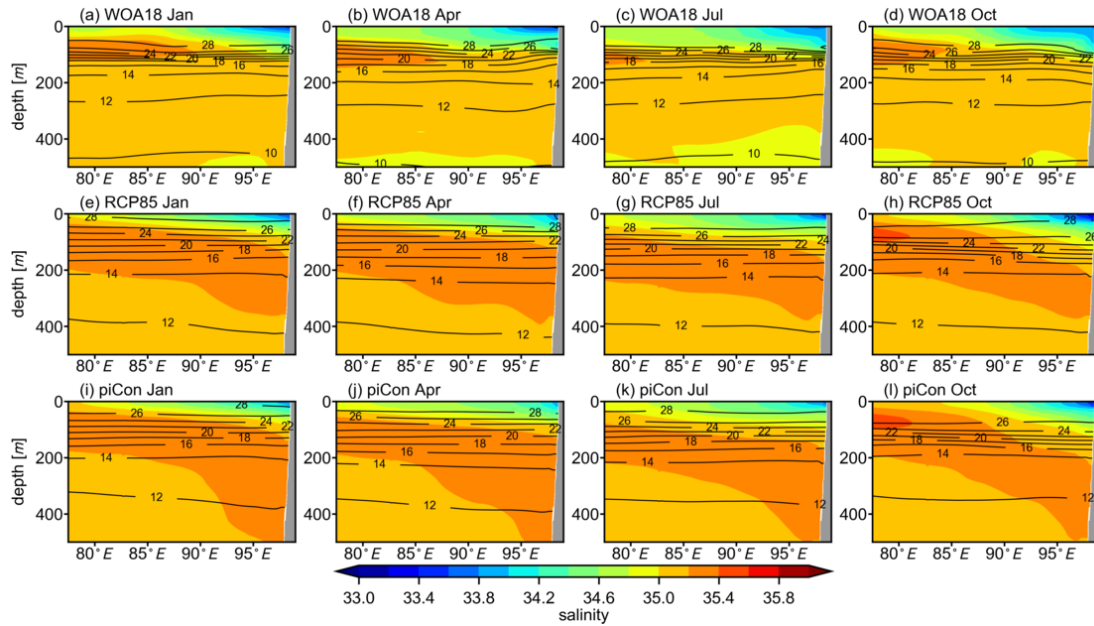


Figure 2.8: Longitude-depth distributions of climatological (1981-2010) monthly mean of salinity (color-shaded contours) and temperature (black contours) at southern boundary for WOA18 (a, b, c, d), RCP85 (e, f, g, h), and piCon (i, j, k, l).

by the outer model is reasonable on the climatological scale. For temperature, it is clear that the WOA18 shows a stronger climatological thermocline than the outer model results. At the western boundary (Figure 2.9), the outer model also shows good agreement with the WOA18 climatology in terms of salinity. In January, a significant low surface salinity area appears at the southern tip of India, while in July and October, the surface salinity is higher; this reflects the seasonal variability of the local flow field, which transports low salinity water from the BoB in winter and saltier water from the Arabian Sea in summer through the western boundary (Vinayachandran et al., 1999; Jensen, 2001; Lee et al., 2016; Sanchez-Franks et al., 2019). For temperature, the thermocline simulated by the outer model is relatively weak at the two open boundaries.

Certainly, there is a bias in temperature and salinity between the MPIOM and the observations. For the purpose of generating more realistic external forcing, a bias correction is applied on the monthly climatology scale for temperature and salinity. First, the difference between the WOA18 climatology and climatological monthly MPIOM output is calculated to determine the correction field. Then, the MPIOM output is corrected by adding the corresponding correction field for each month. Figure 2.10 shows an example to illustrate the improvement by this bias correction. Since the WOA18 only offers climatological data, the Argo-based RG.Clim (Roemich and Gilson, 2009) is used for validation. It can be seen that the corrected temperature field shows a stronger thermocline structure than the uncorrected field. After the bias correction, the vertical temperature structure is more in line with the observations. The standard deviation

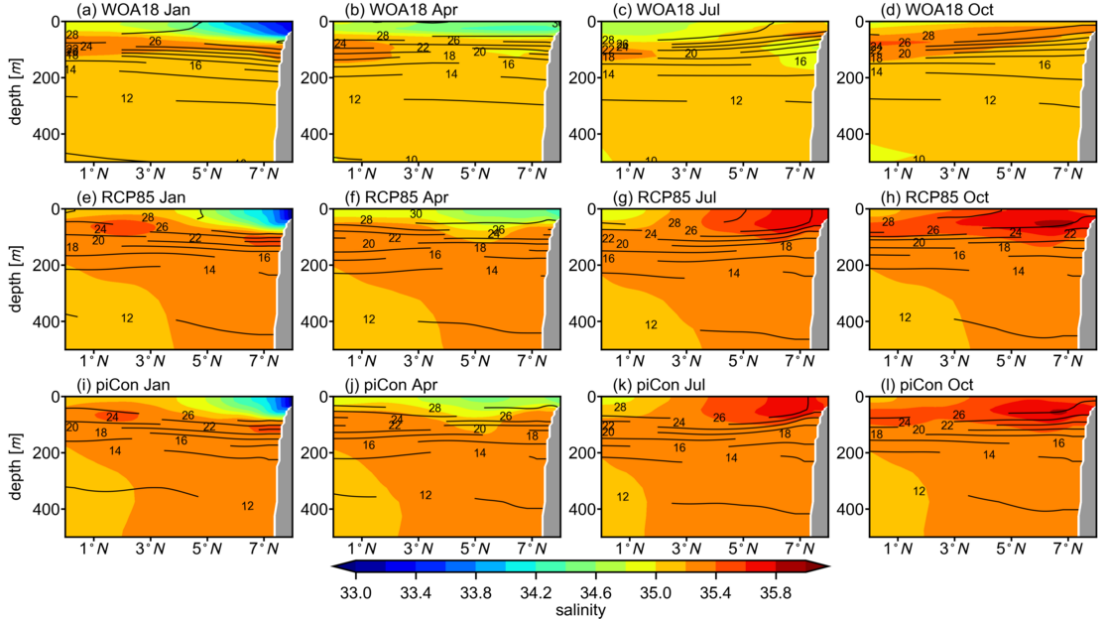


Figure 2.9: Latitude-depth distributions of climatological (1981-2010) monthly mean of salinity (color-shaded contours) and temperature (black contours) at western boundary for WOA18 (a, b, c, d), RCP85 (e, f, g, h), and piCon (i, j, k, l).

of annual means represents the intensity of interannual changes. Since only the climatological monthly variability is corrected by this bias correction process, it must be expected and can be seen that the interannual changes remain unchanged before and after the bias correction (Figure 2.10e, f). The comparison of the standard deviation of annual means also indicates that the interannual temperature variability given by MPIOM is reliable. The standard deviation of climatological monthly means represents the intensity of monthly changes. It can be observed that the temperature structure is more consistent with the observation after the bias correction (Figure 2.10g, h, i). This comparison also shows that the maximum amplitudes of interannual and seasonal changes at the southern boundary occur at the thermocline depth at around 100m.

Figure 2.11 shows the yearly horizontal averaged time series of temperature and salinity before and after the bias correction. It can be seen again that the bias correction does not change the interannual variation characteristics. For temperature, compared to piCon, RCP85 shows an obvious upward trend at the surface, 200m, and 500m depth. Under the RCP8.5 scenario, the changes of temperature decrease with increasing depth. At the end of the 21st century, ocean warming as suggested by the outer model can even happen at 500m depth. At a depth of 100m, as shown in Figure 2.10, the interannual temperature variability is significant, but it does not show a clear long-term trend. Meanwhile, because the warming is greater at the surface than at depth, the intensity of the thermocline will also be enhanced. For salinity, there is no significant long-term trend in both scenarios. The interannual salinity variability is significantly larger at the surface than at the subsurface and deep layers, which reflects the impact of the variable

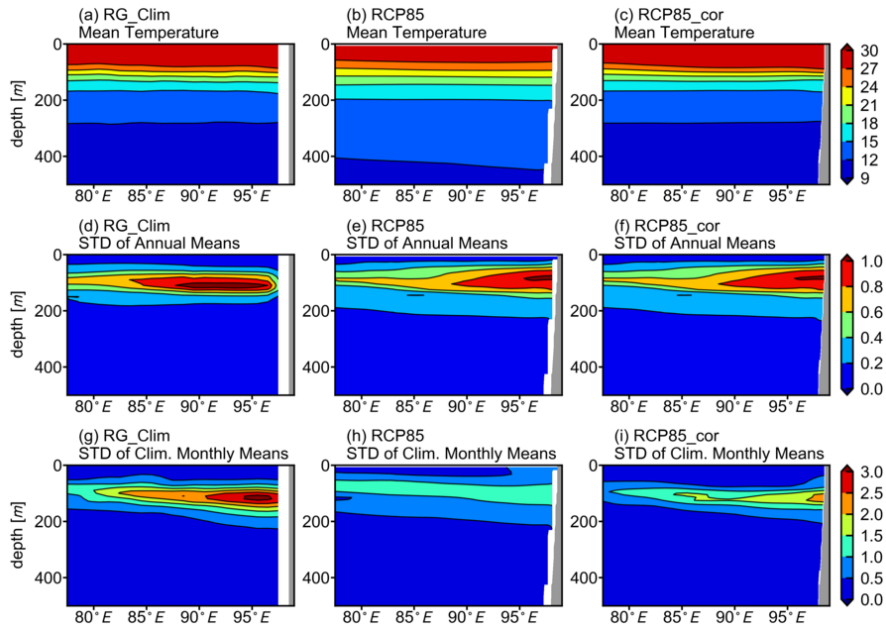


Figure 2.10: Comparison of mean temperature (a, b, c), standard deviation of annual means (d, e, f), and standard deviation of climatological monthly means (g, h, i) over 2004-2016 at southern boundary for RG\_Clim, RCP85, and RCP85\_cor.

freshwater flux.

In general, sea level height, temperature, and salinity derived from the outer model MPIOM are relatively consistent with the observations. After the bias correction, the distribution and the magnitude of the temperature and salinity patterns are improved. Compared to piCon, RCP85 shows a long-term rising trend of temperature, which reflects the trend of ocean warming under the high emissions pathway.

### 2.3.2 Air-sea Interface

Atmospheric forcing, such as air temperature, cloud cover, precipitation, specific humidity, air pressure, zonal wind stress, meridional wind stress, and wind speed derived from the atmospheric part ECHAM6 of MPI-ESM-MR, are six-hourly prescribed at the air-sea interface. These parameters are involved in the calculation of heat flux, momentum flux, and freshwater flux. They are also the primary sources of high-frequency ocean responses in the model domain. ERA5 (Hersbach et al., 2020) is the fifth generation WCMWF atmospheric reanalysis of the global climate, and it is selected as the reference for correcting the systematic error existing in ECHAM6. One of the apparent advantages of ERA5 is the high resolution; its horizontal resolution reaches about 31km. Before the correction, all data sets are linearly interpolated onto the HAMSOM grid.

Figure 2.12 shows the comparison of domain-averaged climatological monthly means for six scalars among ERA5, RCP85, and piCon. With respect to averaged value, these three data

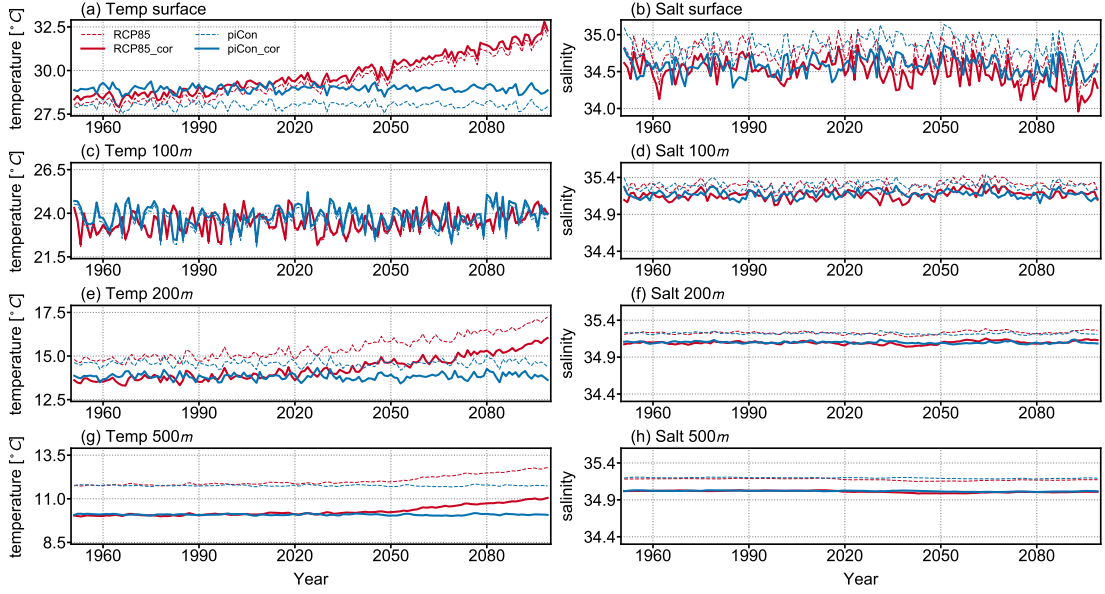


Figure 2.11: Yearly time series of lateral boundary averaged temperature (a, c, e, g) and salinity (b, d, f, h) at surface, 100m, 200m, and 500m, respectively.

sets generally show consistent seasonal variations; also regarding the standard deviations, the interannual changes of these three data sets are similar in magnitude. For air temperature (Figure 2.12a) and specific humidity (Figure 2.12d), because the period compared here contains the results under the high emissions pathway of 2006-2018, the average values of RCP85 are significantly higher than of piCon. For precipitation, unlike the result of the outer model ECHAM6, ERA5 does not peak in July. This comparison reflects that the atmospheric forcing given by ECHAM6 exhibits systematic errors.

The wind density function (Siegismund and Schrum, 2001) is used to describe the two-dimensional wind field. This function quantitatively addresses the angular distribution of wind forcing by combining the wind speed and their relative frequency of occurrence at predefined directions. Figure 2.13 shows the comparison of the climatological normalized wind density function of 72 predefined directions among three data sets. In general, these three data sets all indicate that the southwest monsoon dominates the BoB in summer and the northeast monsoon dominates in winter. The southwest monsoon's wind density is stronger than the northeast monsoon, which is also confirmed by Figure 2.13f.

Figure 2.14 shows the normalized relative frequency of wind in the BoB. All three data sets show that the occurrence of southwest winds in summer is more frequent than that of northeast winds, while the opposite is true in winter. By comparing the outer model results and the ERA5 results, it can be found that in summer, ERA5 shows more southwest winds than ECHAM6, while in winter, ECHAM6 shows more northeast winds. Figure 2.15 shows the mean wind speed. The distribution of the mean wind speed given by the ECHAM6 shows a good agreement with the ERA5 results, but generally larger in magnitude. Principally, ECHAM6 simulates the monsoon

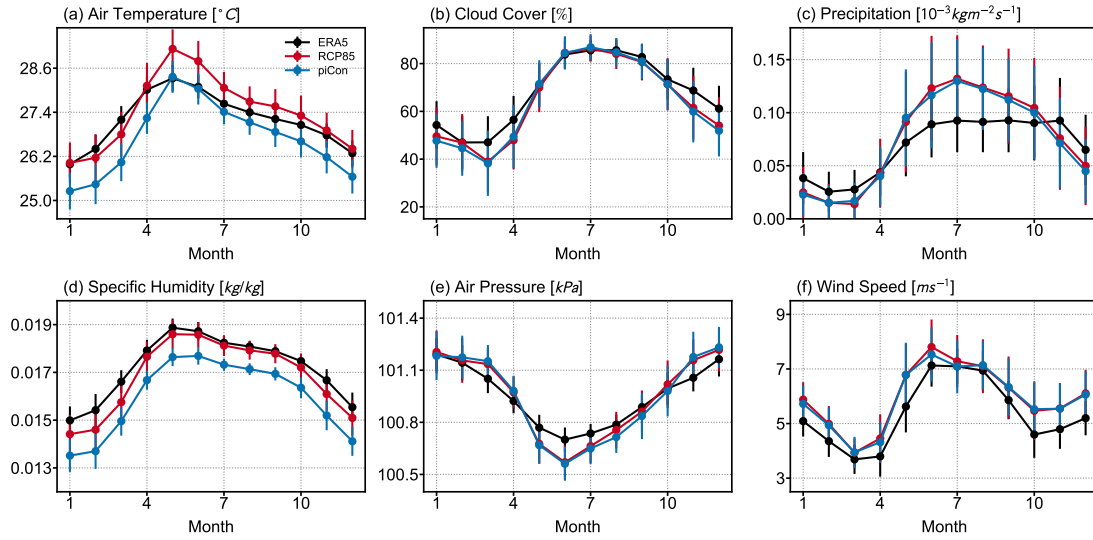


Figure 2.12: Comparison of climatological (1979-2018) monthly means of BoB spatially averaged air temperature (a), cloud cover (b), precipitation (c), specific humidity (d), air pressure (e), and wind speed (f) for ERA5, RCP85, and piCon. Vertical error bars represent standard deviation.

feature well in the BoB. However, the average wind speed is overestimated in ECHAM6.

It can be seen from the above comparisons that although ECHAM6 simulates relatively reasonable seasonal variation characteristics, there is still a certain systematic error. Hence, a bias correction process is applied for some atmospheric forcing parameters on the monthly climatology scale for eliminating these systematic errors. According to the characteristics of different parameters, different correction schemes are designed. For air temperature, cloud cover, and specific humidity, the correction fields are the difference between the ERA5 climatology and the climatological monthly ECHAM6 output, and correction of these parameters is performed by adding the corresponding correction field for each month. For precipitation, the correction fields are calculated by dividing ERA5 by ECHAM6, and for correction of precipitation, a multiplication of with these correction fields is performed. For wind speed, to keep the horizontal wind structure, the quotient of domain-averaged ERA5 and ECHAM6 is calculated as the correction factor, and correction of wind speed is performed by multiplying this factor. The air pressure keeps unchanged since it only affects sea level height due to the inverse barometric effect in HAMSOM. Wind directions also keep unchanged because the wind direction's adjustment may destroy the horizontal distribution characteristics of momentum flux at the sea surface.

Figure 2.16 shows the comparison of air temperature distribution among ERA5, RCP85, and RCP85\_cor. It can be seen that before being bias-corrected, the spatial structure of RCP85 is relatively smooth. After the bias correction, the air temperature shows more high-resolution features, and its distribution characteristics are more in line with ERA5. Especially in July, the corrected air temperature shows a gradient in the southeast direction that was not visible before being bias-corrected.

Figure 2.17 is equivalent to Figure 2.16, but shows the distribution of precipitation. Although

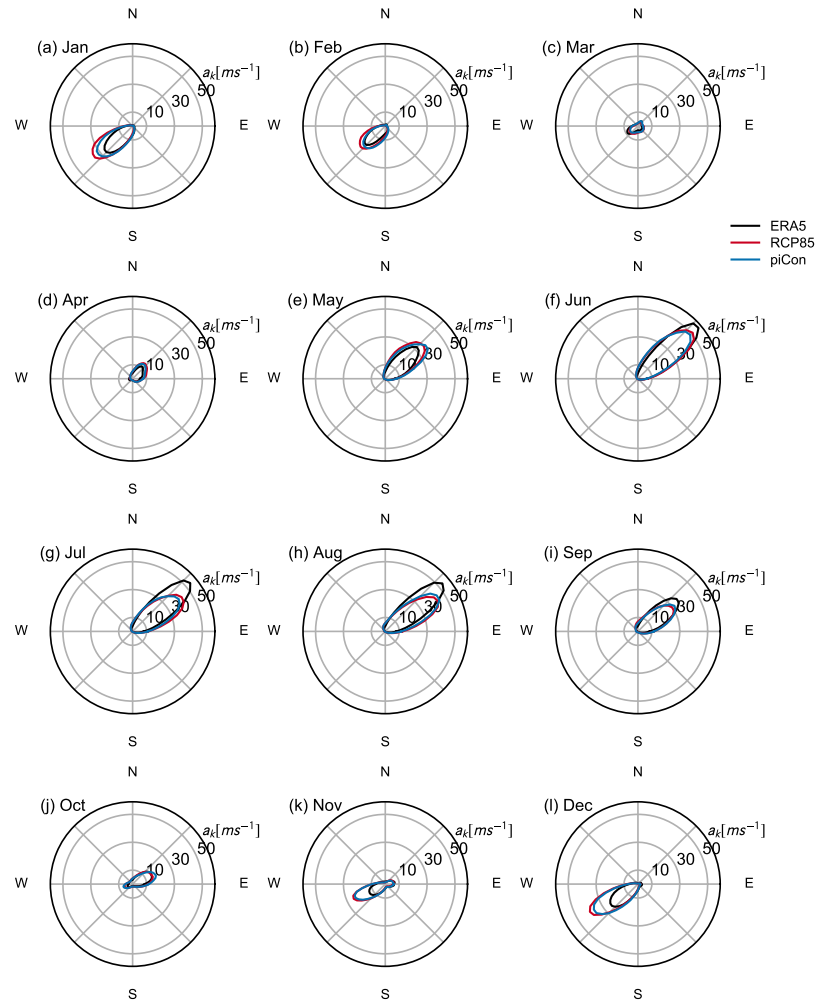


Figure 2.13: Comparison of climatological (1979-2018) normalized wind density function of 72 classes for the whole BoB for ERA5, RCP85, and piCon.

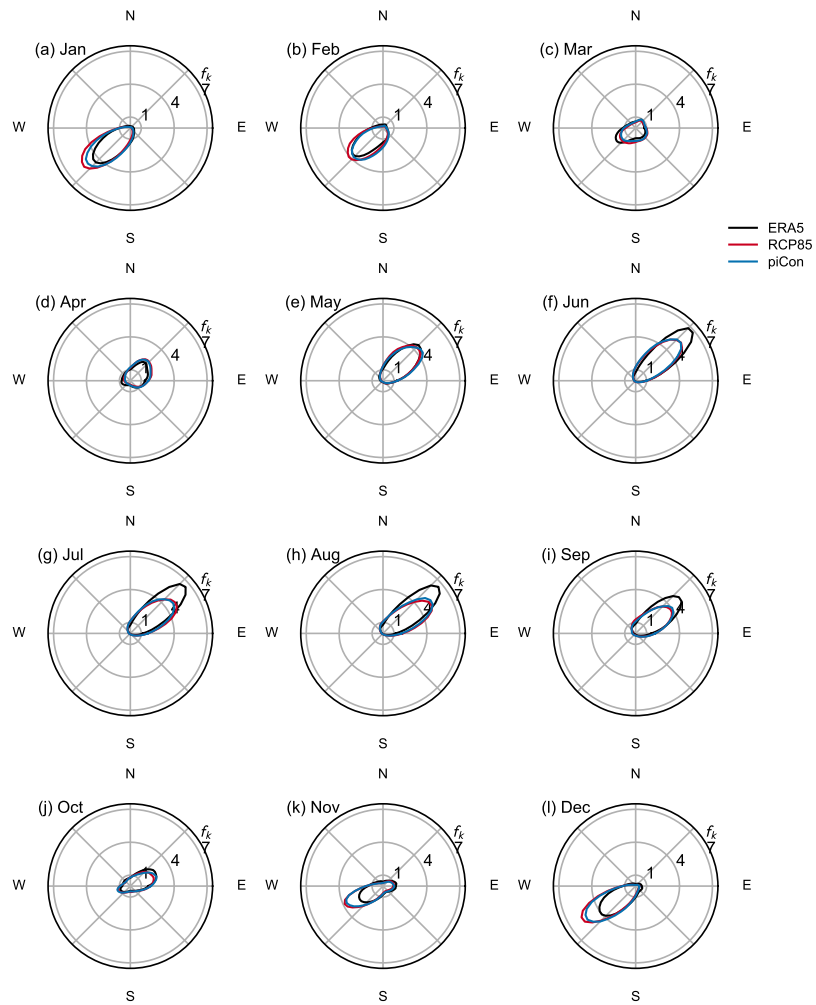


Figure 2.14: Comparison of climatological (1979-2018) normalized relative frequency of 72 classes for the whole BoB for ERA5, RCP85, and piCon.

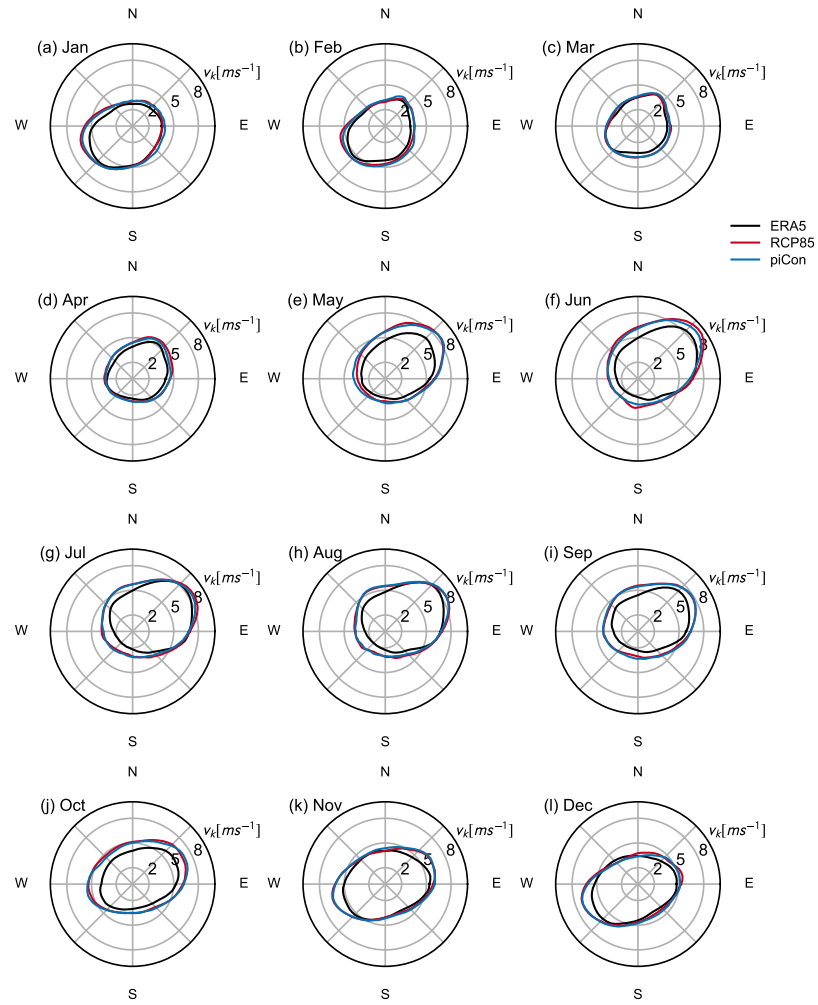


Figure 2.15: Comparison of climatological (1979-2018) mean wind speed of 72 classes for the whole BoB for ERA5, RCP85, and piCon.

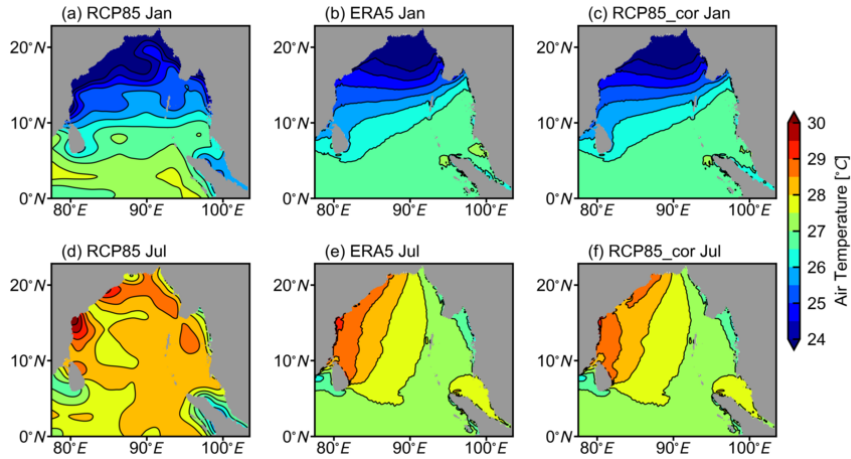


Figure 2.16: Climatological (1979-2018) monthly air temperature distributions of RCP85 (a, d), ERA5 (b, e), and RCP85\_cor (c, f) in January and July.

the uncorrected precipitation is generally consistent with ERA5, it shows relatively coarse due to the low resolution. The corrected precipitation is in close agreement with ERA5 not only in magnitude but also with respect to patterns, which clearly shows the improvement brought by the bias correction.

Figure 2.18 shows the distribution of the wind speeds. As mentioned above, because the need to keep the wind field pattern unchanged, only the domain averaged wind speeds are corrected, resulting in wind speeds, which are more consistent with ERA5 in magnitude. In general, the feature of uncorrected wind speeds are already in good agreement with ERA5, which supports the above analysis of the wind density function, indicating that ECHAM6 well simulates the monsoon characteristics in the BoB.

Figure 2.19 shows the yearly time series of eight domain-averaged atmospheric parameters. It can be seen that the bias correction does not affect the interannual variability. The systematic error in the direct ECHAM6 output can most obviously be seen in the wind speeds. This error is well eliminated through the bias correction process (Figure 2.19g). As can be seen from the air temperature, under the RCP8.5 scenario, ECHAM6 shows that at the end of the 21st century, the averaged annual air temperature can reach  $31^{\circ}\text{C}$  in the BoB, which is about  $4^{\circ}\text{C}$  higher than in the early 21st century. In contrast, as expected, under the piCon scenario, the air temperature remains stable. The specific humidity, which is highly correlated with the air temperature, also shows a similar long-term trend. For other atmospheric parameters, although there are some prominent oscillations on the interannual time scale, the long-term trend is not significant.

### 2.3.3 River Discharge

In addition to the freshwater import and export at the sea surface brought by precipitation and evaporation, river discharge, especially the discharge from the three largest rivers, the Ganges River, the Irrawaddy River, and the Salween River, can also significantly affect the sea surface

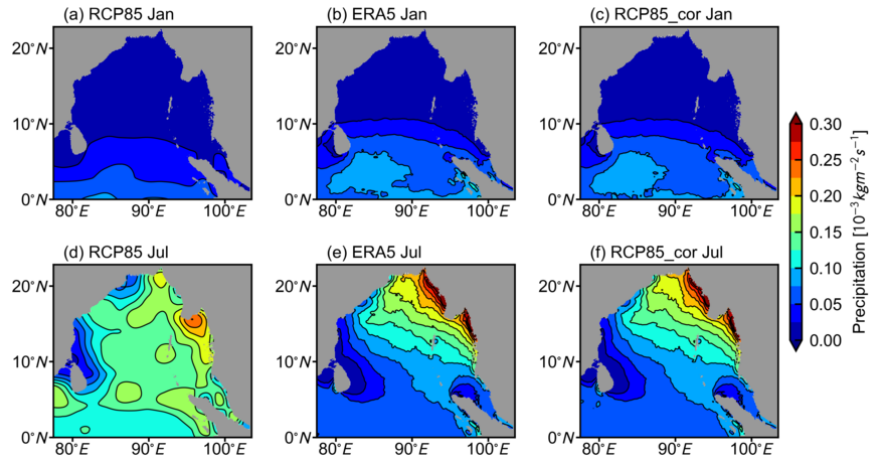


Figure 2.17: Climatological (1979-2018) monthly precipitation distributions of RCP85 (a, d), ERA5 (b, e), and RCP85\_cor (c, f) in January and July.

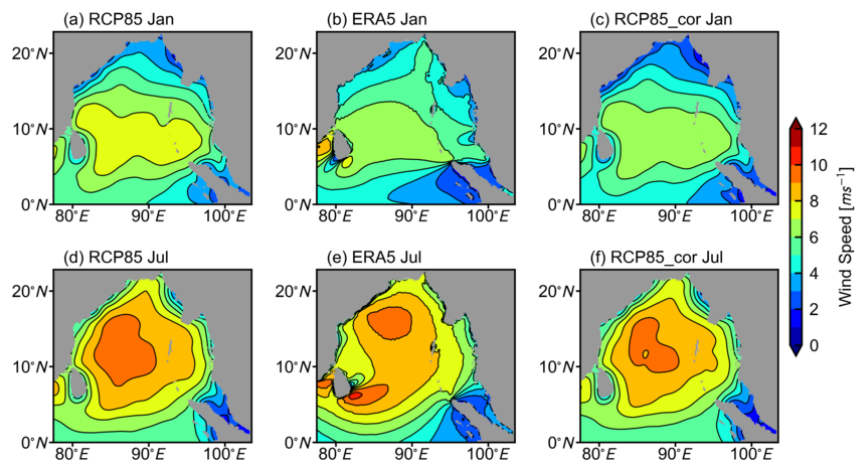


Figure 2.18: Climatological (1979-2018) monthly wind speed distributions of RCP85 (a, d), ERA5 (b, e), and RCP85\_cor (c, f) in January and July.

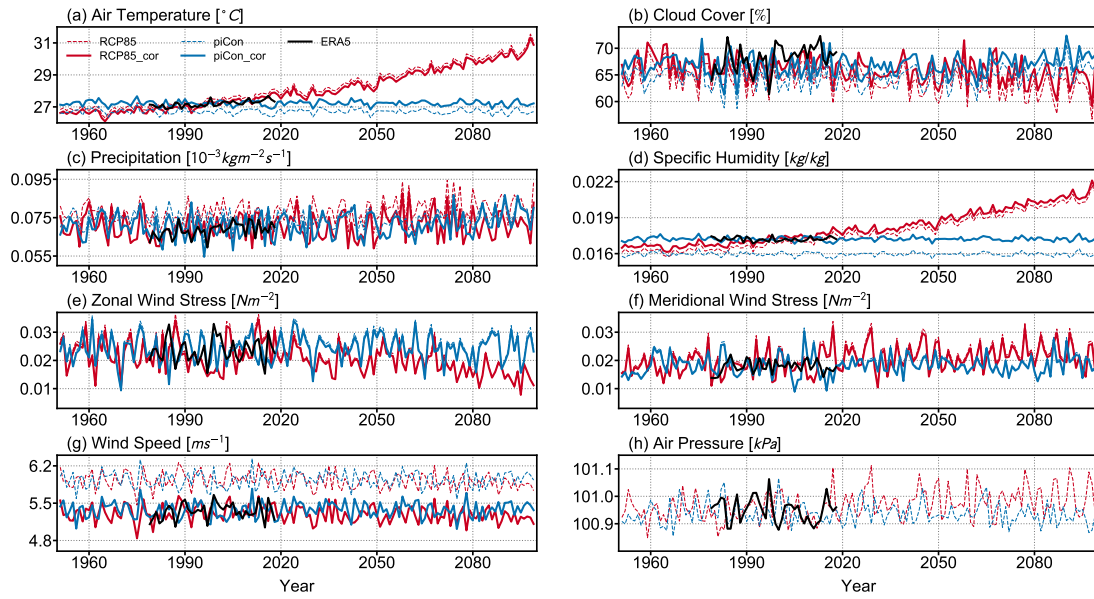


Figure 2.19: Yearly time series of BoB spatial averaged air temperature (a), cloud cover (b), precipitation (c), specific humidity (d), zonal wind stress (e), meridional wind stress (f), wind speed (g), and air pressure (h), respectively.

salinity along the coast. The river discharge further modulates the horizontal salinity structure in the upper layers. Therefore, the river discharge derived from ECHAM6 is also six-hourly prescribed. Unlike ECHAM6, which calculates the river component for all wet points, HAMSOM introduces the river effect by inputting an additional water volume to the selected river point.

The Water Global Assessment and Prognosis (WaterGap; Döll et al., 2003) data are selected as a reference for correcting the ECHAM6 river output. Figure 2.20 shows the distribution of river points in each data set and the average discharge rate of each river. The WaterGap data have a high resolution of approximately  $50\text{km} \times 50\text{km}$ , while the horizontal resolution of ECHAM6 is approximately  $200\text{km} \times 200\text{km}$ . Hence, WaterGap shows more river points because of its high resolution. The discharge rate of WaterGap indicates that the three largest rivers in this area are the Ganges River, the Irrawaddy River, and the Salween River. The uncorrected river discharge given by ECHAM6 shows the wrong location of the major rivers because of the relatively low resolution. For example, the estuary of the Ganges River deviated from its actual location. In addition, the uncorrected river discharge rates fail to correctly reflect the input from the other two major rivers, the Irrawaddy River and the Salween River.

The objective of the correction is to ensure that the river discharge can reasonably reflect the main characteristics of the river input in this region, especially of the dominant three largest rivers. Therefore, the locations of the river points are adjusted according to the actual estuary locations. The magnitudes of three major rivers are also corrected by means of the WaterGap data. Figure 2.20c and 2.20e show the corrected RCP85 and piCon river locations and the corresponding multi-year averaged discharge rate. It can be seen that the distribution of rivers

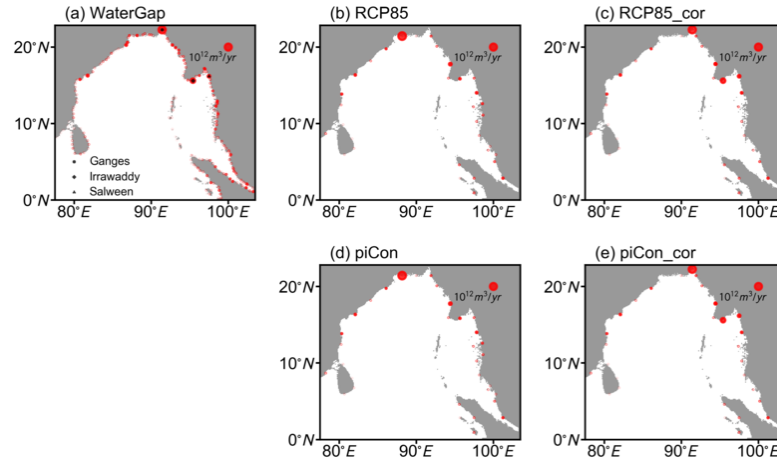


Figure 2.20: Distributions of river points and their multi-year (1979-2008) average discharge rate (scatter area) for WaterGap (a), RCP85 (b), RCP85\_cor (c), piCon (d), and piCon\_cor (e), respectively. Locations of the Ganges River, the Irrawaddy River, and the Salween River are marked in (a).

is significantly improved after the correction.

Figure 2.21 shows the comparison of climatological monthly river discharge rate of all relevant rivers and the of three largest rivers. Before the correction, ECHAM6 underestimates the total river discharge, significantly underestimates the discharge of the Irrawaddy River and the Salween River and slightly overestimates the discharge of the Ganges River. After the correction, the monthly variations and magnitudes of the discharge rate are significantly improved with compared to the results of WaterGap.

Figure 2.22 shows the yearly time series of the discharge rates. Especially for the Irrawaddy River and the Salween River, the corrected yearly discharge rate is significantly more consistent with the WaterGap rates. It can be seen that for the total river discharge, as well as for the Irrawaddy River and the Salween River, RCP85 shows higher rates than piCon in the second half of the 21st century, and RCP85 shows an increasing trend, which may also reflect the climate impact on river basins under the high emissions pathway. Overall, this correction improves the river discharge forcing, in terms of the input location, the discharge rate in magnitude, and the seasonal variation.

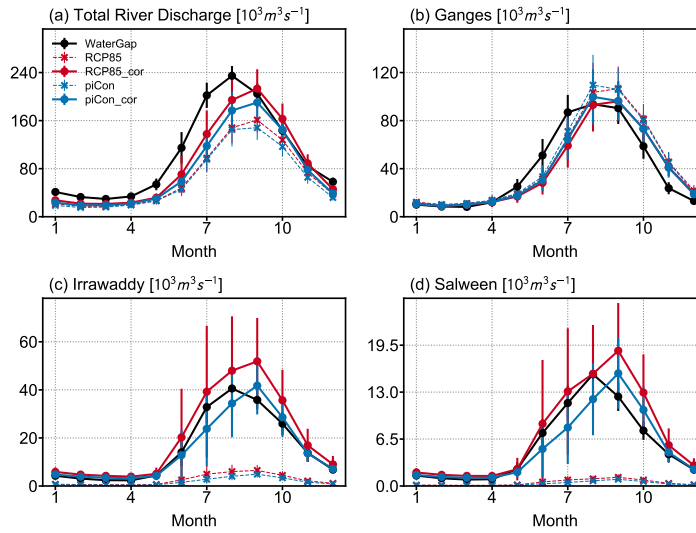


Figure 2.21: Comparison of climatological (1979-2008) monthly river discharge rate of the all rivers (a), the Ganges River (b), the Irrawaddy River (c), and the Salween River (d) for Water-Gap, RCP85, RCP85.cor, piCon, and piCon.cor. Vertical error bars represent standard deviation.

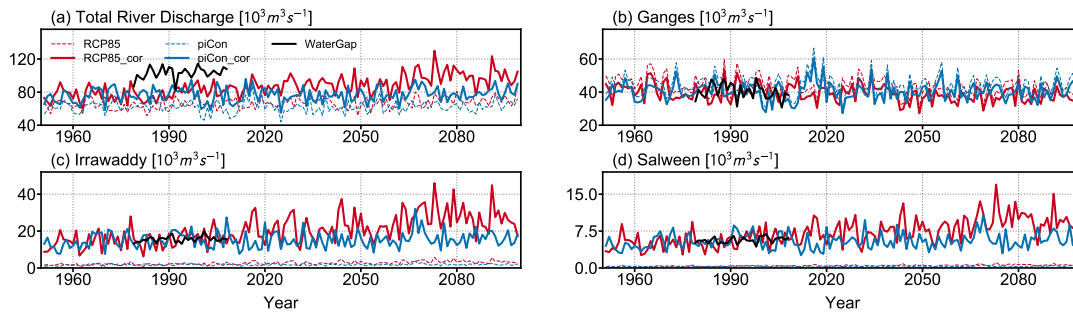


Figure 2.22: Yearly time series of river discharge rate of the all rivers (a), the Ganges River (b), the Irrawaddy River (c), and the Salween River (d), respectively.



## Chapter 3

# Model Evaluation

As mentioned in the previous chapter, the ocean simulation in the BoB is downscaled using the regional model HAMSOM driven by the global model MPI-ESM. The forcing extracted from the outer model MPI-ESM is bias-corrected for eliminating the systematic error and improving the regional downscaling performance. The HAMSOM experiment RCP85 is discussed by comparing the corresponding global model results and other third-party data sets in this chapter for evaluating the performance of HAMSOM.

### 3.1 Sea Level Anomaly

The sea level anomaly is a deviation from the average sea level height, reflecting the patterns and changes of eddies and currents. In HAMSOM, the sea level height is mainly modulated by the flow field under consideration of the volume conservation. The river discharge also modulates the sea level height along the coast and then affect the offshore area. The sea level height can be monitored by satellite altimeters, including the AVISO product. Figure 3.1 shows the multi-year monthly mean of sea level anomalies for HAMSOM and AVISO. In the northern BoB, the HAMSOM results show that sea level anomalies along the coast are negative in January and April, and positive in July and October, which is in good agreement with the satellite observation. The seasonal characteristics of sea level anomalies along the coast are consistent with the seasonality of the river discharge (Figure 2.21). In the western BoB, the AVISO results show significant positive anomalies in April, which suggests the existence of an anticyclone, indicating that the EICC flows poleward. However, the AVISO results show significant negative anomalies in October, which suggests the existence of a cyclone, indicating that the EICC flows equatorward. This feature is well reproduced in HAMSOM. Besides the good performance of the overall patterns and seasonal changes, HAMSOM also reproduces the correct magnitude of sea level anomalies observed by satellite.

Figure 3.2 shows the monthly time series of domain-averaged sea level anomalies for five selected subareas (marked in Figure 3.1a, e). In the western (Figure 3.2a) and eastern (Figure 3.2d) bay, and the southern Andaman Sea (Figure 3.2e), the time series of HAMSOM is in good agreement with the satellite observations. Especially in the western bay, the seasonal variation

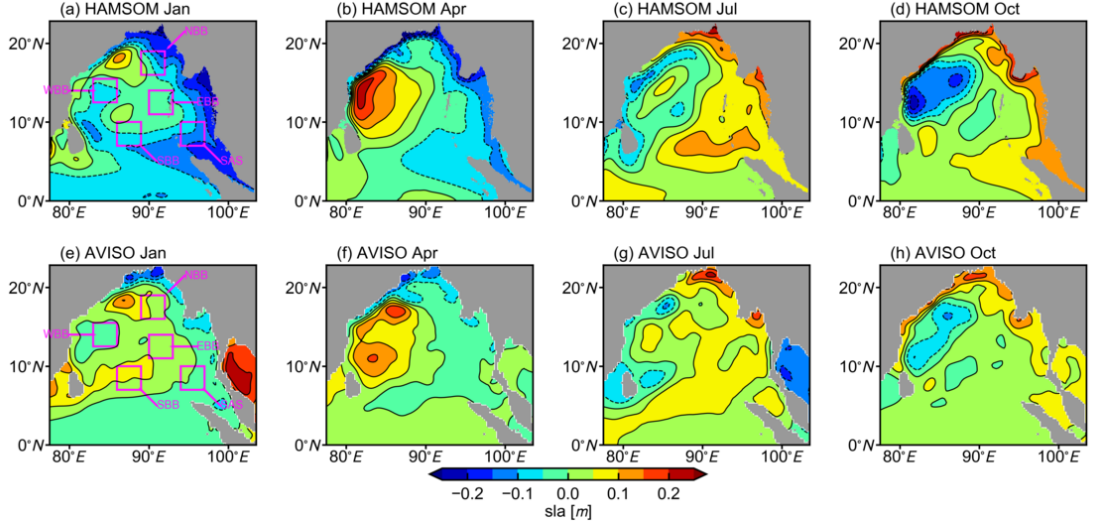


Figure 3.1: Comparison of multi-year (1993-2012) monthly mean of sea level anomalies for HAMSOM (a, b, c, d) and AVISO (e, f, g, h). Five selected subareas are marked with magenta boxes in (a) and (b).

of sea level anomalies is well simulated in HAMSOM. In the northern (Figure 3.2b) and southern (Figure 3.2c) bay, although there is a correlation between the results of HAMSOM and AVISO, the correlation coefficients are relatively small. In general, the above comparisons prove that HAMSOM well simulates the spatial patterns and seasonal variations of sea level anomalies in the BoB.

## 3.2 Thermodynamics

For the entire simulated domain, the temperature input at lateral boundaries and the heat flux calculated at the air-sea interface are the major factors affecting the average temperature. The heat exchange at the air-sea interface significantly affects the upper ocean thermodynamics. For this reason, the calculation of heat flux in HAMSOM is also evaluated in this subsection. In general, the validation of temperature and salinity comprehensively reflects the performance of HAMSOM with respect to thermodynamic processes.

Taylor diagrams are commonly used to graphically summarize the relative merits of different data sets (Taylor, 2001). Figure 3.3 shows the Taylor diagram for surface/subsurface temperature and salinity in the BoB. The subsurface refers to a depth of 100 *m*. The global quality controlled monthly ocean temperature and salinity objectively analyses of version 4.2.1 of the Met Office Hadley Centre 'EN' series (Good et al., 2013), named as EN4, is selected as a reference data set in the Taylor diagram. The German contribution of the Estimating the Circulation and Climate of the Ocean project GECCO2 (Köhl, 2015) is also used here as a third-party data set. The standard deviation of the sea surface temperature of HAMSOM is almost the same with MPIOM, and their values are consistent with observation-based EN4 data (Figure 3.3a). For

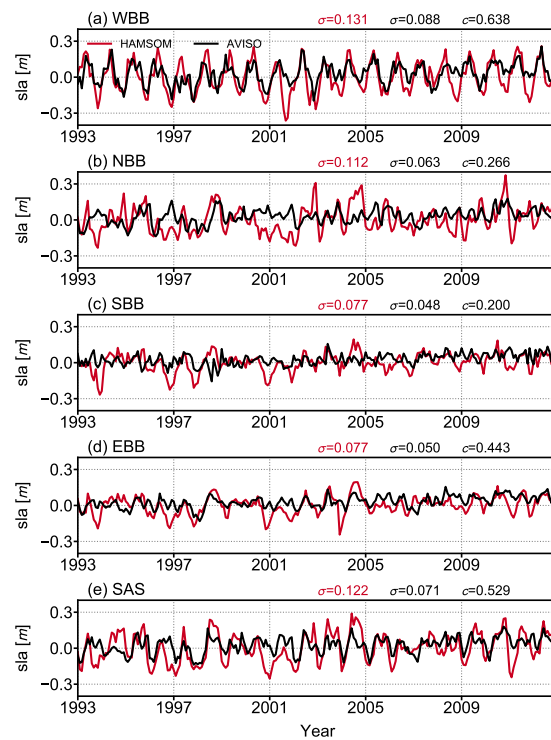


Figure 3.2: Monthly time series of domain-averaged sea level anomalies for the selected subarea WBB (a), NBB (b), SBB (c), EBB (d), and SAS (e). The standard deviation  $\sigma$  of time series is labeled with the corresponding color. The Pearson correlation coefficient  $c$  between HAMSOM and AVISO is labeled, too.

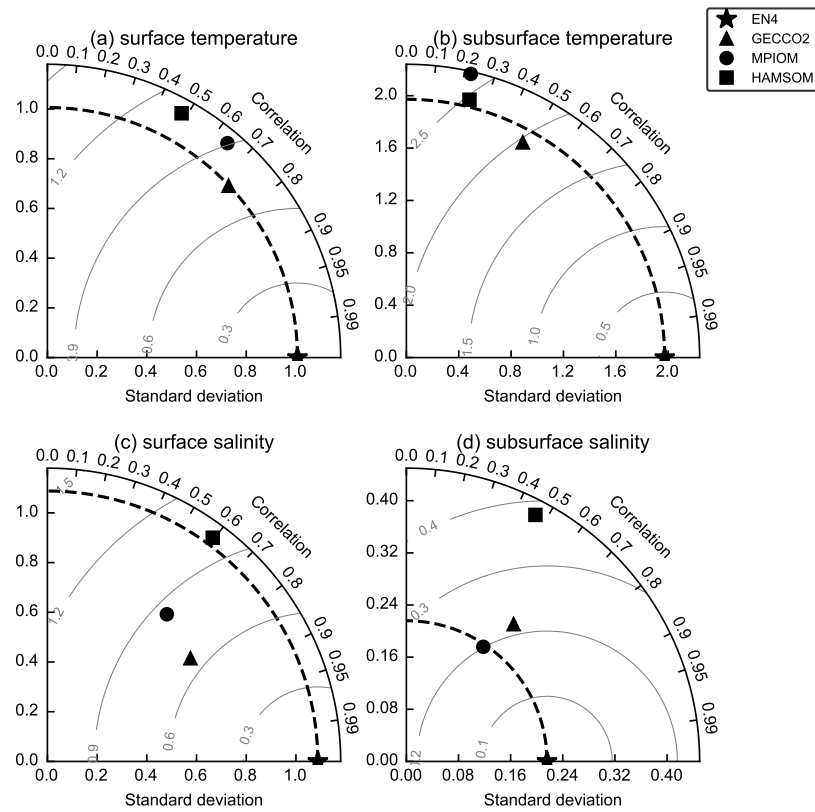


Figure 3.3: The Taylor diagram of the surface temperature (a), subsurface temperature (b), surface salinity (c), and subsurface salinity (d) from 1981 to 2010 for different data sets. The observation-based EN4 (pentagon) is chosen as the reference data set. Grey lines indicates the centered RMS difference from the reference data set.

the subsurface temperature, the standard deviation of HAMSOM is smaller and more consistent with EN4 than that of MPIOM (Figure 3.3b), indicating that HAMSOM performances better than its global forcing model MPIOM for the subsurface temperature. This improvement can be attributed to the correction of the lateral boundary temperature forcing. As mentioned in the previous chapter, MPIOM underestimates the vertical stratification. The WOA18-based bias correction is responsible that the seawater temperature input has a more realistic vertical structure. HAMSOM shows the standard deviation closest to the EN4 data for sea surface salinity compared to MPIOM and GECCO2 (Figure 3.3c), which can be attributed to the bias correction of the river discharge. For the subsurface salinity, the results show that the standard deviation is bigger than that of EN4. Observations for subsurface salinity are sparse in the BOB. The EN4 data also shows a weight index from 0 to 1, which indicates the total weighting given to the observation increments when forming this objective analyses for each cell. The mean weight of subsurface temperature and salinity for the BoB is 0.57 and 0.22, respectively. So, the standard deviation of the subsurface salinity of EN4 may not represent the realistic state.

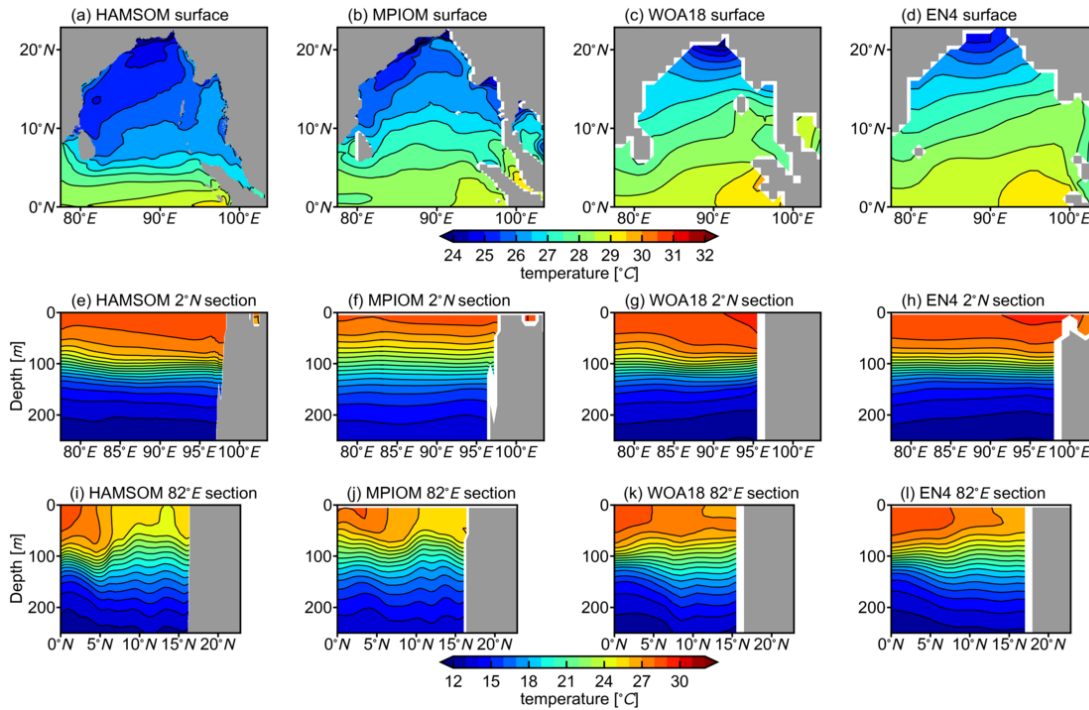


Figure 3.4: Comparison of climatological (1981-2010) monthly seawater temperature in January for HAMSOM (a, e, i), MPIOM (b, f, j), WOA18 (c, g, k), and EN4 (d, h, l). First row is the sea surface. Second row is the zonal section at  $2^{\circ}N$ . Third row is the meridional section at  $82^{\circ}E$ .

Figures 3.4 and 3.5 show the climatological monthly mean of temperature for four data sets in January and July, respectively. HAMSOM naturally inherits general features introduced at the open lateral boundaries from its global provider, such as the sea surface temperature gradient from south to north in January. Meanwhile, whether the meridional or the zonal section, the HAMSOM results are more consistent with the observations than its global forcing model MPIOM, especially for the strength of the thermocline. In July, the sea surface temperature of HAMSOM is relatively low.

Figures 3.6 and 3.7 show the climatological monthly mean of salinity in January and July, respectively. For the sea surface salinity, the HAMSOM results show a gradient from southwest to northeast, which is more consistent with observations than its global forcing model MPIOM. The HAMSOM results show low salinity along the coast, reflecting the influence of freshwater input through rivers. The vertical salinity distribution given by HAMSOM is also more consistent with observations than by MPIOM.

The seasonality is one of the most crucial characteristics in the BoB. For the overall monthly climatology of temperature and salinity, the HAMSOM results show reasonable seasonal variabilities (Figure 3.8). The RG\_Clim used in this comparison offers a basic description of the modern upper ocean. This data set compensates for the lack of subsurface salinity observations in the BoB, but this data set period is only from 2004 to 2016. All five data sets show a consistent

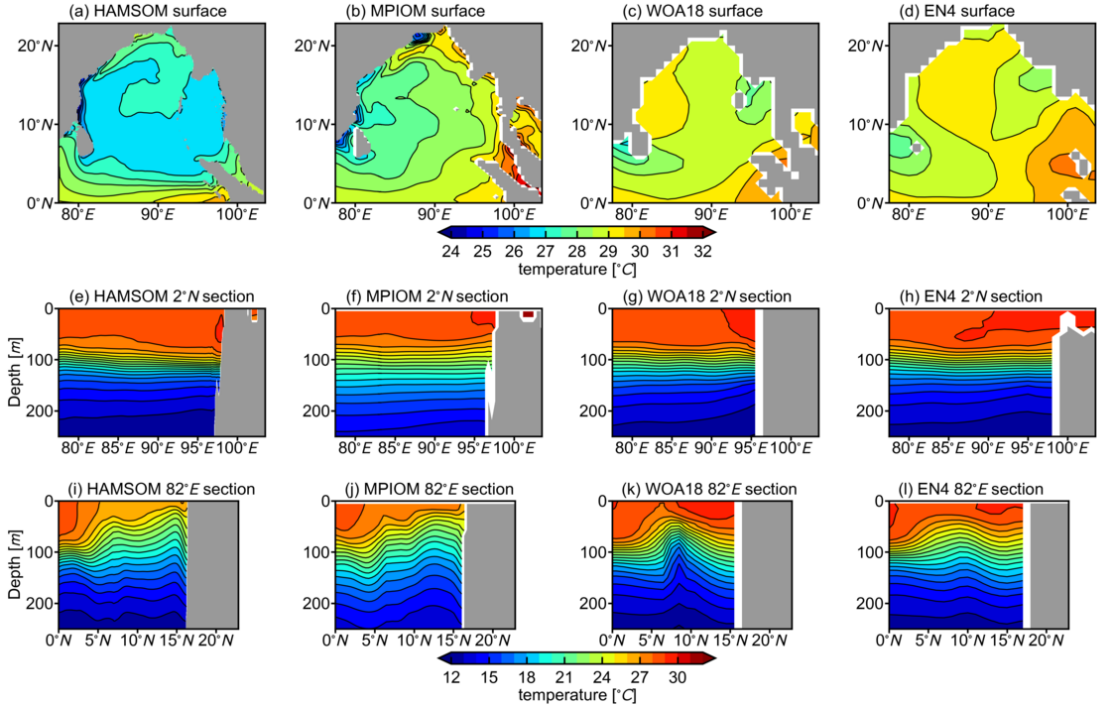


Figure 3.5: As in Figure 3.4, but for July.

seasonality at the surface, which indicates the dominance of the monsoon. For the subsurface, the seasonality is relatively weak. The standard deviation of HAMSOM results agrees with other data sets, indicating that the amplitude of seasonal changes simulated by HAMSOM is reliable.

The long-term sea surface temperature and salinity trends given by HAMSOM is in agreement with its global model (Figure 3.9). The sea surface temperature is considered to rise under the high emissions pathway, and numerical simulation can be used to confirm the temperature rises and the respective rates. The time series of yearly sea surface temperature given by HAMSOM show the same variability as the MPIOM results, but there is a relatively constant offset between these two models. For the sea surface salinity, HAMSOM shows a significant drop before 1960 and then becomes stable. After the stabilization, the changes of the HAMSOM simulated salinity are consistent with the MPIOM results. However, there is also an offset that maybe due to the bias correction of river discharge. In general, the downscaled HAMSOM agrees with its global forcing model, proving the consistency of HAMSOM results.

The air-sea heat flux modulates sea surface temperature. As stated in the model description, the short wave radiation (Figure 3.10), long wave radiation (Figure 3.11), sensible heat flux (Figure 3.12), and latent heat flux (Figure 3.13) are calculated separately during the run of HAMSOM. From the calculation results, the BoB mainly gains heat through the short wave radiation and loses heat through the latent heat flux and long wave radiation. The short wave radiation is mainly affected by the sun's altitude angle, so it shows a meridional gradient. The long wave radiation and the sensible heat flux have similar spatial distributions, but the mag-

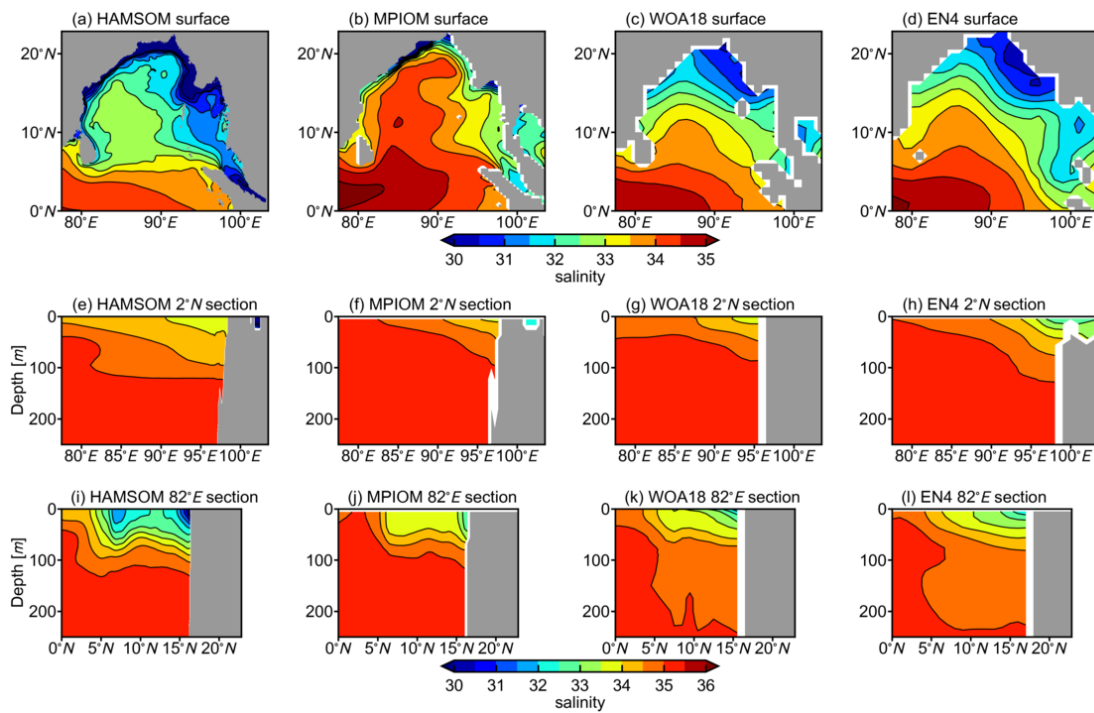


Figure 3.6: Comparison of climatological (1981-2010) monthly salinity in January for HAMSON (a, e, i), MPIOM (b, f, j), WOA18 (c, g, k), and EN4 (d, h, l). First row is the sea surface. Second row is the zonal section at  $2^{\circ}N$ . Third row is the meridional section at  $82^{\circ}E$ .

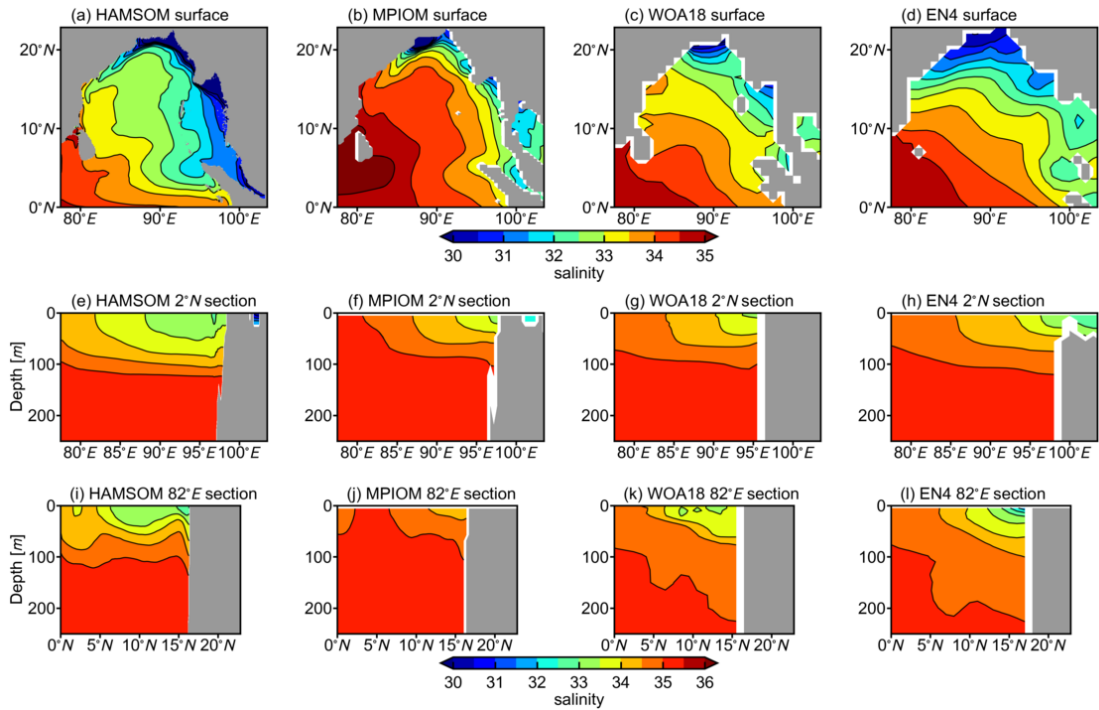
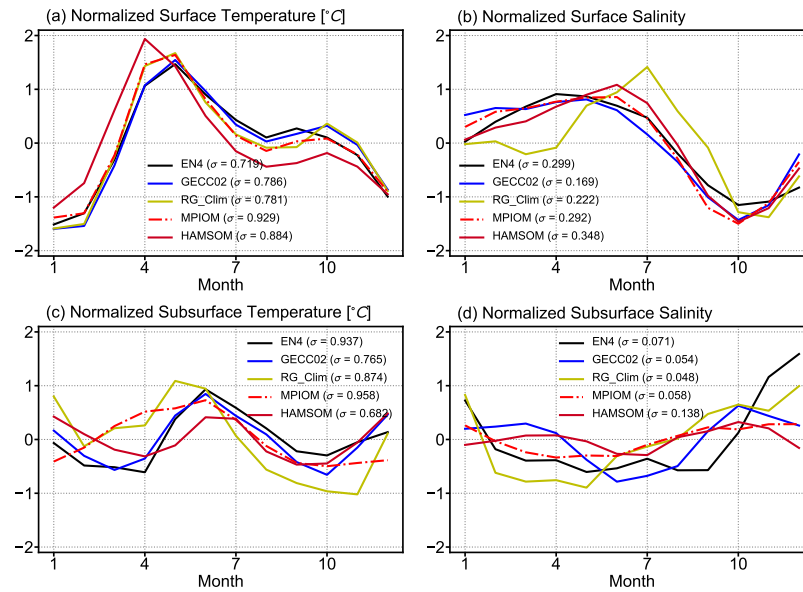


Figure 3.7: As in Figure 3.6, but for July

Figure 3.8: Normalized monthly climatology (1981-2010) of surface temperature (a), surface salinity (b), subsurface temperature (c), and subsurface salinity (d) of the BoB for different data sets. The standard deviation  $\sigma$  corresponding to each data set is labelled.

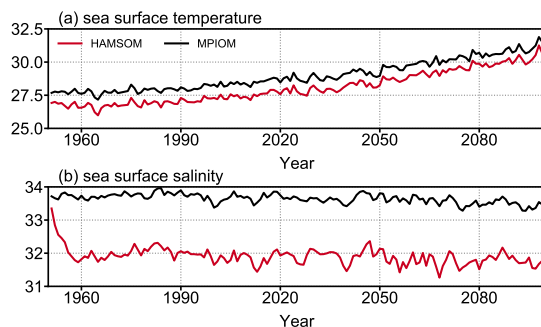


Figure 3.9: Comparison of yearly time series of the BoB domain-averaged sea surface temperature (a) and sea surface salinity (b) between the regional model HAMSOM (red line) and the global model MPIOM (black line), under the historical scenario and the RCP8.5 scenario (since 2006).

nitude of long wave radiation is more prominent than that of the sensible heat flux. The latent heat flux results show that there is a significant heat loss in the northwestern BoB, especially in January, suggesting that this area evaporates vigorously since the latent heat flux mainly reflects the evaporation process. It is worth noting that the contours shown near the lateral boundaries are artefacts caused by open boundary effect.

The net heat flux (Figure 3.14) can be obtained by comprehensively considering these four heat flux terms. In April, the BoB, especially the coastal area in its northwestern part, gains heat from the atmosphere, while in January, it loses heat to the atmosphere. There is a significant loss of heat at the lateral boundaries for all months, which is artificially caused by the open boundary effect. The seasonal variation of the net heat flux is more significant in the western part of the BoB than in the eastern part, which is supposed to be related to the local seasonal flow field and the corresponding thermodynamic processes.

The annual cycle of heat flux (Figure 3.15) for the inner region (Figure 3.14a, magenta borders) indicates significant seasonal variabilities of the heat exchange at the BoB air-sea interface. The incoming short wave radiation and the outgoing long wave radiation have almost the same seasonal variation, but the magnitudes are different. Their maximum values appear around March, and their minimum values appear around August. The annual cycle of sensible heat flux indicates that, on average, from January to April, the sea surface temperature is higher than the air temperature, resulting in the sensible heat transfers from the ocean to the atmosphere. While from May to November, the sea surface temperature is lower than the air temperature, resulting in the sensible heat transfers from the atmosphere to the ocean. The seasonal variation of latent heat flux is highly associated with the precipitation. For instance, the precipitation is minimal in the winter, while the latent heat loss from the ocean is maximal, indicating a robust evaporation process. The net heat flux shows two peaks around March and September. For the primary peak around March, the ocean mostly gains heat due to short wave radiation. At the secondary peak around September, the heat loss due to the latent heat flux is minimal. In general, the HAMSOM calculated heat fluxes suggest that the BoB loses heat to the atmosphere with a magnitude of  $25Wm^{-2}$  on average, which causes the sea surface temperatures simulated

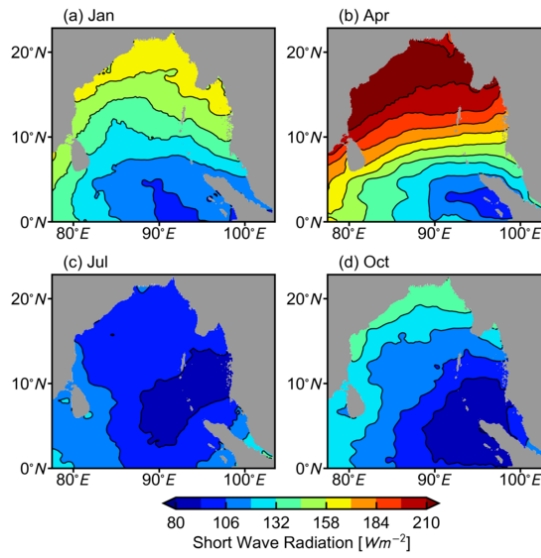


Figure 3.10: Climatological (1979-2008) monthly average of the incoming short wave radiation in January (a), April (b), July (c), and October (d).

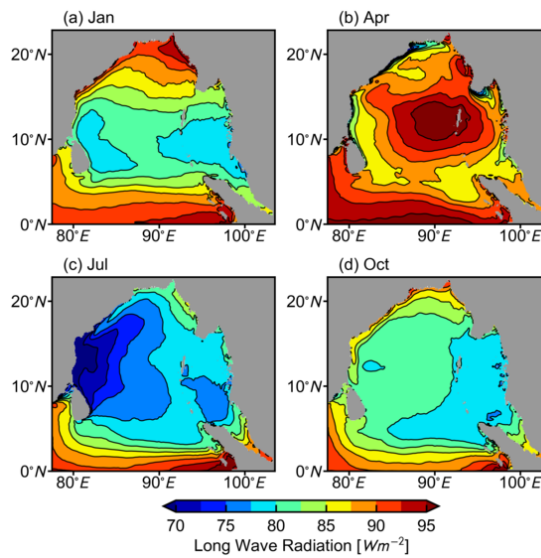


Figure 3.11: As in Figure 3.10, but for the outgoing long wave radiation.

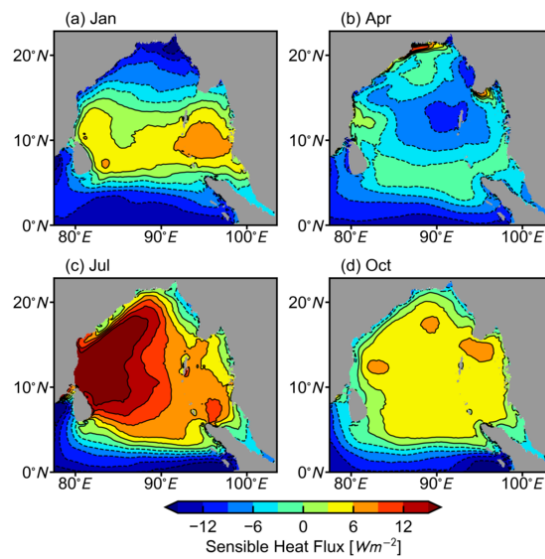


Figure 3.12: As in Figure 3.10, but for the incoming sensible heat.

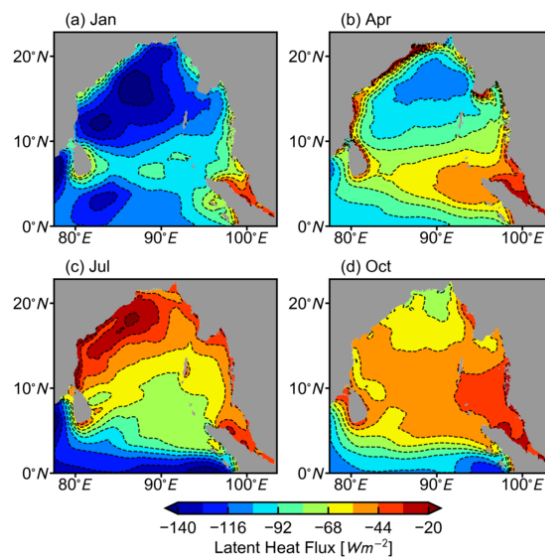


Figure 3.13: As in Figure 3.10, but for the incoming latent heat.

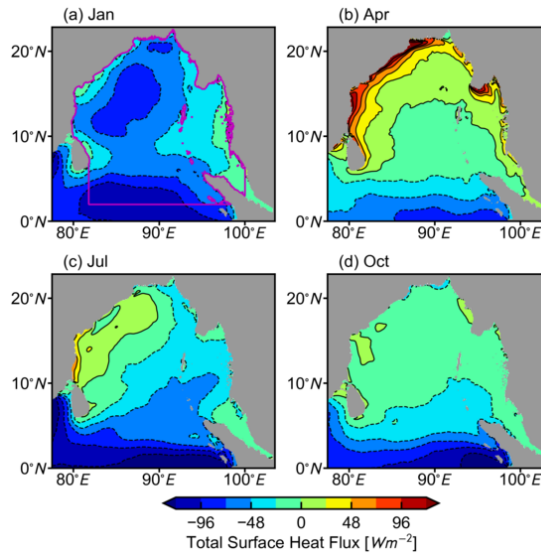


Figure 3.14: As in Figure 3.10, but for the total surface heat flux. Positive values refer to the heat into the sea. Magenta borders in (a) mark the area where is used to analyse the domain-averaged heat flux in Figure 3.15.

by HAMSOM to be lower compared to its global forcing model.

### 3.3 Flow Field

The flow field simulated by HAMSOM incorporates the wind-induced flow, the barotropic flow caused by the sea surface height gradient, and the baroclinic flow caused by the density gradient. For a regional downscaling simulation, the kinetic energy is expected to reach a steady-state after spin-up. This section mainly evaluates the performance of HAMSOM with regard to the flow field and the related dynamic pressure and volume transport.

The volume-averaged kinetic energy, also called dynamic pressure, can be used to measure whether the model has reached a steady-state and how much spin-up time is required to reach this steady-state. Figure 3.16 shows the time series of the dynamic pressure at different depths in the simulated area. As the depth increases, the average dynamic pressure becomes smaller. Meanwhile, the required spin-up time becomes longer as the depth increases. For example, for the upper 50m, the dynamic pressure quickly reaches a steady-state, while for deep ocean beneath 3000m, it takes more than ten years to become stable.

The surface circulation is clockwise in January and April and counterclockwise in July and October (Figure 3.17), reflecting the well-known dominance of the monsoon with respect to the upper ocean circulation. The EICC flows equatorward during August-December and reverses its direction to poleward during February-May (Shankar et al., 1996; Shetye et al., 1996; Durand et al., 2009), as it is reasonably reproduced by HAMSOM (Figure 3.17b, d). Compared to the outer model MPIOM and the third-party ocean synthesis GECCO2, the higher horizontal

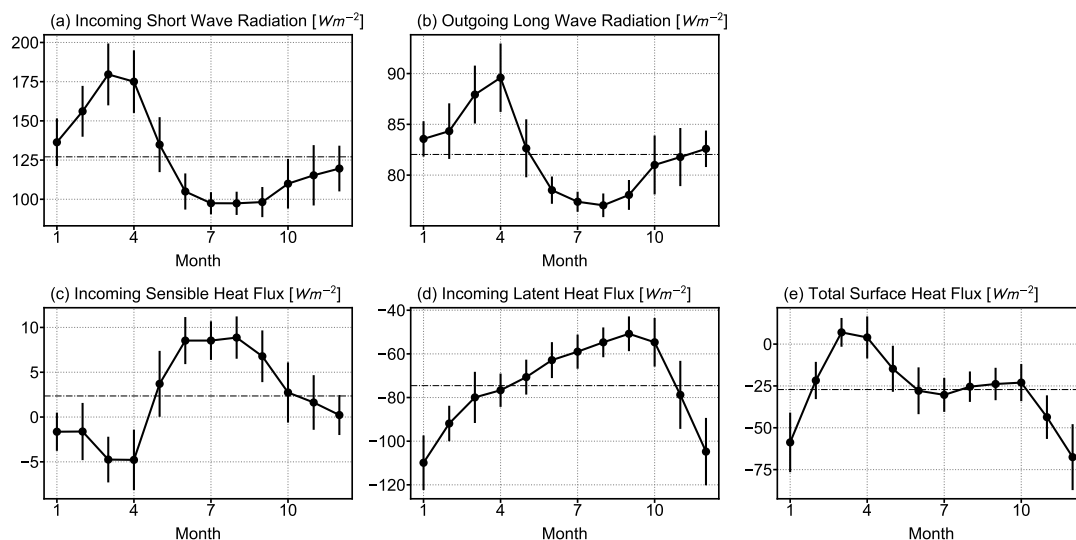


Figure 3.15: Climatological (1979-2008) annual cycle of domain-averaged incoming short wave radiation (a), outgoing long wave radiation (b), incoming sensible heat flux (c), incoming latent heat flux (d), and total surface heat flux (e). Vertical error bars represent standard deviation.

resolution of HAMSOM allows a better representation of coastal features. However, HAMSOM overestimates the current strength close to the open lateral boundaries due to the open boundary effect.

The flow field is also evaluated for a meridional section (Figure 3.18) and a zonal section (Figure 3.19). In general, the upper ocean flow simulated by HAMSOM is in good agreement with this from MPIOM and GECCO2. The direction of upper ocean currents is reversed in January and July, reflecting the dominance of the monsoon. As a consequence of the higher model resolution and more accurate bathymetry, HAMSOM performs better in coastal areas. For example, the EICC is more prominent than in GECCO2 (Figure 3.19b, d, j, l), which could be attributed to the higher resolution.

The integrated transports calculated from the HAMSOM results show a good agreement with the MPIOM results (Figure 3.20). For the inner BoB, the transports through the western section and the southern section are almost balanced. The MPIOM results show positive transports through the western section and negative transports through the southern section in summer, while the opposite is true in winter. The HAMSOM results reproduce this feature for winter, but the outflow through the southern section is weaker in summer due to the overestimated current parallel to the southern boundary.

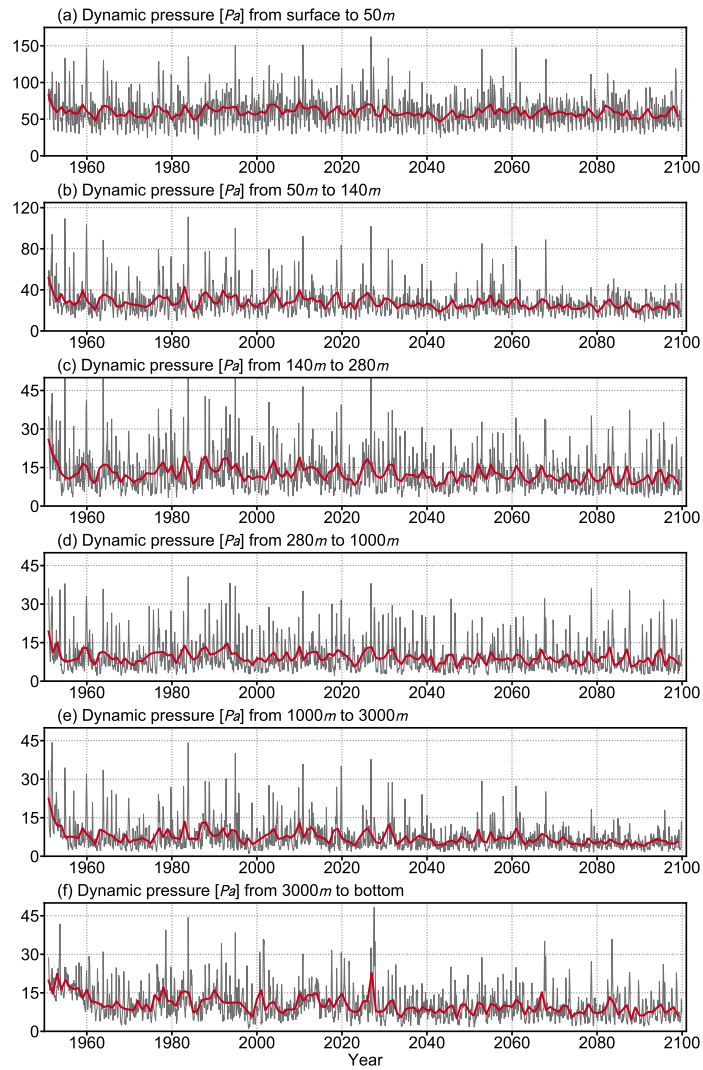


Figure 3.16: HAMSOM averaged dynamic pressure time series of the BoB for different depths. Grey line shows monthly mean. Red line shows yearly mean.

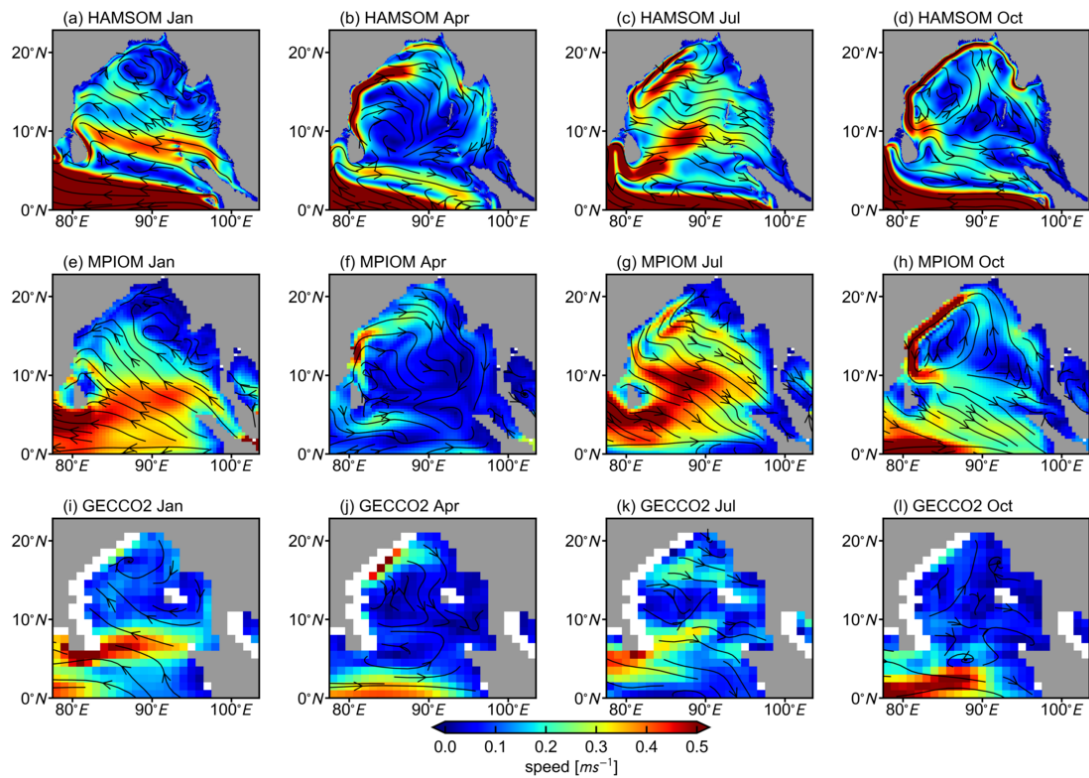


Figure 3.17: Comparison of climatological (1981-2010) monthly surface circulation for HAMSOM (a, b, c, d), MPIOM (e, f, g, h), and GECCO2 (i, j, k, l). Black lines with arrows are streamlines. Shaded colors refer to the current speed.

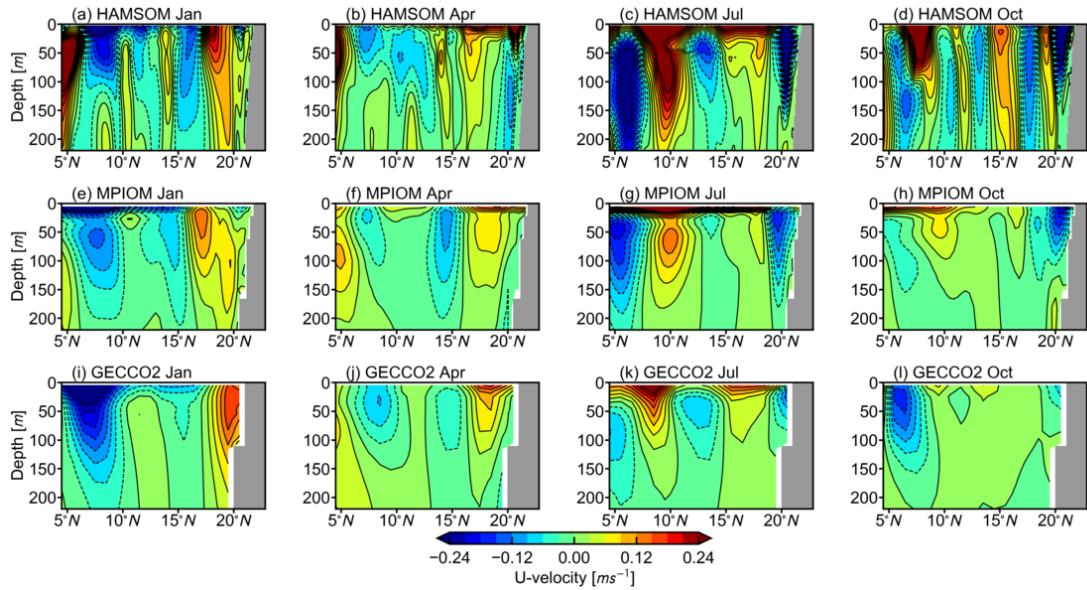


Figure 3.18: Comparison of climatological (1981-2010) monthly U-velocity (averaged over 88°E-90°E) for HAMSO (a, b, c, d), MPIOM (e, f, g, h), and GECCO2 (i, j, k, l).

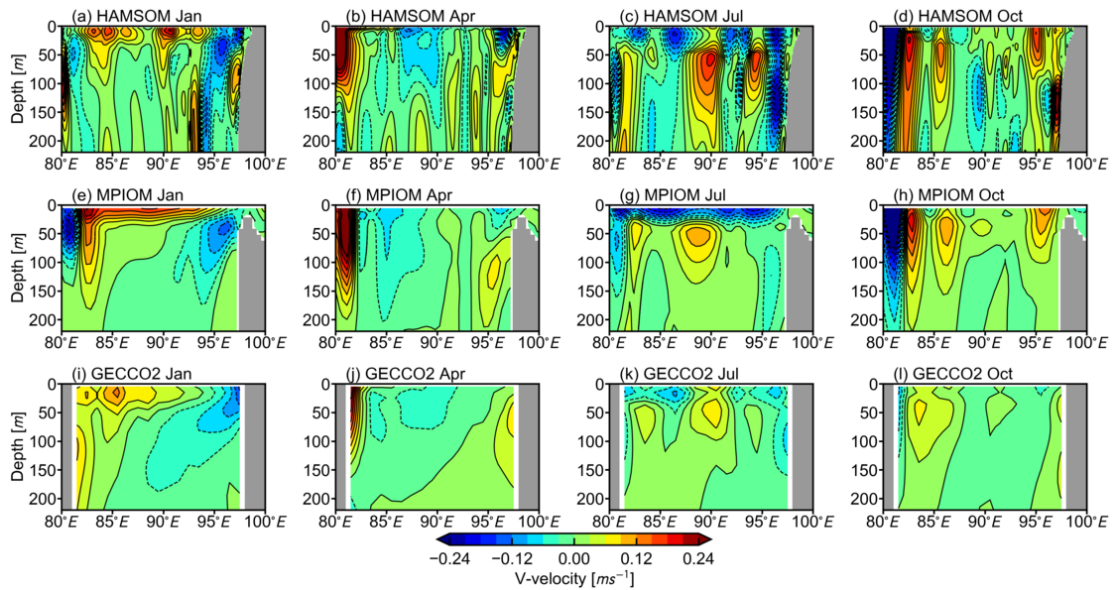


Figure 3.19: Comparison of climatological (1981-2010) monthly V-velocity (averaged over 10°N-12°N) for HAMSO (a, b, c, d), MPIOM (e, f, g, h), and GECCO2 (i, j, k, l).

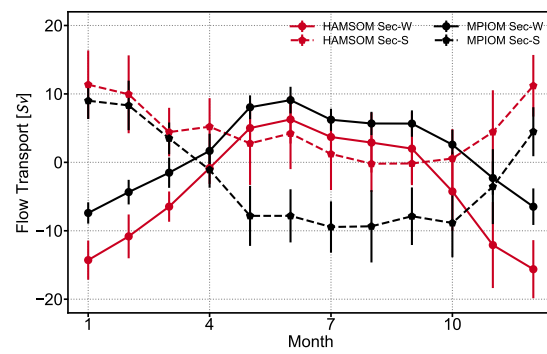


Figure 3.20: Comparison of Climatological (1981-2010) annual cycle of the upper 50m flow transport through the western section (Sec-W;  $82^{\circ}E$ ,  $2^{\circ}N$ - $22.5^{\circ}N$ ) and the southern section (Sec-S;  $2^{\circ}N$ ,  $82^{\circ}E$ - $100^{\circ}E$ ) for HAMSOM and MPIOM. Vertical error bars represent standard deviation.



## Chapter 4

# Results and Discussion

### 4.1 Correlation with External Forcing of Historical Scenario

Previous studies pointed out that remote forcing from the equatorial Indian Ocean affects the ocean circulation and thermocline in the BoB (Potemra et al., 1991; Yu et al., 1991; McCreary et al., 1993, 1996; Girishkumar et al., 2013). The related Indian Ocean Dipole (IOD) is an east-west dipole mode that dominates the interannual sea surface temperature variability in the tropical Indian Ocean (Saji et al., 1999; Webster et al., 1999; Ashok et al., 2003; Fischer et al., 2005; Schott et al., 2009; Deser et al., 2010). The study on sea level and subsurface temperature anomalies revealed a see-saw behavior of the thermocline in the tropical Indian Ocean which is related to the IOD (Saji et al., 1999). In this section, the HAMSOM experiment RCP85 results from 1951 to 2005, driven by the historical scenario, are discussed on the interannual time scale. The correlation between the BoB subsurface temperature/salinity anomalies and the external IOD signal, and the related governing mechanisms, are discussed in this section.

The dipole mode index (DMI) describes the difference in sea surface temperature anomalies between the western tropical Indian Ocean and the southeastern tropical Indian Ocean. The DMI strongly correlates with the principal component of the second EOF mode of the sea surface temperature anomalies in the tropical Indian Ocean and is considered a reliable representation of the IOD (Saji et al., 1999). The normalized time series of DMI and domain-averaged subsurface (100m) temperature/salinity anomalies are shown in Figure 4.1a. For reasons of consistency, the DMI time series is extracted from MPIOM since it is the global model used in this downscaling investigation. Anomalies used here are residuals subtracted by monthly climatology (from 1971-2000). In order to eliminate sub-seasonal variations, a 3-month running mean is applied to these monthly time series.

Lead-lag running Pearson correlation coefficients with a window of 30-year between the time series of DMI and the subsurface temperature/salinity anomaly are shown in Figure 4.1b and 4.1c. The value of the Pearson correlation determines the extent of linearity between two variables. The HAMSOM results show that the subsurface temperature anomaly of the BoB negatively

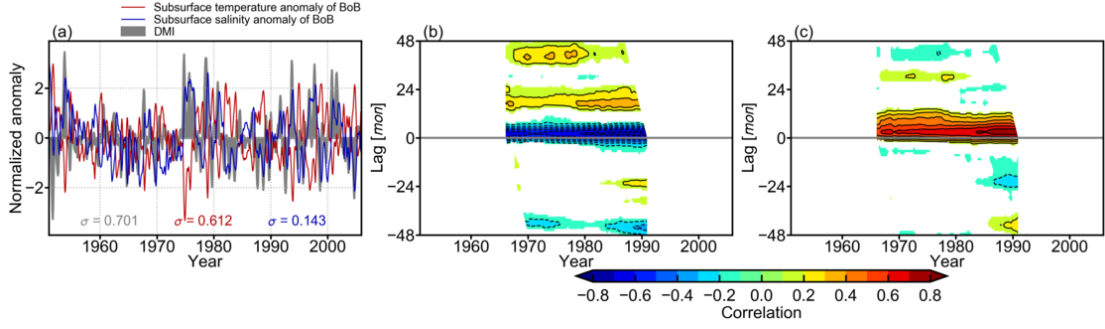


Figure 4.1: Normalized 3-month running mean of DMI, temperature anomaly and salinity anomaly at subsurface of the BoB (a). The standard deviation  $\sigma$  is labelled with the corresponding color. Lead-lag running Pearson correlation with a window of 30 years between the DMI and the subsurface temperature anomaly (b), and between the DMI and the subsurface salinity anomaly (c). Only significant correlation coefficients with  $p$  - value  $< 0.05$  are shaded.

correlates to the DMI with a notable lag of about three months on average, while the subsurface salinity anomaly of the BoB positively correlates to the DMI. The maximum absolute correlation is close to 0.8, representing high linearity between the external signal IOD and the BoB subsurface temperature/salinity variability.

To further examine this correlation, relevant results from the global model MPIOM, the third-party ocean synthesis GECCO2, and the observation-based EN4, are shown in Figure 4.2. The results from MPIOM and GECCO2 support the correlation revealed by HAMSOM. However, the results from EN4 only show a relatively weak correlation between the DMI and the subsurface temperature anomaly of the BoB. The subsurface salinity anomaly from 1951 to 1956 shows artificial oscillations (Figure 4.2g). As discussed in the previous chapter, there is a weight index from 0 to 1 defined in EN4, which represents the total weighting given to the observation increments when forming the analyses. The mean weight of BoB is 0.57 for the subsurface temperature, but only 0.22 for the subsurface salinity, indicating the lack of salinity observations.

Meanwhile, by comparing the DMI correlation magnitudes obtained from different data sets, it can be seen that the correlation is stronger when the data set shows a lower degree of freedom. For example, HAMSOM has a lower degree of freedom than MPIOM because it is a regional ocean model without ocean-atmosphere feedback processes. GECCO2 has a higher degree of freedom because assimilation processes are included. EN4 has the highest degree of freedom of these four data sets because it is based on observations.

Figure 4.3 shows the correlation between the DMI and the temperature/salinity anomalies of the BoB at different depths for HAMSOM and other data sets. The Argo-based RG\_Clim is also introduced, but its period only spans from 2004 to 2018 that is different compared to other data sets. Except for EN4, the other four data sets show that the BoB temperature/salinity anomaly at subsurface is strongly correlated with the DMI. For the BoB temperature anomaly, except for the negative correlation at a depth of 100m, significant positive correlations with a lag about 12

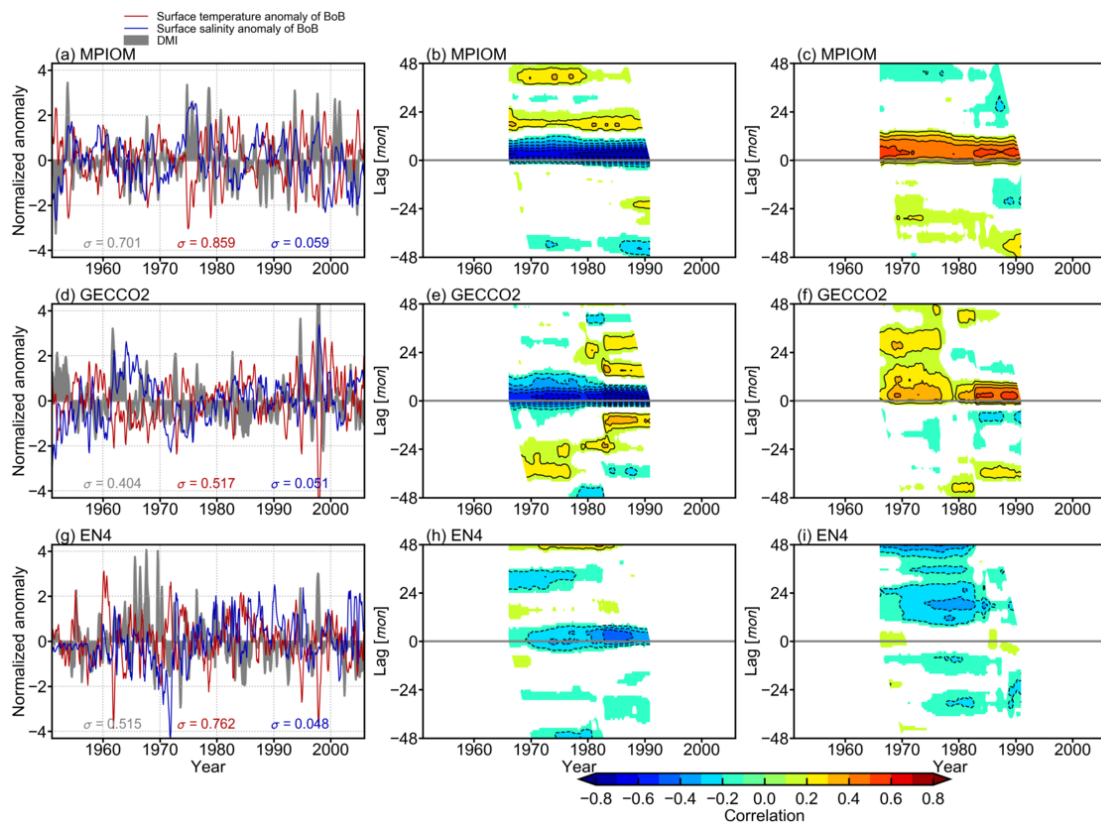


Figure 4.2: As in Figure 4.1, but for results from MPIOM (a, b, c), GECCO2 (d, e, f), and EN4 (g, h, i).

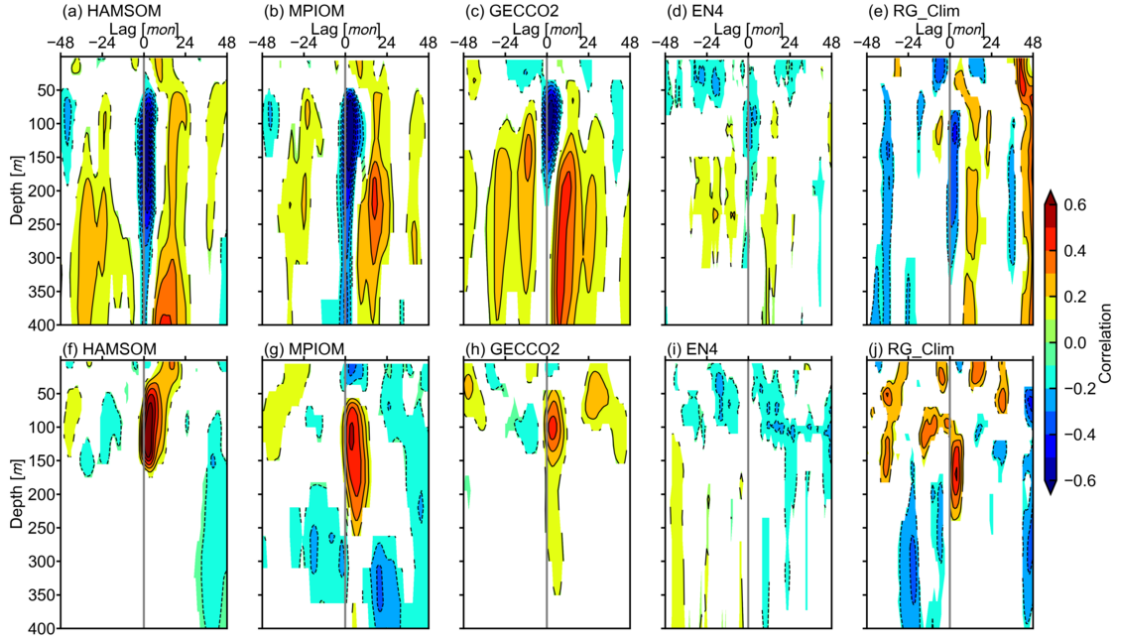


Figure 4.3: Lead-lag Pearson correlation between the DMI and the BoB temperature anomalies at different depths from HAMSOM (a), MPIOM (b), GECCO2 (c), EN4 (d), and RG\_Clim (e), respectively. The second row is as in the first row, but for the correlation between the DMI and the BoB salinity anomalies. Analysis period is from 2004 to 2018 for RC\_Clim and from 1960 to 2005 for others.

months can also be observed below 150m. The results suggest that the depth range correlated to the DMI is broader for the temperature anomaly than for the salinity anomaly. For the BoB salinity anomaly, the significant positive correlation appears below 50m, and it is possible to be as deep as 250m. On average, salinity correlations reach the maximum at a three-month delay. No apparent correlation is observed for the sea surface. The local intense wind-induced mixing and other surface factors that are not closely related to the IOD could be the reasons for this missing correlation of the upper 50m of the BoB.

To more closely analyze the response of the subsurface temperature/salinity in the BoB to the IOD, the composites of subsurface temperature/salinity anomalies during ASO, NDJ, FMA, and MJJ, of positive IOD years (pIOD) and negative IOD years (nIOD), are shown in Figure 4.4 and 4.5. Five pIOD years (1974, 1978, 1993, 1997, 2000) and five nIOD years (1979, 1988, 1992, 1998, 2004) can be identified from the normalized DMI time series (Figure 4.1a), by looking at years with maxima above two and years with minima below minus two. These extremes are all located around September. For the subsurface temperature anomalies, the pattern is opposite during pIOD and nIOD events in ASO, as well as in NDJ when IOD events end. This opposing behavior is becoming weaker over time, which can be seen in particular for FMA and MJJ. When a pIOD (nIOD) event happened in the tropical Indian Ocean, areas near the BoB coasts first show large and statistically significant negative (positive) temperature anomalies (Figure

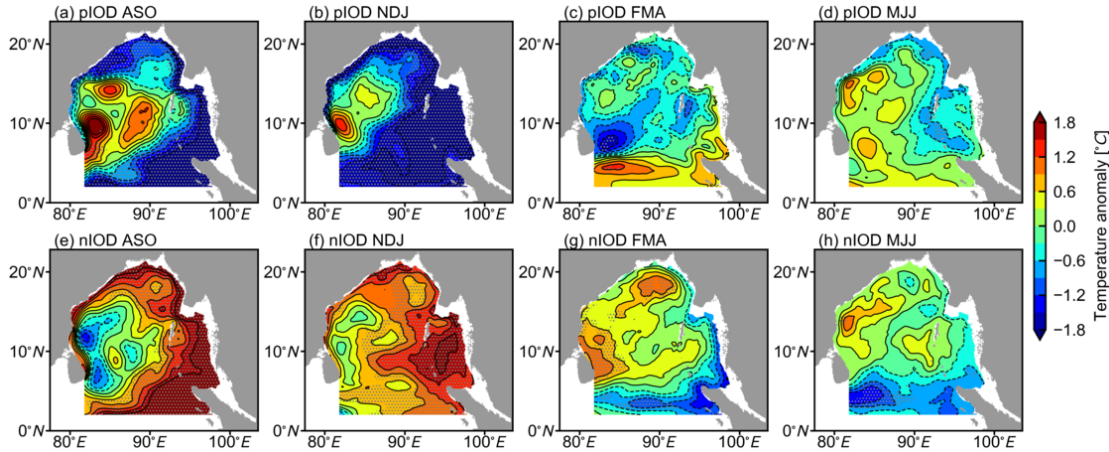


Figure 4.4: Composite of subsurface temperature anomalies during ASO (a, e), NDJ (b, f), FMA (c, g), and MJJ (d, h), of pIOD and nIOD years, respectively. Anomalies significant at the 95% confidence level by a two-tailed Welch's t-test are hatched with grey dots.

4.4a, e). Next, these large anomalies appear in most areas of the eastern basin but in the western basin they are limited to the coastal areas (Figure 4.4b, f). For the subsurface salinity anomalies, a similar development can also be observed (Figure 4.5a, b, e, f). Its development is consistent with the characteristics of coastal Kelvin waves and westward moving Rossby waves. First, the subsurface disturbance signals in the eastern equatorial Indian Ocean related to the IOD propagate counterclockwise along the BoB coasts in the form of coastal Kelvin waves. Subsequently, these signals are reflected at the eastern boundary and propagate westward into the basin interior. The coastal Kelvin waves travel fast (Moore and McCreary, 1990; Cheng et al., 2013), explaining why the related significant anomalies first appear near the coasts. The reflected Rossby waves are predominantly moving westward with a relatively slow speed, explaining why the signal near the western boundary seems to be trapped and why even the domain-averaged subsurface temperature/salinity anomaly lags the DMI.

Figure 4.6 presents a similar plot as Figure 4.3, but for HAMSOM subareas. The closer the subarea is to the eastern boundary, the stronger the correlation is between the DMI and the local temperature/salinity anomalies. For the subarea WBB which is located close to the western boundary, the correlation is weakest (Figure 4.6d, j), while the composite results show statistically significant anomalies along the western boundary (Figure 4.4 and Figure 4.5), indicating that the subarea WBB does not receive information from the coastal Kelvin wave but only get the weakened signal from the westward moving Rossby wave.

Daily data from HAMSOM is used for tracking Rossby waves (Figure 4.7, 4.8). The positive temperature anomalies show a westward moving Rossby wave signal in the daily climatological subsurface temperature (Figure 4.7a). This signal takes approximately four to five months to cross the basin zonally. Positive temperature anomalies already appear at the western boundary before the westward Rossby wave has approached. The water in a narrow band at the western boundary shows a strong agreement with the water at the eastern boundary, suggesting that

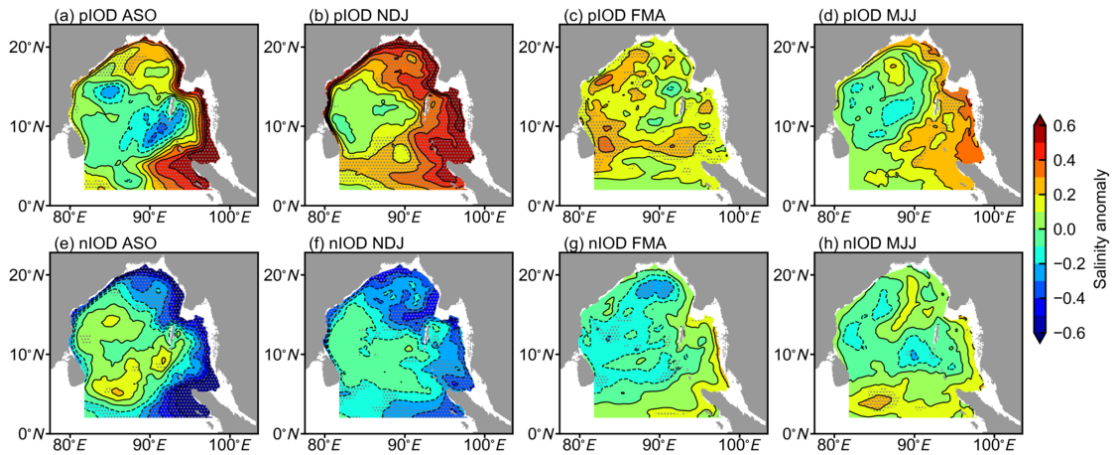


Figure 4.5: As in Figure 4.4, but for subsurface salinity anomalies.

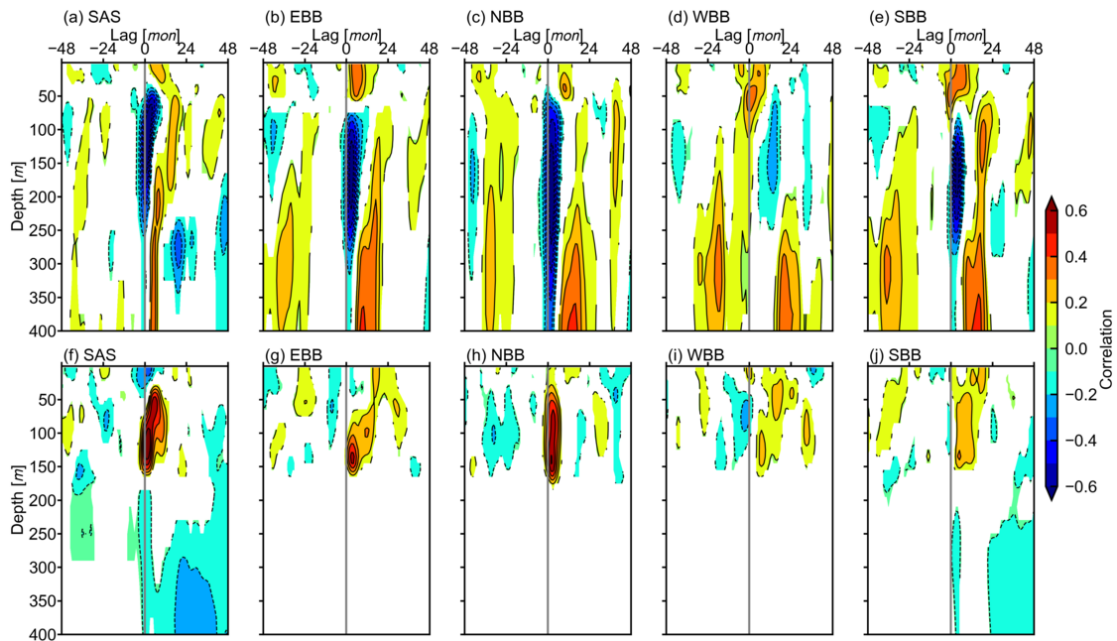


Figure 4.6: Lead-lag Pearson correlation between the DMI and the temperature anomaly of subareas SAS (a), EBB (b), NBB (c), WBB (d), and SBB (e), respectively, at different depths. The second row is as in the first row, but for the correlation between the DMI and the salinity anomaly. Analysis period is from 1960 to 2005. Only significant correlation coefficients with  $p$ -value  $< 0.05$  are shaded.

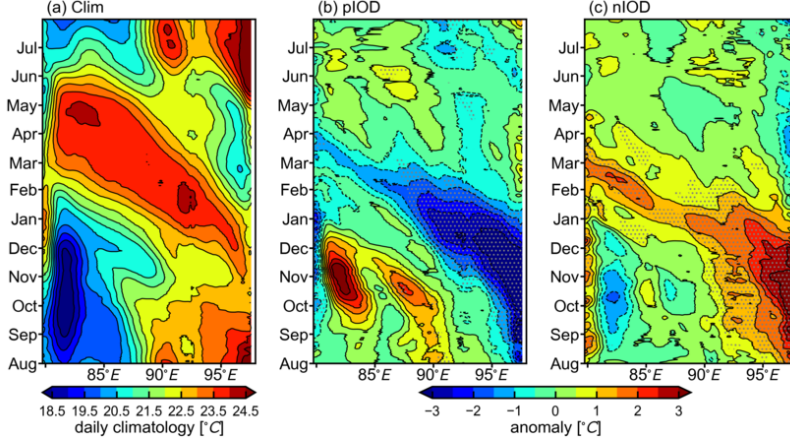


Figure 4.7: Hovmöller diagram of daily climatological (1971-2000) subsurface temperature (a; averaged over  $10^{\circ}N$  to  $12^{\circ}N$ ), composite of subsurface temperature anomalies for pIOD (b) and for nIOD (c). Anomalies significant at the 95% confidence level by a two-tailed Welch's t-test are hatched with grey dots.

fast traveling coastal Kelvin waves dominate the coastal areas in the BoB. More details of the coastal Kelvin waves are presented in the next section. In pIOD and nIOD years, the propagation features of coastal Kelvin waves and westward Rossby waves are essentially the same as the climatology but carrying negative and positive anomalies, respectively (Figure 4.7b, c). The statistically significant anomalies first appear at the eastern boundary, then at the western boundary, subsequently in the basin interior, indicating that the extreme IOD signal propagates to the entire BoB by coastal Kelvin waves and westward Rossby waves. The analysis of the subsurface salinity also supports these mechanisms (Figure 4.8).

To further investigate the role of advection and diffusion in this correlation, related terms are directly outputted during the HAMSOM simulation. Only the advection and diffusion of salinity are discussed here to simplify the presentation. The salinity budget can be written as follows:

$$\frac{\partial S}{\partial t} = -u \frac{\partial S}{\partial x} - v \frac{\partial S}{\partial y} - w \frac{\partial S}{\partial z} + \frac{\partial}{\partial x} \left( \kappa_H \frac{\partial S}{\partial x} \right) + \frac{\partial}{\partial y} \left( \kappa_H \frac{\partial S}{\partial y} \right) + \frac{\partial}{\partial z} \left( \kappa_V \frac{\partial S}{\partial z} \right), \quad (4.1)$$

where  $S$  is salinity,  $u$ ,  $v$ , and  $w$  are zonal, meridional, and vertical velocity,  $\kappa_H$  and  $\kappa_V$  are horizontal and vertical diffusion coefficients. The left side represents the salinity tendency (ST). The right side from left to right represents the salinity change rate of zonal (UADV), meridional (VADV), vertical (WADV) advection, and of zonal (UDIF), meridional (VDIF), vertical (WDIF) diffusion, respectively.

Figure 4.9 shows the salinity budget of the BoB at 100m depth during ASO. At this depth, the advection terms are much larger than the diffusion terms, and the vertical diffusion term is larger than the horizontal diffusion terms. The sum of three advection terms becomes much smaller and about the same magnitude as the salinity tendency and the vertical diffusion. All advection terms show significant differences for pIOD and nIOD events compared to the climatology. Meanwhile, on the average for the entire BoB, the vertical advection contributes positively to the positive

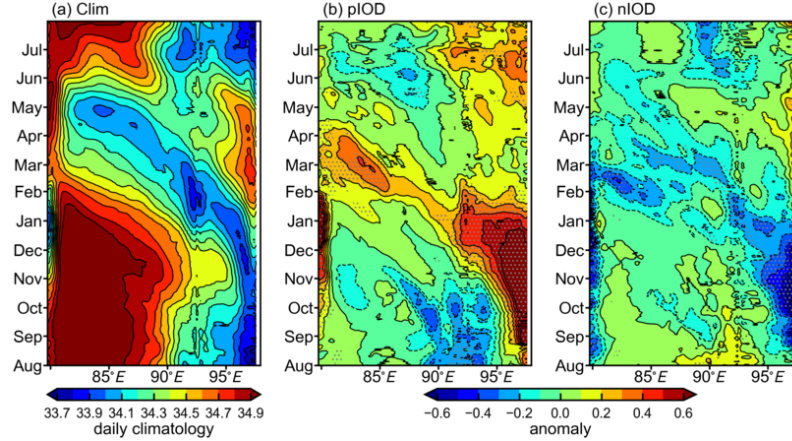


Figure 4.8: As in Figure 4.7, but for subsurface salinity.

salinity tendency of pIOD and the negative salinity tendency of nIOD. In contrast, the summed-up horizontal advection contributes negatively.

The domain-averaged advection terms at different depths are shown in Figure 4.10. For the entire BoB, three advection terms show significant differences for most depths at pIOD and nIOD events compared to the climatology. Except for subarea SAS which shows significant differences in horizontal advection change rate for pIOD events, all other areas show differences which do not pass the significance test. However, the differences in vertical advection are significant except for the subarea NBB. Figure 4.11 shows the domain-averaged diffusion terms at different depths. The horizontal diffusion terms are small and can be ignored. The vertical diffusion term shows large values only near the sea surface. For depths below 50m, the vertical diffusion term is also negligible.

Figure 4.12 shows the sum of advection terms, the sum of diffusion terms, and the final salinity tendency at different depths. For the entire BoB as well as for all subareas, the results show that the salinity tendency is dominated by diffusion processes near the surface, while advection processes dominate the tendency at the subsurface. Wind-induced mixing can explain the dominance of diffusion near the surface. The salinity tendency shows a subsurface salinity increase (decrease), indicating a positive (negative) anomaly for pIOD (nIOD) events, which shows an apparent response to the IOD signal (Figure 4.12m, n, o). The salinity change rate due to advection shows more obvious responses at the subsurface during extreme IOD events, suggesting that the correlation discussed in this section is mainly caused by advection processes.

In conclusion, a delayed correlation between the subsurface temperature/salinity anomaly of the BoB and the IOD is revealed. On average, a lag of three months shows the strongest correlation. The HAMSOM model reveals that coastal Kelvin waves and westward moving Rossby waves connect the interannual variabilities in the tropical Indian Ocean surface and the BoB subsurface. The salinity budget determined in HAMSOM indicates that the advection processes' contribution plays a dominant role in this correlation. Notably, the vertical advection shows a positive contribution, while the horizontal advection shows a negative contribution.

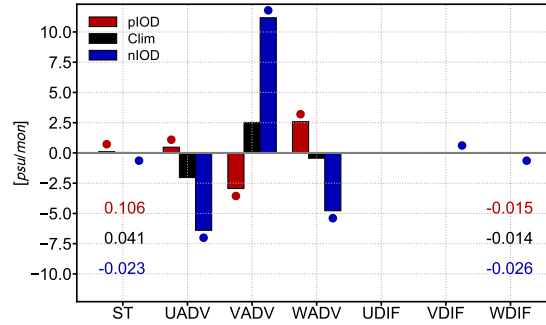


Figure 4.9: Domain-averaged subsurface salinity tendency and related salinity change rate terms of the BoB during ASO of pIOD years, nIOD years, and climatological (1971-2000) period, respectively. The values of ST and WDIF in different cases are labelled with the corresponding color. Dots with corresponding color indicate that they are significant different at the 95% confidence level by a two-tailed Welch's t-test compared to the climatology.

During pIOD events, intensified upwelling occurs in the eastern Indian Ocean (Nyadjro and McPhaden, 2014; Chen et al., 2016), uplifting cold saltier water along the eastern boundary. This anomaly in turn induces coastal Kelvin waves, which are reflected at topographic disturbances, inducing Rossby waves that move westward to the basin interior. Through this chain of processes, the interannual subsurface temperature/salinity variability in the BoB is remotely modulated by the external IOD signals in the tropical Indian Ocean.

## 4.2 Long-term Trend of RCP8.5 Scenario

In this section, HAMSOM experiment RCP85 results from 1980 to 2099, driven by the historical scenario from 1980 to 2005 and the RCP8.5 scenario from 2006 to 2099, are discussed. The total of 120 years data can be divided into four 30-year periods, of which the first 30 years represents the current climate state, and the next three 30 years represent the future climate state under the RCP8.5 scenario.

### 4.2.1 Sea Level Height

As a regional ocean model, HAMSOM is not the best choice for projecting the absolute sea level rise in the BoB under the high emissions pathway, but it can still be used to discuss the sea surface height distribution. The model results show that, on the 30-year average, the sea level in the western basin is higher than in the eastern basin. This overall distribution keeps unchanged under the RCP8.5 scenario (Figure 4.13). However, the standard deviations of climatological monthly data in the basin interior show an increase with time (Figure 4.13e, f, g, h), suggesting that the seasonal variability of sea level height will be enhanced under the high emissions pathway.

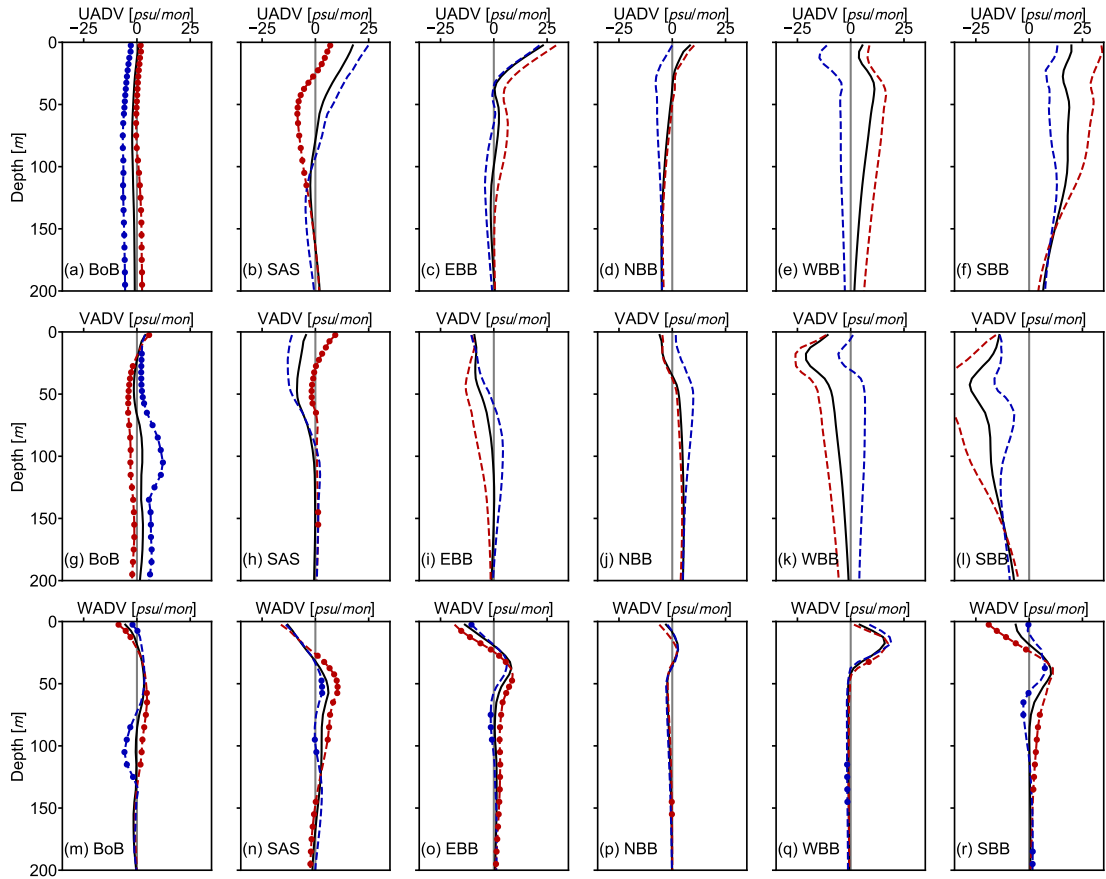


Figure 4.10: Domain-averaged UADV at different depths of the BoB (a) and subareas (b, c, d, e, f) during ASO. Black solid line is for the climatology (1971-2000); red and blue dashed line is for the composite of pIOD and nIOD years, respectively. Dots with corresponding color indicate that they are significant different at the 95% confidence level by a two-tailed Welch's t-test compared to the climatology. The second and third row as in the first row, but for VADV and WADV, respectively.

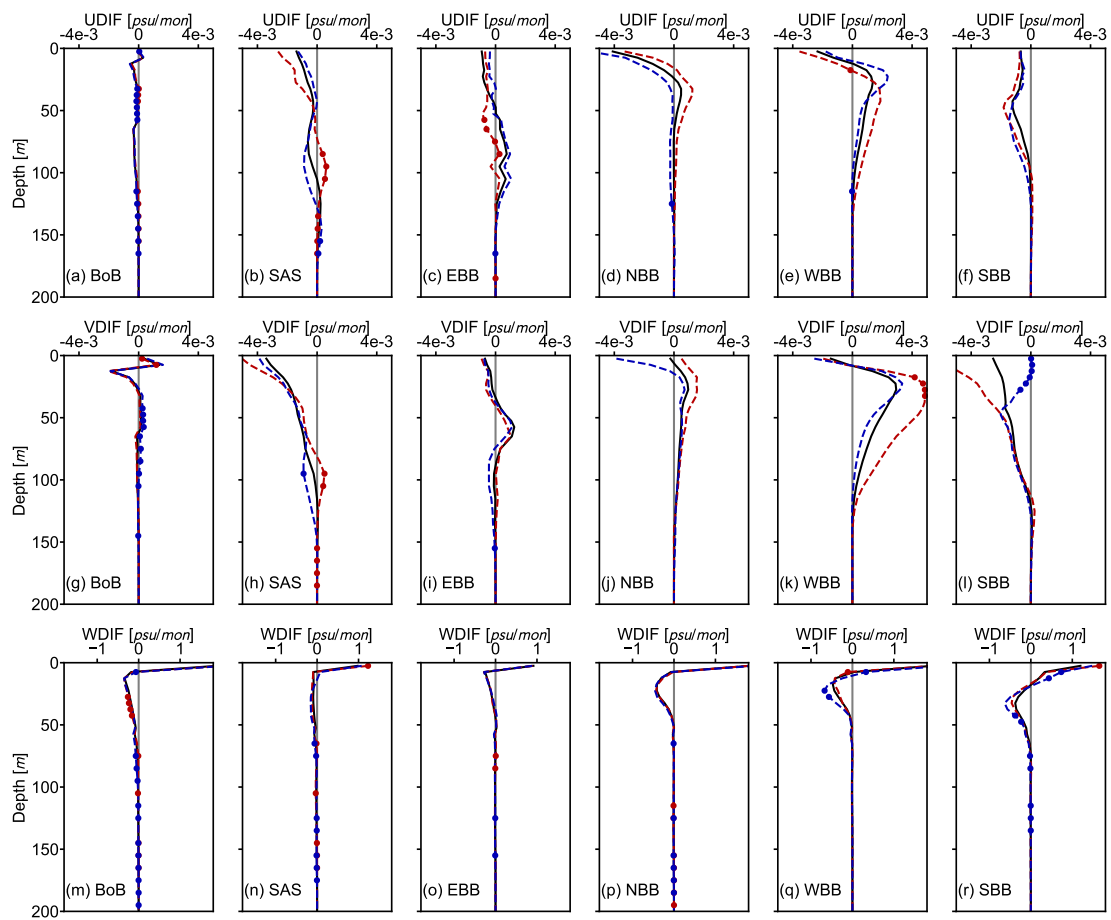


Figure 4.11: As in Figure 4.10, but for UDIF (first row), VDIF (second row), and WDIF (third row), respectively.

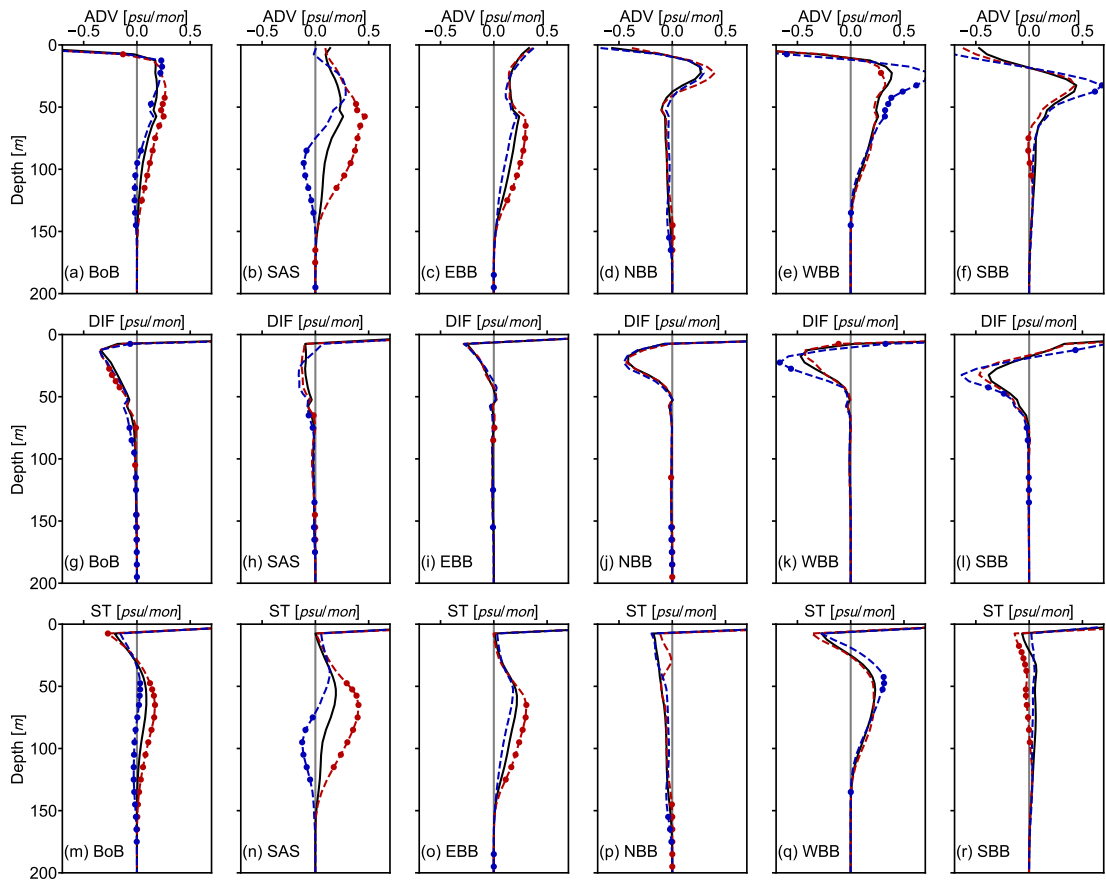


Figure 4.12: As in Figure 4.10, but for the sum of advection terms (first row), the sum of diffusion terms (second row), and the salinity tendency (third row), respectively.

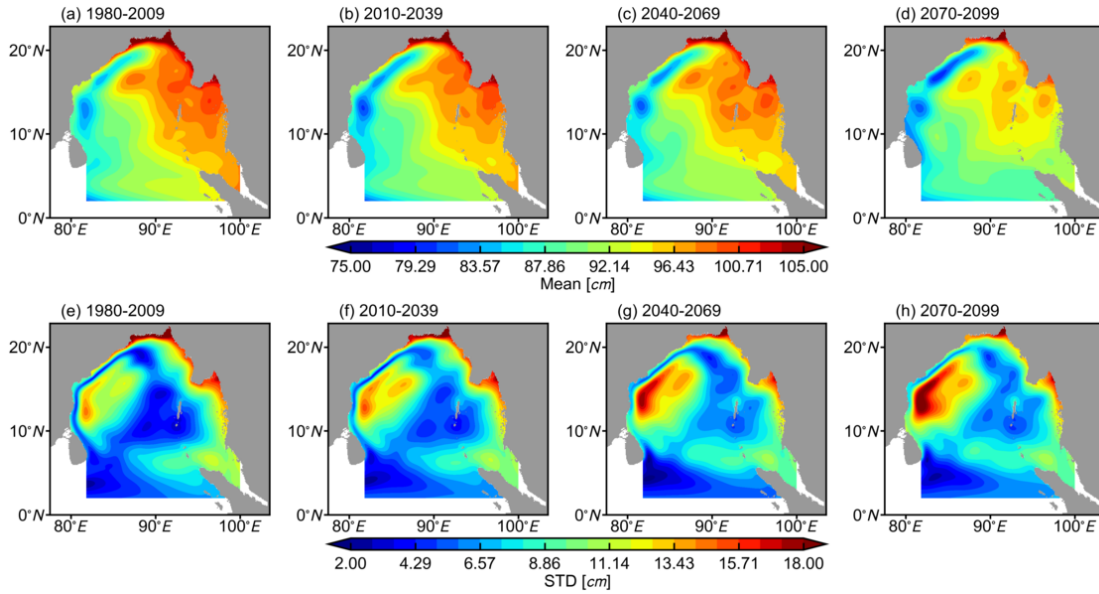


Figure 4.13: 30-year average of sea level height for the period 1980-2009 (a), 2010-2039 (b), 2040-2069 (c), and 2070-2099 (d), respectively. The standard deviation of climatological monthly sea level height for each period is shown in the second row.

#### 4.2.2 Water Temperature

As mentioned in the previous chapter, the BoB domain-averaged sea surface temperature simulated by HAMSOM shows the same warming trend as the global forcing model MPIOM (Figure 3.9). Figure 4.14 shows a spatial difference in the magnitude of sea surface warming. The central region of the BoB shows the most significant temperature increase. The temperature increase is relatively small near the western and eastern boundaries and smallest near the equator. The standard deviations of climatological monthly sea surface temperatures are getting larger with time in most areas of the BoB, especially in the northern and central basin, indicating the enhancement of sea surface temperature seasonal variabilities.

For the subsurface temperature at a depth of  $100m$ , the results of HAMSOM generally suggest a warming trend (Figure 4.15). At this depth, on average, the water is cold in the western basin and warm in the eastern and southern basin, which is significantly different from the temperature distribution of the sea surface. This cold water area is believed to be a consequence of the East India Coastal Current and the associated upwelling. For the period 2010-2039, The subsurface water along the western boundary becomes colder than in the current state, reflecting the complicated dynamics at the thermocline mentioned in the previous section. For the long-term trend, the subsurface water still shows a warming trend for most areas of the BoB. The most significant increase in mean temperature is mainly concentrated in the northeast of Sri Lanka. In contrast, the most significant enhancement in seasonal changes is concentrated in the area affected by the western boundary current.

Figure 4.16 shows the yearly time series and the 30-year running mean of the domain-averaged

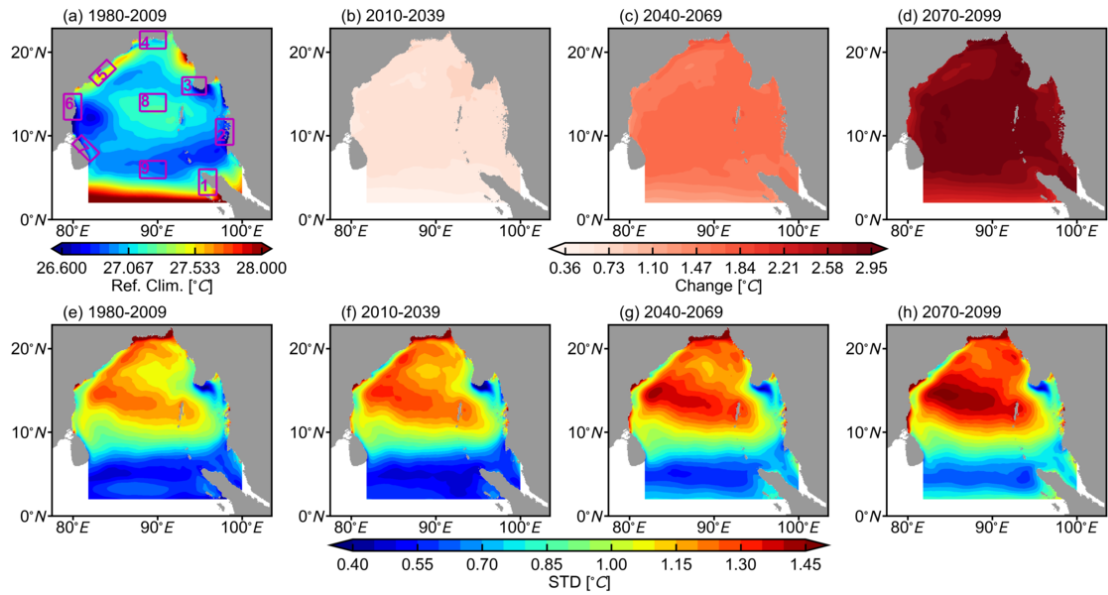


Figure 4.14: 30-year average of sea surface temperature for the period 1980-2009 (a). Changes of temperature compared to (a) are shown in (b) for 2010-2039, (c) for 2040-2069, and (d) for 2070-2099, respectively. The standard deviation of climatological monthly sea surface temperature for each period is shown in the second row. Nine subareas are marked by black boxes.

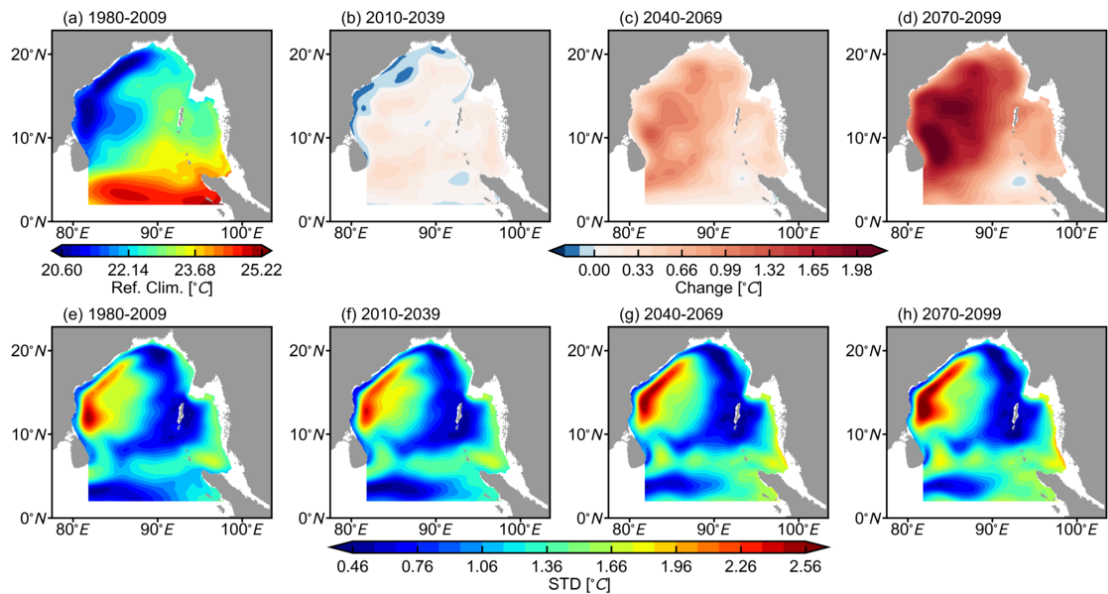


Figure 4.15: As in Figure 4.14, but for the subsurface temperature.

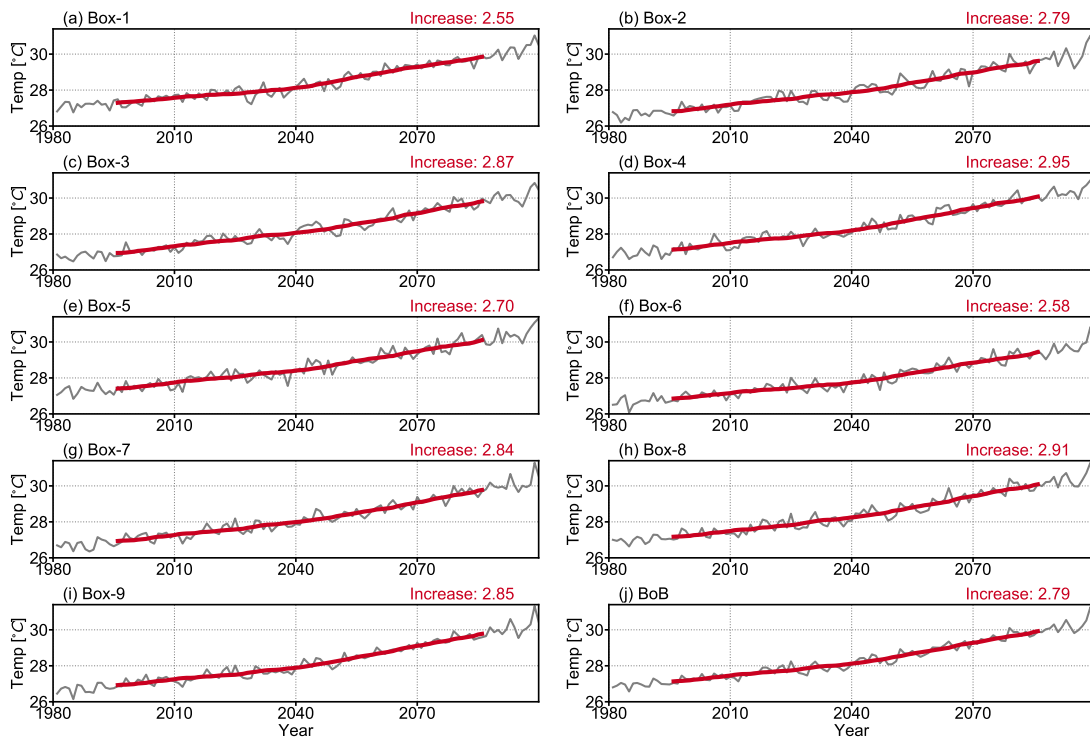


Figure 4.16: Yearly time series (grey line) and 30-year running mean (red line) of domain-averaged sea surface temperature for subareas (a, b, c, d, e, f, g, h, i) and the entire BoB (j). The temperature increase from the first 30-year mean to the last 30-year mean is labelled.

sea surface temperature for subareas (marked in Figure 4.14a) and the entire BoB. All yearly time series show a clear upward trend with small oscillations. By calculating the temperature difference between the last 30-year mean and the first 30-year mean, the results show that, under the RCP8.5 scenario, the sea surface temperature in the BoB will rise by 2.55 to 2.91 °C at the end of the 21st century compared to the current climate state. However, this warming trend does not always show-up in the subsurface (Figure 4.17). The annual oscillation of temperature at a depth of 100m is more significant than that of surface temperature. Until the end of the 21st century, the water at this depth will rise by 0.39 to 1.52 °C.

Figure 4.18 shows diagrams of the time required for the temperature to increase at different depths in the entire BoB predicted by the downscaled HAMSOM results and the global MPIOM results. These two models show a similar sandwich structure. The warming is fastest for the surface layer. As the depth increases from the surface to the thermocline depth about 100m, the time increased. However, for the layers below the thermocline to a depth of approximately 300m, the warming becomes faster again with increasing depth. This sandwich structure is believed to be a consequence of complicated subsurface dynamics that affect the heat transfer and weaken the warming at the thermocline. More studies are required for investigating the detailed processes of how subsurface dynamics modulate the heat transfer and affect the heating

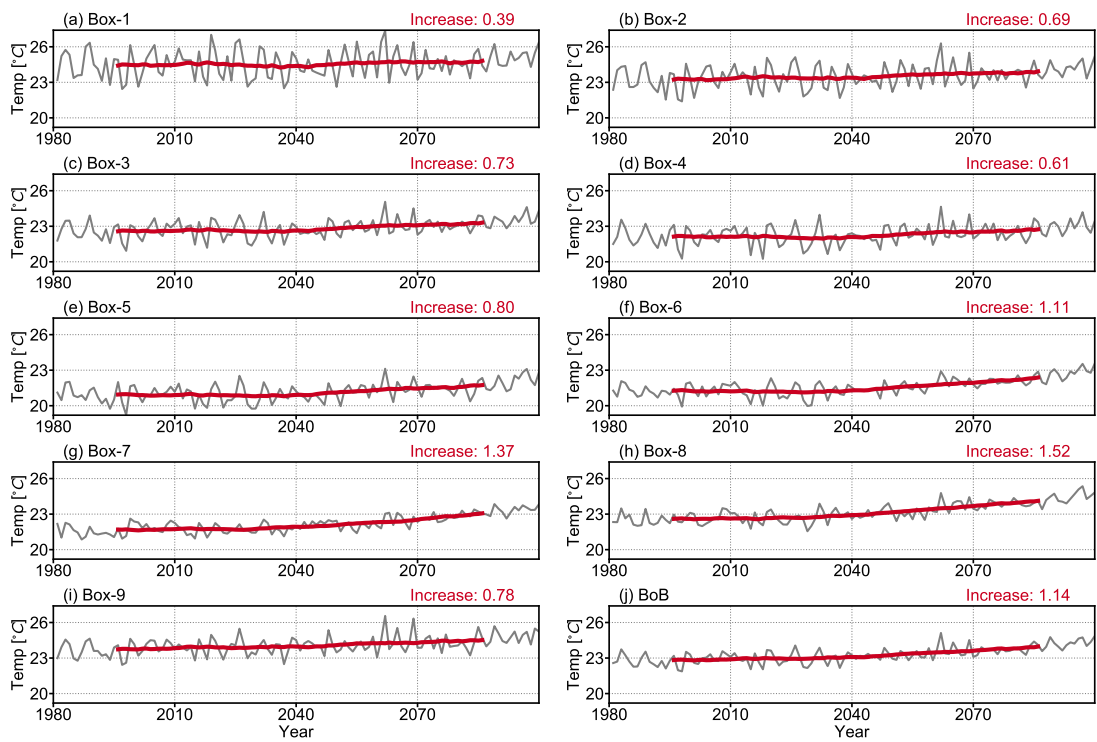


Figure 4.17: As in Figure 4.16, but for the subsurface temperature.

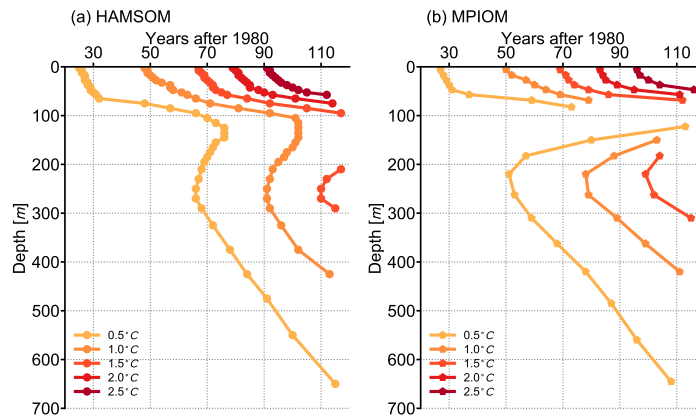


Figure 4.18: The time required for the temperature to increase at different depths of the BoB predicted by HAMSOM (a) and MPIOM (b).

rate. Compared to MPIOM, the downscaled HAMSOM results are expected to be more reliable since the forcing data is bias-corrected. The results of HAMSOM exhibit a  $1\text{ }^{\circ}\text{C}$  warming at a depth of  $100\text{m}$ , while MPIOM does not show any significant warming, indicating that the strength of stratification may play an important role for the heat transfer.

### 4.2.3 Salinity

The sea surface salinity of the BoB also shows a significant long-term trend (Figure 4.19). In general, the surface seawater is fresher near the coast and saltier close to the central basin and the southern boundary, reflecting the influence of freshwater from rivers. Compared to the current climate state, at the end of the 21st century, the surface seawater becomes saltier in the western basin and fresher in the eastern basin, resulting in a smaller horizontal salinity gradient. The maximum increase in salinity occurs mainly along the western boundary, reaching  $0.5\text{psu}$ . The maximum decrease in salinity mainly occurred in the areas affected by the inflow of the Irrawaddy and Salween rivers, reaching up to  $1.6\text{psu}$ . The surface salinity reduction in the eastern basin is mainly attributed to the increase in river discharge and precipitation (Figure 2.19c and Figure 2.22). In contrast, the subsurface salinity increase in the western basin is believed to be a result influenced by the local upwelling (4.20). The standard deviations suggest that the seasonal variability in sea surface salinity exhibits an increasing trend, especially at the estuaries of the Irrawaddy and Salween rivers.

At the subsurface ( $100\text{m}$ ), the seawater is generally saltier in the entire basin (Figure 4.20). The projected results suggest a tendency to become salty in the entire basin, especially in areas close to the continental slope and the eastern basin. The maximum increase can reach  $0.65\text{psu}$ . However, unlike the subsurface temperature, the seasonal variability of the subsurface salinity shows a weakened trend.

Figure 4.21 shows the yearly time series and 30-year running mean of domain-averaged sea surface salinity for different subareas (marked in Figure 4.14a) and the entire BoB. Only the

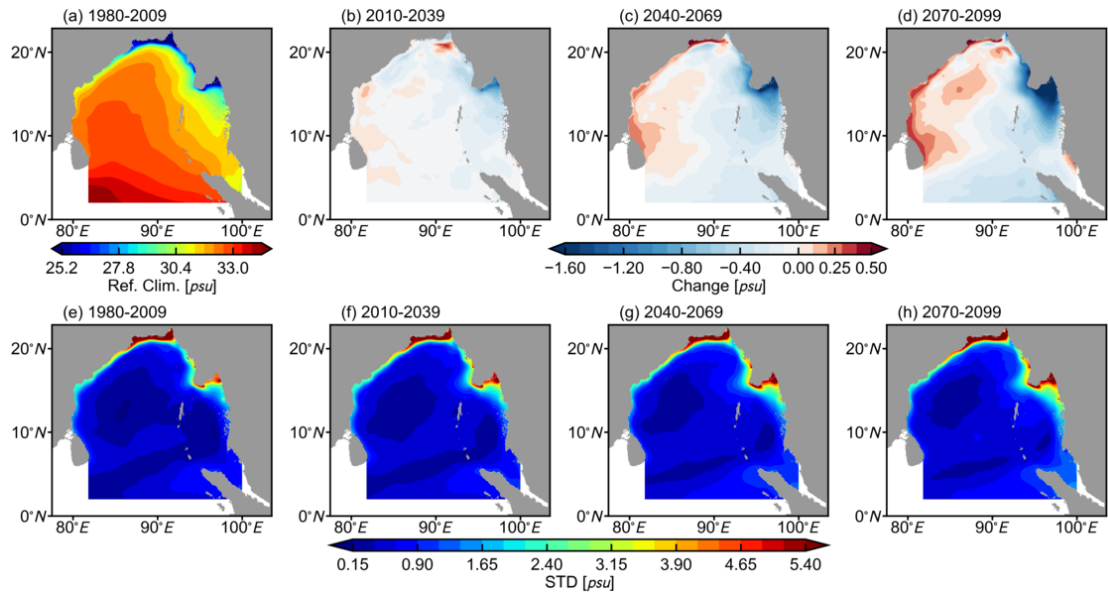


Figure 4.19: 30-year average of sea surface salinity for the period 1980-2009 (a). Changes of salinity compared to (a) are shown in (b) for 2010-2039 (b), (c) for 2040-2069, and (d) for 2070-2099, respectively. The standard deviation of climatological monthly sea surface salinity for each period is shown in the second row.

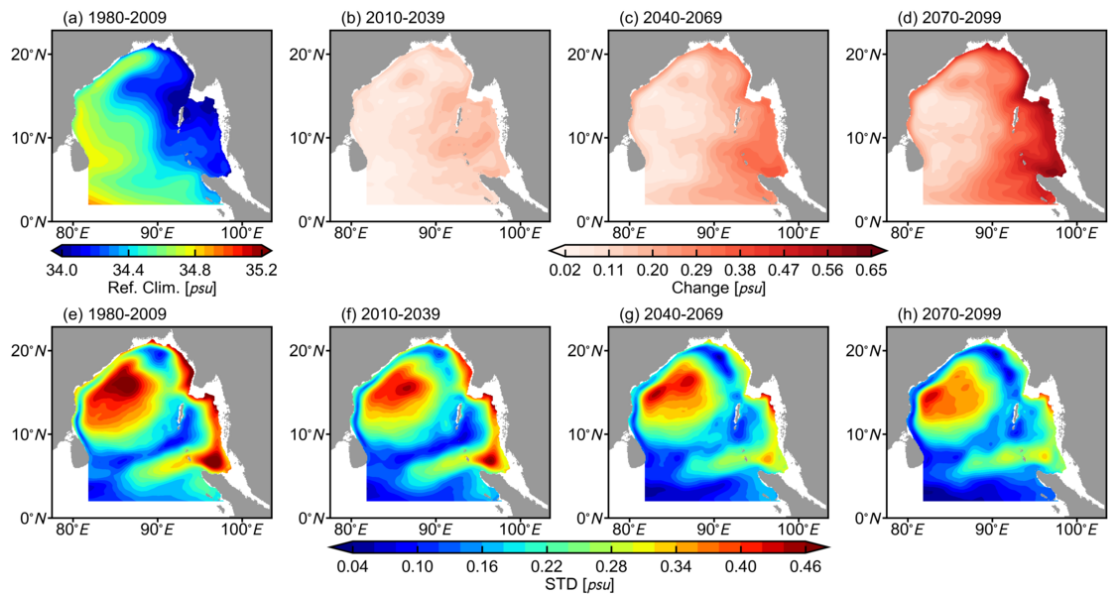


Figure 4.20: As in Figure 4.19, but for the subsurface salinity.

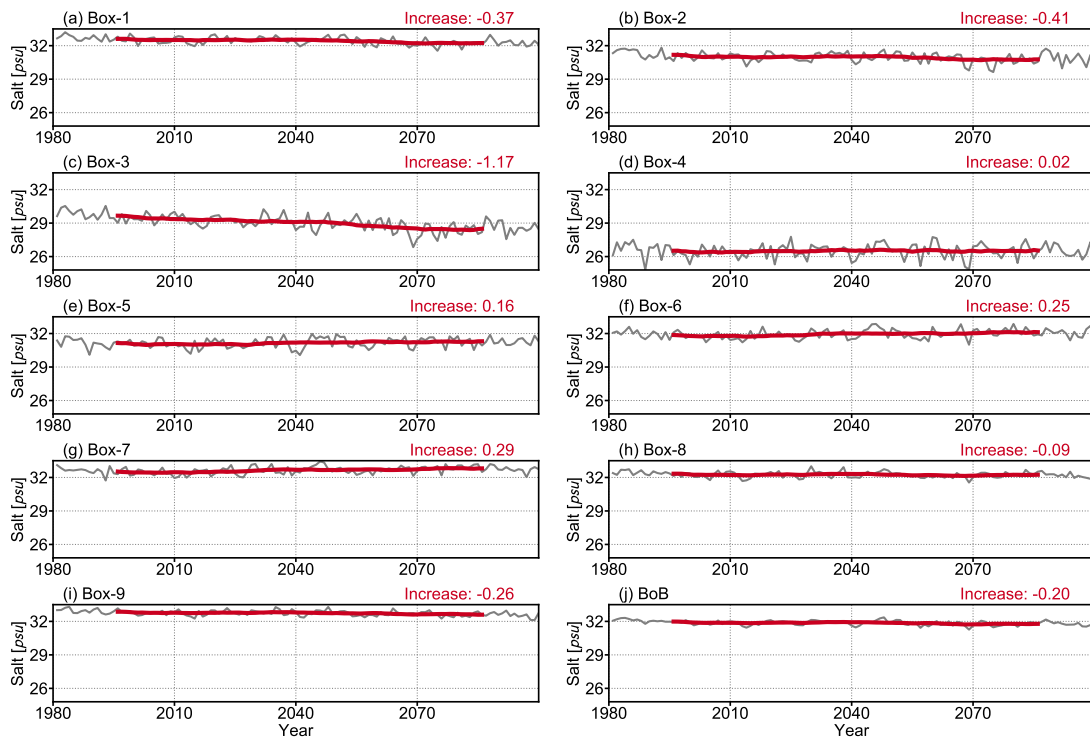


Figure 4.21: Yearly time series (grey line) and 30-year running mean (red line) of domain-averaged sea surface salinity for subareas (a, b, c, d, e, f, g, h, i) and the entire BoB (j). The salinity difference between the last 30-year mean to the first 30-year mean is labelled.

subarea near the estuaries of the Irrawaddy and Salween rivers shows a considerable downward trend (Figure 4.21c). The magnitude of annual oscillations is generally more significant than that of the long-term change from the first 30-year to the fourth 30-year period. For the entire BoB, the long-term sea surface salinity variability shows a slight downward trend with a  $0.2\text{psu}$  decrease (Figure 4.21j). For the subsurface salinity at a depth of  $100\text{m}$ , all subareas and the entire BoB show a long-term upward trend (Figure 4.22). The long-term change from the first 30-year to the fourth 30-year period is also generally smaller than the magnitude of annual oscillations. However, it seems that the annual oscillation is getting weaker, especially for subareas near the coast. For the entire BoB, the subsurface salinity shows an upward trend with a  $0.27\text{psu}$  increase (Figure 4.22j).

#### 4.2.4 Stratification

Figure 4.23 shows an overview of the long-term change of the projected stratification. The strength of stratification is measured by the buoyancy frequency determined by the vertical density gradient. The depth of maximum buoyancy frequency indicates the depth of the pycnocline. Under the high emissions pathway, the stratification strength is enhancing, and the pycnocline depth is getting shallower in most areas of the BoB. Although the stratification shows a long-

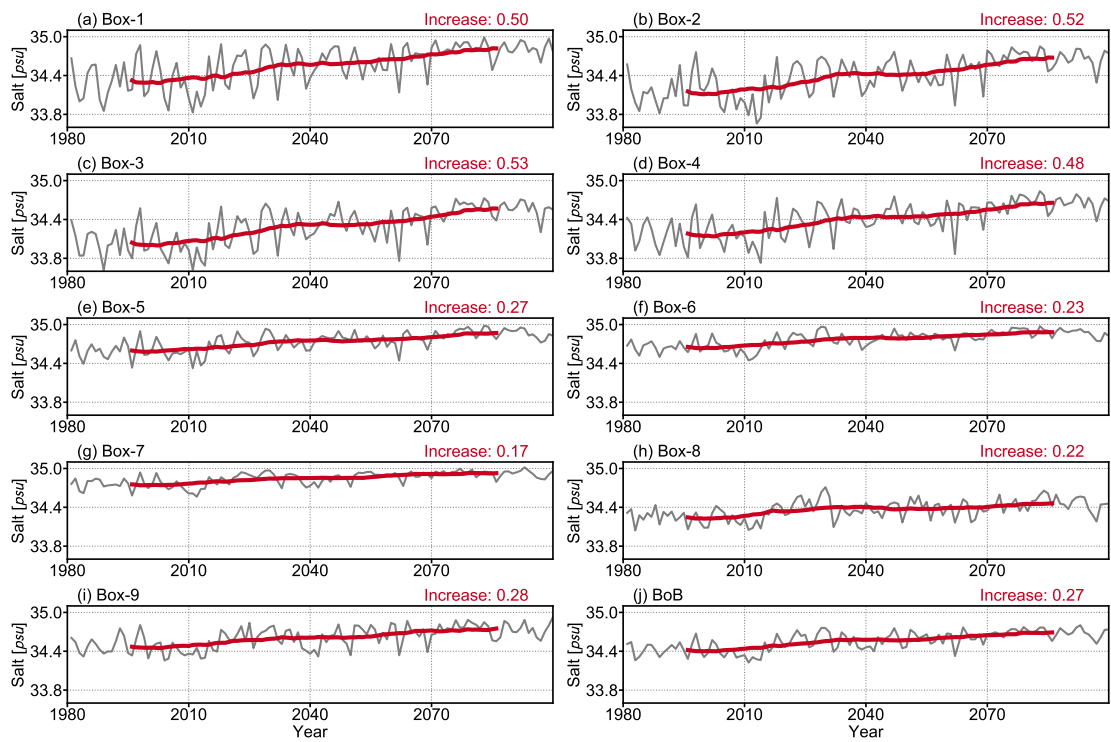


Figure 4.22: As in Figure 4.21, but for the subsurface salinity

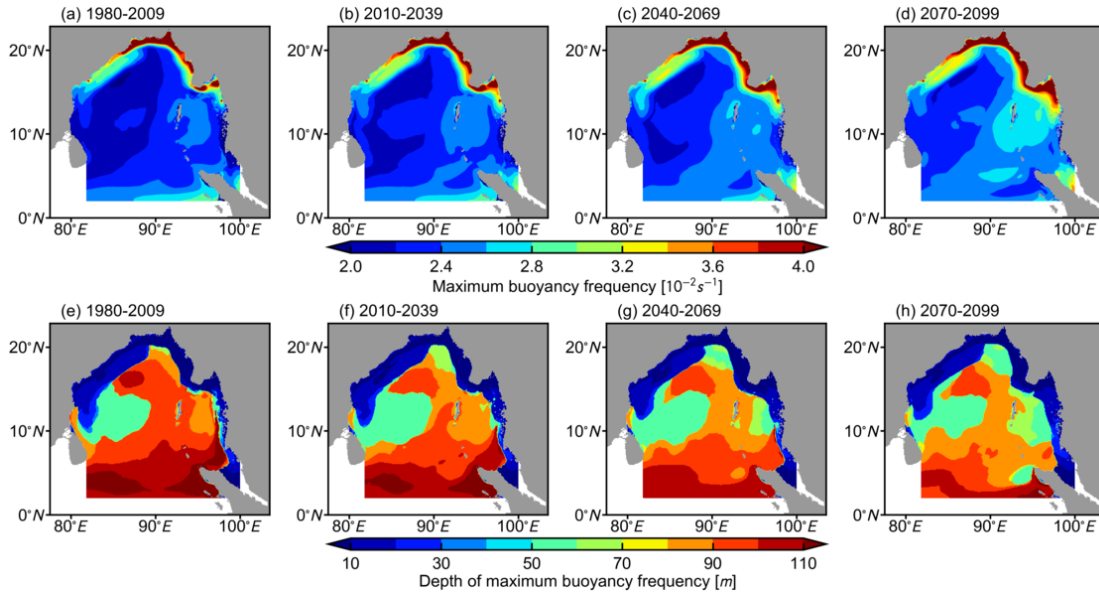


Figure 4.23: The distributions of maximum buoyancy frequency for the period 1980-2009 (a), 2010-2039 (b), 2040-2069 (c), and 2070-2099 (d), respectively. The distribution of depth of maximum buoyancy frequency for each period is shown in the second row.

term change, the overall spatial pattern is primarily the same throughout the entire simulation. The maximum stratification is located in relatively shallow depth and is strong at the northern and western boundaries. In contrast, in the eastern, central, and southern regions, the maximum stratification is located relatively deep and is weak. In the area closer to the equator, the pycnocline is located about in 100m depth. In contrast, the area close to the coast, especially the area near the northern boundary, is affected by abundant freshwater supplied by rivers, and hence, the pycnocline is located shallow in a depth of 20m. Overall, along the counterclockwise direction of the coast, the pycnocline depth changes from deep to shallow when going north, and then from shallow to deep when going south. The subarea located at the northern boundary shows the intensest stratification (Figure 4.24). Subareas in the south tend to have one pycnocline, while subareas in the north trend to have two. For example, Box-4 shows a primary pycnocline at a depth of 20m and a secondary pycnocline at a depth of about 60m, while Box-1 exhibits only one pycnocline at a depth of 100m.

For the long-term trend, the results show the temperature increase and the stratification intensification of the upper ocean (Figure 4.24). Usually, the depth of the pycnocline is relatively stable throughout the entire simulation, except for Box-2, where the depth of maximum buoyancy frequency shows an upward trend, rising to about 30m at the end of the 21st century, and at a depth of about 100m still a significant stratification exists.

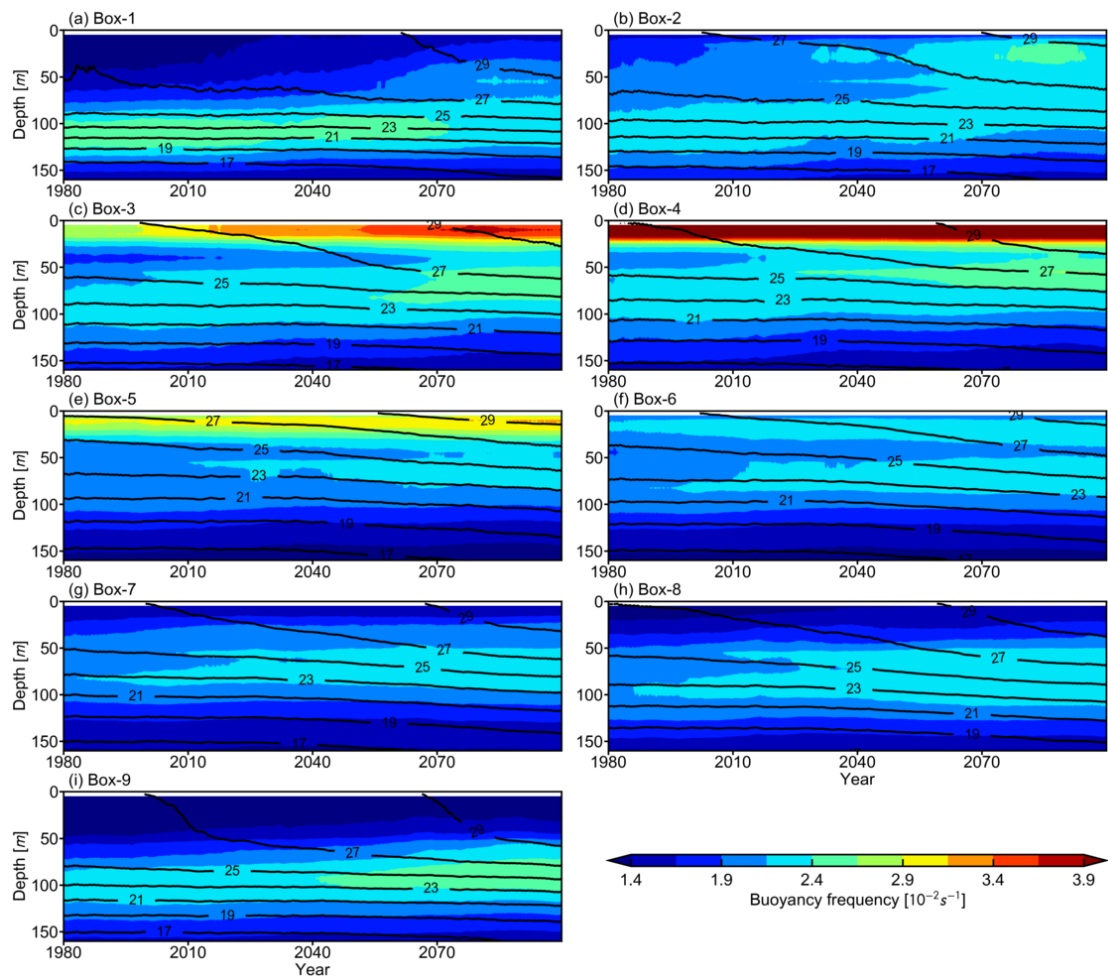


Figure 4.24: The depth-time diagrams of 30-year running mean of domain-averaged buoyancy frequency (shaded) and temperature (contours, in  $^{\circ}\text{C}$ ) for different subareas.

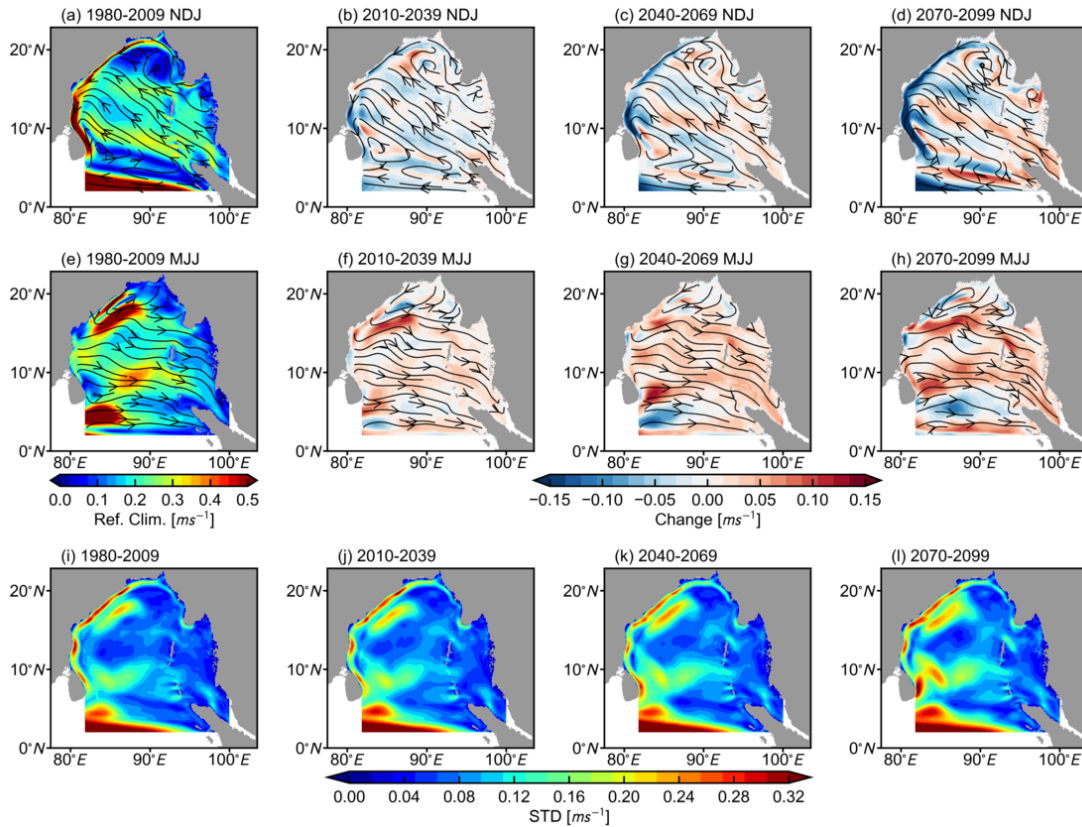


Figure 4.25: Climatological sea surface current speed in NDJ (a) for the period 1980-2009. Changes of current speed in NDJ compared to (a) are shown in (b) for 2010-2039, (c) for 2040-2069, and (d) for 2070-2099. The second row as in the first row, but for MJJ. Black lines with arrows are streamlines. The standard deviation of climatological monthly sea surface current speed for each period is shown in the third row.

#### 4.2.5 Circulation

Under the RCP8.5 scenario, the surface circulation of the BoB maintains its monsoon-controlled seasonal characteristics, but the strength changes (Figure 4.25). For example, in winter, the EICC in the last 30-year period is weaker than in the current climate state (Figure 4.25d). Besides, in the east of Sri Lanka, the seasonal variability of sea surface current speed shows a trend of enhancement (Figure 4.25i, j, k, l).

For the upper ocean circulation, the spatial pattern remains unchanged under the RCP8.5 scenario (Figures 4.26, 4.27). However, three flows are showing apparent long-term trends. First, the subsurface flow between  $5^{\circ}N$ - $7^{\circ}N$ , here the westward flow in summer is getting stronger, and its seasonal variability is also enhanced. Second, the western boundary current is getting weaker in winter, the depth of influence is becoming shallower, and its seasonal variability is also getting weaker. Third, the north-south flow from  $50m$  to  $200m$  at the eastern boundary is

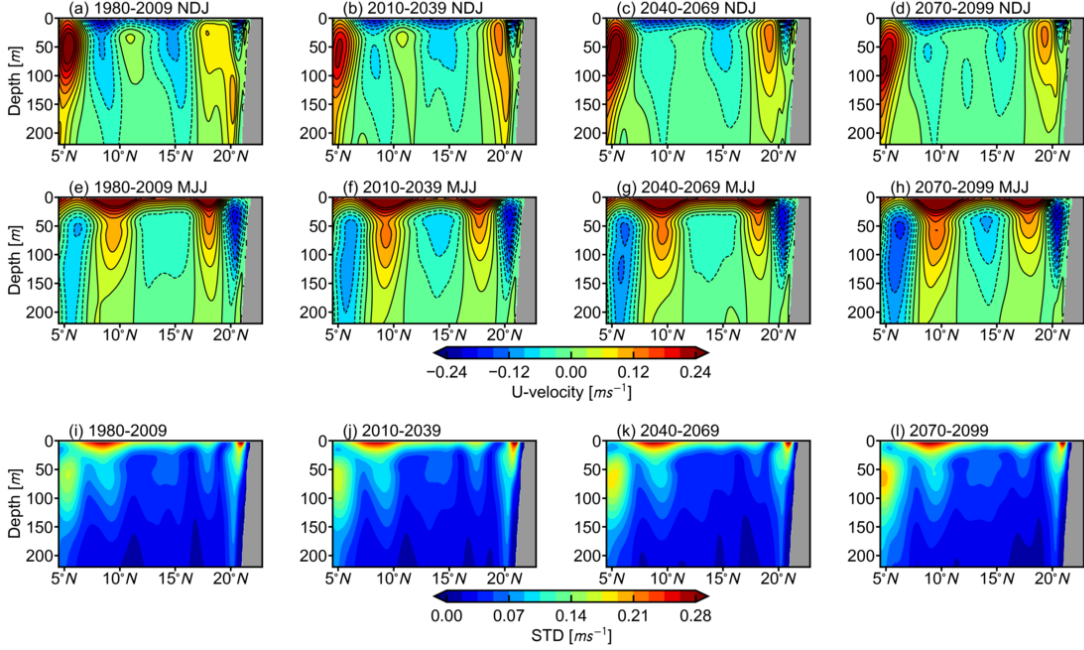


Figure 4.26: Climatological U-velocity (averaged over  $88^{\circ}E-90^{\circ}E$ ) in NDJ for the period 1980-2009 (a), 2010-2039 (b), 2040-2069 (c), and 2070-2099 (d), respectively. The second row as in the first row, but for MJJ. The standard deviation of climatological monthly U-velocity for each period is shown in the third row.

getting stronger, so as its seasonal variability.

The domain-averaged surface and subsurface current speeds for all subareas show large amplitudes of annual oscillations and small long-term trends (Figure 4.28, 4.29). The western boundary current shows a weakened long-term trend with large annual oscillations (Figure 4.28e, f, Figure 4.29e, f). The enhancement of the subsurface flow at the eastern boundary is confirmed by Figure 4.29b. The current speed in the east of Sri Lanka shows a strengthening trend at the surface (Figure 4.29g) but keeps stable in the subsurface (Figure 4.29g).

#### 4.2.6 Coastal Kelvin Wave

As discussed in the previous section, the external signal such as IOD modulates the interannual subsurface variability through its trigger effect on coastal Kelvin waves (CKWs) and Rossby waves. These large scale waves play an important role for the ocean dynamics, especially for the BoB, which is bounded in the north. In this subsection, the long-term change of intraseasonal coastal Kelvin waves under the RCP8.5 scenario is discussed based on the daily temperature from the HAMSOM experiment RCP85 and the latest methodology to extract the wave information.

Rydbeck et al. (2019) developed a methodology to objectively determine amplitude and phase information of equatorial Kelvin waves on the basis of sea surface height anomalies in the Pacific. This method is analogous to methods utilized for the study of atmospheric intraseasonal

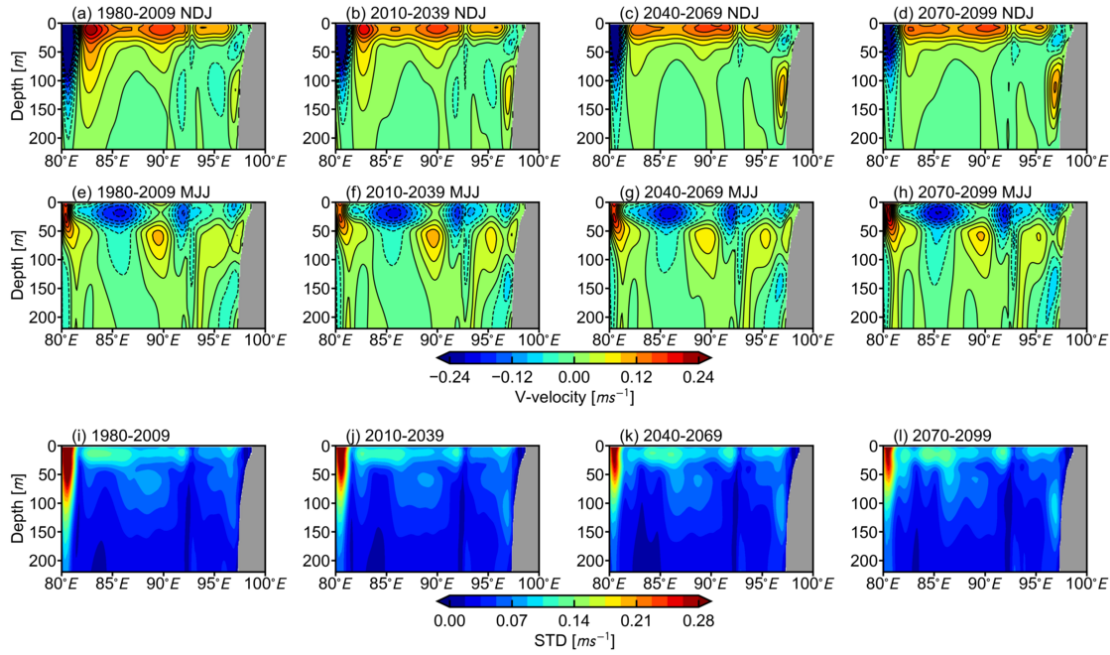


Figure 4.27: As shown in Figure 4.26, but for the V-velocity averaged over  $10^{\circ}N$ - $12^{\circ}N$ .

variabilities. Therefore, this method is also supposed to be appropriate to analyze CKWs as well as other intraseasonal wave-type variations.

Figure 4.30 shows two waveguides at the  $100m$  (D100) and  $20m$  (D20) depth isobath along the coast. The waveguides start at the west coast of Sumatra and run counterclockwise to the east coast of Sri Lanka. The lengths of D100 and D20 are about  $5900km$  and  $7900km$ , respectively. In the northern hemisphere, the CKWs are limited to propagate counterclockwise, so the counterclockwise is defined as the positive direction of these waveguides. Thus, the CKWs are limited to positive wavenumber signals along the waveguides.

To determine the information of internal CKWs along the BoB coasts, the daily anomalies of the one-year running mean of temperature along the waveguide are analyzed. Before applying the filter process described by Rydbeck et al. (2019), the temperature anomalies along the waveguide were linearly interpolated to achieve an equidistant distribution in space. The filter process is as follow. First, the first three harmonics of the seasonal cycle are removed by linear regression. Next, the clockwise moving waves are eliminated by two dimensional Fast Fourier Transform. Finally, the anomalies are band-pass filtered using a 30-180-day Lanczos filter to isolate the time scale of concern.

Figure 4.31 shows the unfiltered and filtered temperature anomalies at D100. The unfiltered temperature anomalies show a semiannual feature, reflecting two pairs of upwelling and downwelling Kelvin waves from the equator (Rao and Sivakumar, 2000; Hase et al., 2008; Rao et al., 2010; Sreenivas et al., 2012). Noteworthy, the intraseasonal CKWs are unrecognizable in the unfiltered field. After the filtering, the results show intraseasonal signals propagating counter-

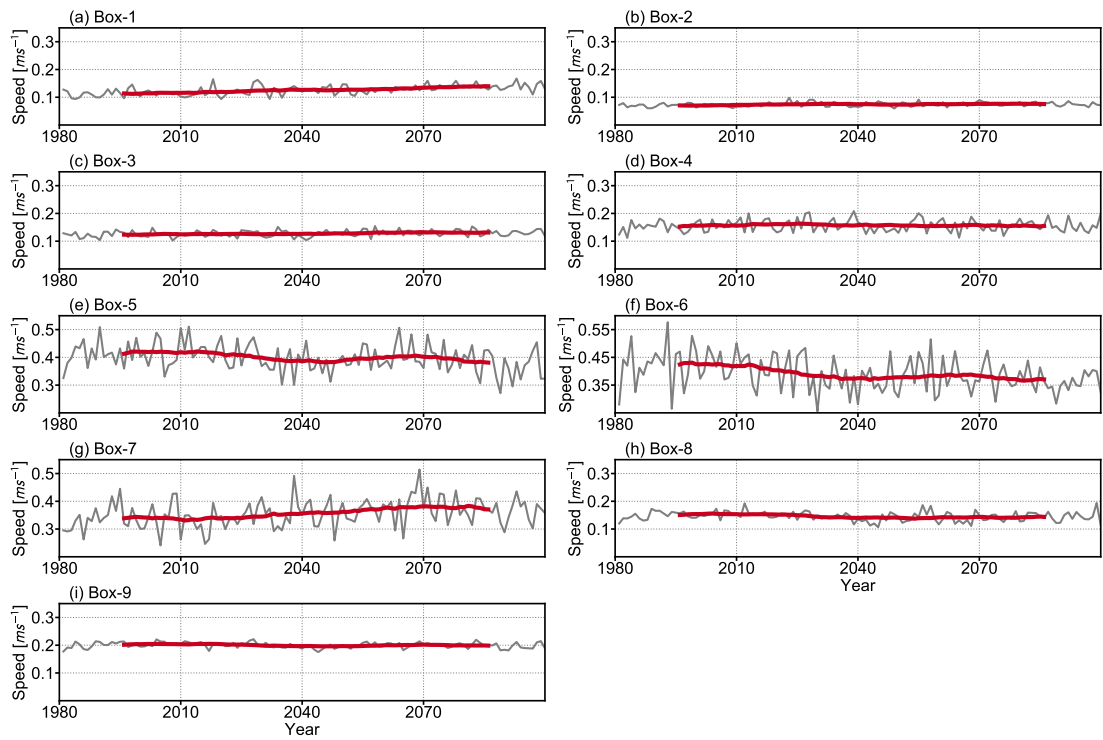


Figure 4.28: Yearly time series (grey line) and 30-year running mean (red line) of domain-averaged upper-50m-averaged current speed for subareas.

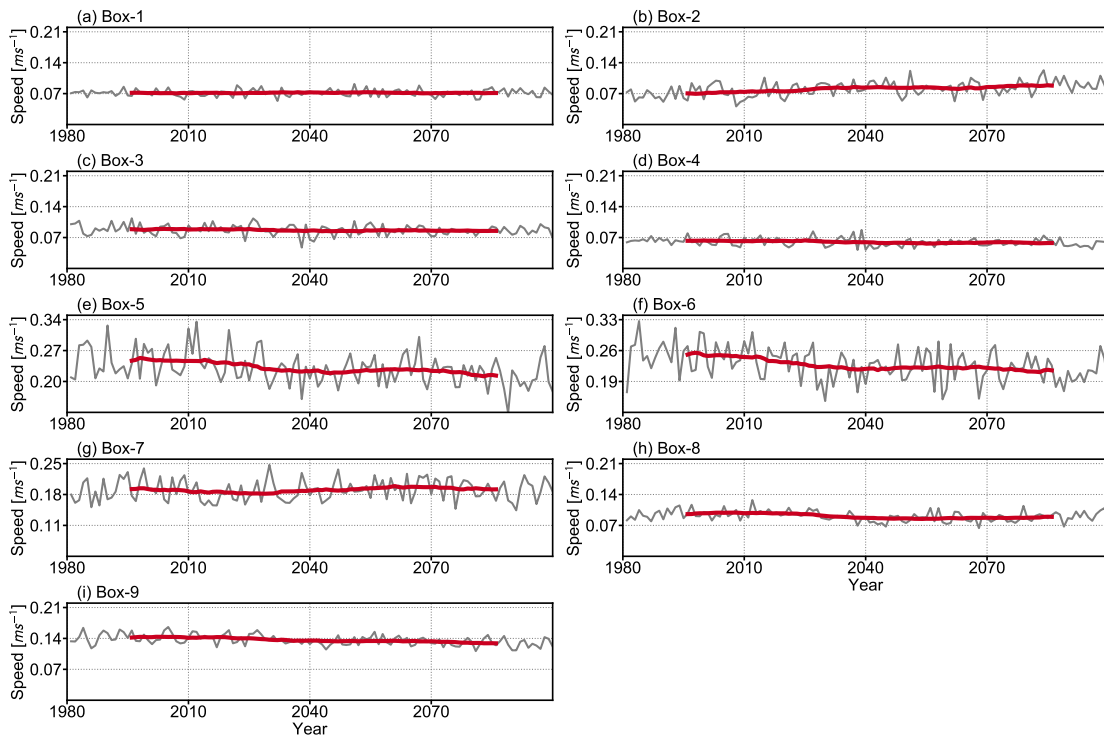


Figure 4.29: As in Figure 4.28, but for the current speed at 100m.

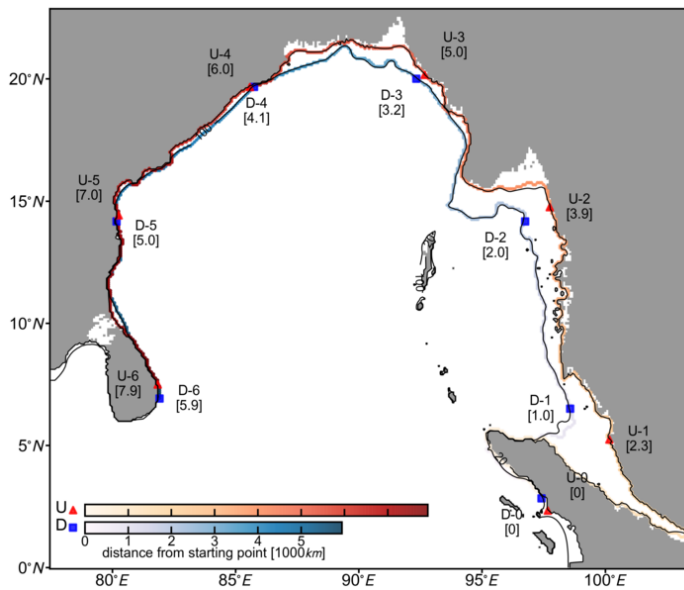


Figure 4.30: Waveguides at 20m (D20) and 100m (D100) depth along the shore. Locations are marked (red triangle for 20m; blue square for 100m) to indicate their distance from the starting point along the waveguide. The distance is labelled in brackets.

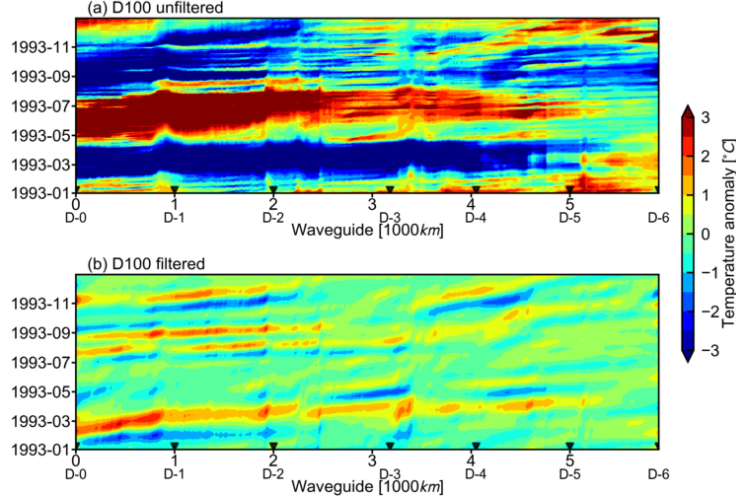


Figure 4.31: Waveguide-time diagrams of unfiltered temperature anomalies (a) and filtered temperature anomalies (b) at D100.

clockwise along the waveguide, indicating the existence of intraseasonal CKWs. The unfiltered and filtered temperature anomalies at D20 are shown in Figure 4.32. For this waveguide at a depth of 20m, the intraseasonal signals also appear in the filtered field, but mainly concentrate at the second half of the waveguide from U-3 to U-6. Due to the distribution of background pycnocline depth (Figure 4.23), the segment from D-0 to D-3 (D100-seg) of D100 and the segment from U-3 to U-6 (D20-seg) of D20 are discussed separately in following.

The filtered anomalies are used to perform an Empirical Orthogonal Function (EOF) analysis. The EOF results are shown in Figure 4.33. The leading two PCs of D100-seg and D20-seg explain about 66% and 51% variance. The lag Pearson correlation between PC1 and PC2 shows a phase difference about 15 days with a correlation of over 0.6. The power spectrums of PC1 and PC2 for D100-seg show two peaks near 70 and 90 days, while the results of D20-seg show a primary peak at 90 days and two secondary peaks at 60 and 70 days, indicating different internal CKW characteristics.

Figure 4.34 shows the first two EOF modes for D100-seg and D20-seg. If the filtered anomalies are purely the representatives of a moving sine wave, then the first EOF mode should explain the same variance as the second mode, and their curves should be smooth and show a shift with half a wavelength. The curves here are relatively unsmooth, but the expected shift between two modes is recognizable.

The wave amplitude and phase can be determined from the first two leading principal components (PCs) using the following formulas:

$$Amp(t) = \sqrt{(PC1(t)^2 + PC2(t)^2)} \quad (4.2)$$

$$Pha(t) = \arctan\left(\frac{PC2(t)}{PC1(t)}\right) \quad (4.3)$$

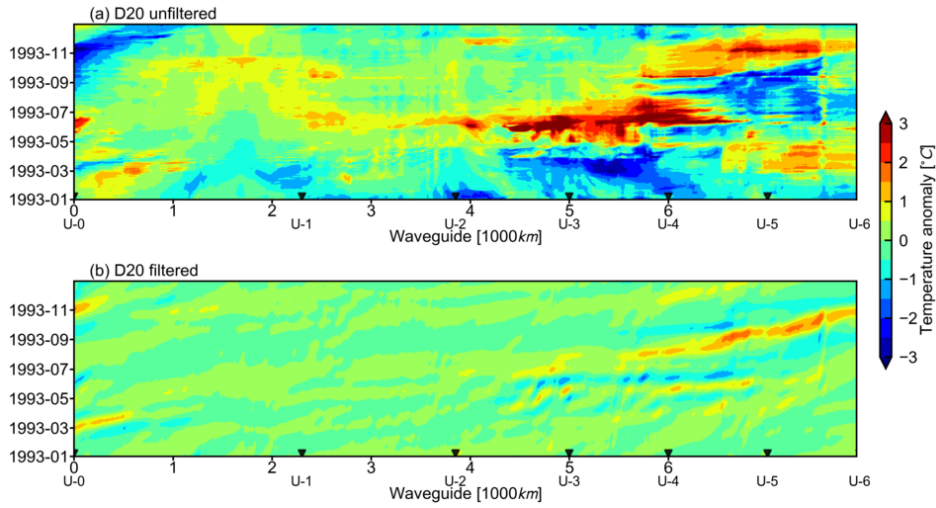


Figure 4.32: As in Figure 4.31, but for D20.

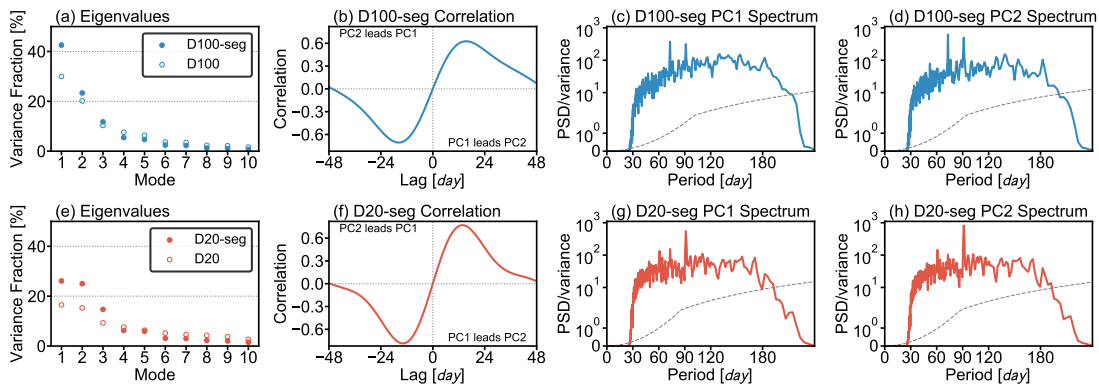


Figure 4.33: The variance fraction of the first ten EOFs at D100-seg (from D-0 to D-3) and D100 (a), the lag Pearson correlation of the first two PCs at D100-seg (b), the power spectrum of PC1 (c) and PC2 (d) for D100-seg, dashed line shows the 99% significant level. The second row as in the first row, but for D20-seg (from U-3 to U-6).

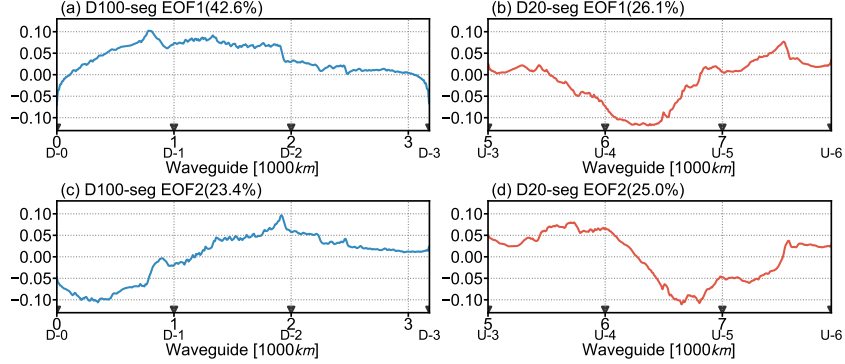


Figure 4.34: The first and second EOF mode for D100-seg (a, c) and D20-seg (b, d).

The amplitude, which is also defined as the intraseasonal Kelvin wave index (KWI; Rydbeck et al., 2019), represents the averaged strength of the CKW associated oscillations over the analyzed area. The period of each wave can be estimated from their calculated phases.

Figure 4.35 shows the time series of the KWI of D100-seg and D20-seg and their probability distributions. These distributions show a good agreement with the exponentiated Weibull distribution and skew to the left. Due to the definition of KWI, the strength of KWI indicates the averaged strength of anomalies over the analyzed waveguide, which makes it possible to detect significant cases of CKWs. To determine the significant CKWs, the 90% value of the fitted distribution probability density function is defined as the threshold value. The threshold value is 14.15 for D100-seg and 8.30 for D20-seg, respectively.

The CKW associated temperature anomalies can be reconstructed by the reconstruction of EOFs as follows:

$$Tempa_{Kelvin\ waves} = EOF1 \times PC1 + EOF2 \times PC2 \quad (4.4)$$

Figure 4.36 shows the reconstructed temperature anomalies and marks the significant CKWs detected from the KWI. The internal CKWs at D100-seg travel faster than that at D20-seg. The magnitudes of the estimated phase speed reasonably agree with estimates of internal gravity wave speeds calculated on the basis of the shallow water equation applying average values for the local upper layer thickness and the local reduced gravity. The reconstructed fields are expected to represent the deviation from the average state, therefore their probability distributions should match well with the Student's t-distribution as shown in Figure 4.37. The results indicate that associated oscillations of the CKWs at D100-seg are more significant than at D20-seg. Similar to the selection of the 90% threshold value for KWI, 5% and 95% values are defined as symmetric threshold values for negative and positive significant anomalies. Using this definition, temperature changes that represent significant CKWs must exceed 0.44 °C at D20-seg and 0.73 °C at D100-seg.

The occurrence of all detected significant CKWs at D100-seg and D20-seg from 1980 to 2099 is shown in Figure 4.38. A total of 228 and 182 significant CKWs are formed at D100-seg and D20-seg, respectively. The accumulated occurrence for each month indicates that significant CKWs at D20-seg usually occur from April to November and are mainly concentrated between May to

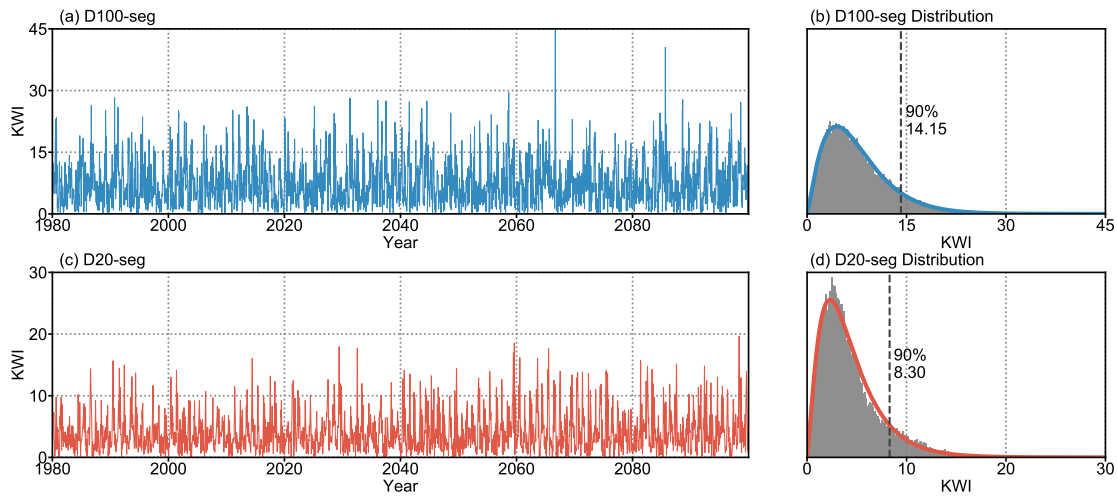


Figure 4.35: The KWI time series of D100-seg (a), the distribution of (a) is shown in (b), Thick solid line shows the fitted probability density function of the exponentiated Weibull distribution, black dashed line indicates the threshold of the 90% KWI. The second row as in the first row, but for D20-seg.

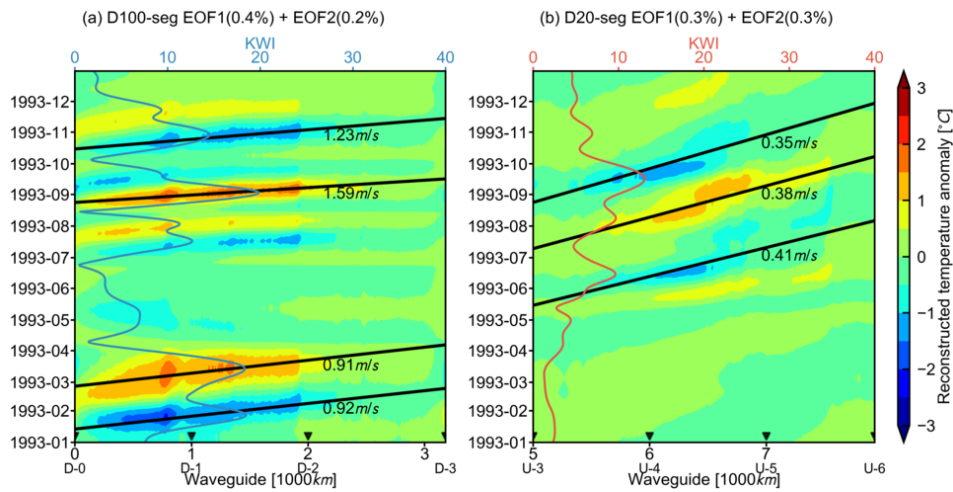


Figure 4.36: The reconstructed temperature anomalies of the first two EOFs of D100-seg (a) and D20-seg (b), blue line and red line show the KWI for D100-seg and D20-seg, respectively. Black lines indicate the significant CKW cases, corresponding speeds estimated by the weighted linear regression are labelled.

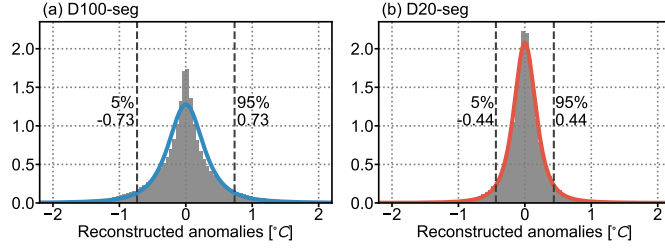


Figure 4.37: The distribution of the reconstructed temperature anomalies of D100-seg, blue solid line shows the fitted probability density function of the Student's t-distribution, black dashed lines indicates the threshold of the 5% and the 95% data. (b) as in (a), but for D20-seg.

July, while significant CKWs at D100-seg occur throughout the year and show two peak periods around March and August (Figure 4.38b). The accumulated occurrence for each year shows that there may occur only one or even no waves in some years, while in other years, possibly up to 7 significant CKWs are generated at D100-seg and 4 at D20-seg (Figure 4.38c). For the long-term trend, the occurrence of significant CKWs at D20-seg will become more frequent (Figure 4.38d). The same holds true for D100-seg for the first three 30-year periods, but for the last 30-year period a decreasing number of significant CKWs is observed.

The phase speed of each significant CKW can be estimated on the basis of the significant temperature anomalies of the reconstructed fields by applying a weighted linear regression in the space-time domain. The wave period is determined by the time series of the phases. Based on the dispersion relationship of the Kelvin wave  $w = ck$ , where  $w$  is the frequency,  $c$  is the phase speed, and  $k$  is the wavenumber, the distribution of significant CKWs in the wavelength-period domain is shown in Figure 4.39. The results reveal the difference in wave characteristics between significant CKWs at D100-seg and D20-seg. Significant CKWs at D100-seg usually have a longer wavelength than that at D20-seg, while their periods exhibit about the same range, indicating that significant CKWs at D100-seg generally travel faster. The wavelength of significant CKWs at D20-seg is relatively stable, while the period is distributed between 20 to 60 days, resulting in the fact that significant CKWs at D20-seg are generally getting slower when their period is becoming longer.

There are two variables that have a decisive influence on the characteristics of internal CKWs along the BoB; one is the local wind, and the other is the incoming Kelvin wave signal from the equator. To focus on long-term changes, the daily KWI is monthly averaged and discussed together with the above mentioned monthly averaged data. Figure 4.40 shows the results of the monthly KWI of D100-seg and the corresponding local wind stresses and speed. Since the D100-seg is located at the eastern boundary, the domain-averaged wind variables in the Box-2 are selected to represent the local wind. The KWI at D100-seg only shows a slight upward trend with oscillations of approximately 10 years (Figure 4.40a). However, it shows remarkable changes over time on the monthly climatological scale (Figure 4.40b-e). For the first two 30-year periods, two comparable peaks in the monthly climatological KWI around March and September occur. In contrast, it exhibits only one significant peak around August for the last two 30-year

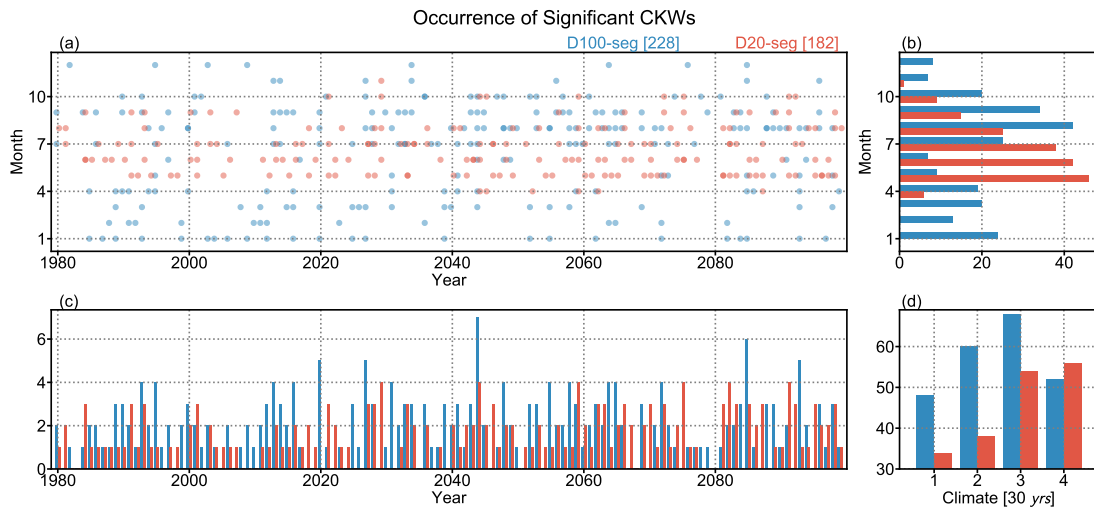


Figure 4.38: The temporal distribution (a) of significant CKWs for D100-seg (blue) and D20-seg (red), the total number of significant CKWs is labelled in brackets, (b) shows the accumulated occurrence for each month, (c) shows the accumulated occurrence for each year, (d) shows the accumulated occurrence for each 30-year.

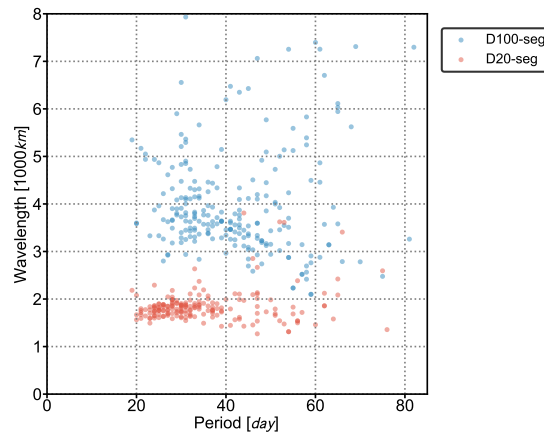


Figure 4.39: The distribution of significant CKWs in the wavelength-period domain.

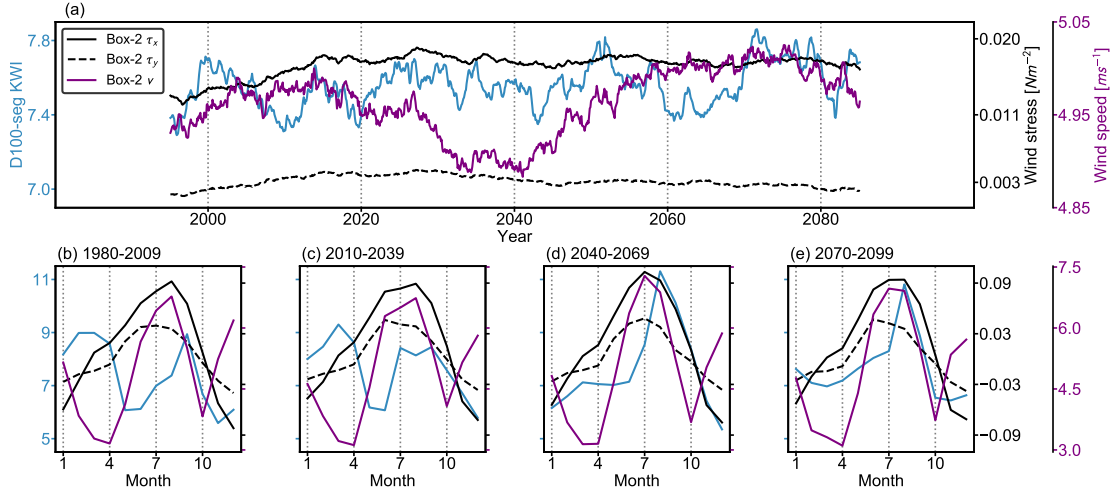


Figure 4.40: The (a) 30-year running mean of KWI of D100-seg (blue solid line), and domain-averaged zonal (black solid line), meridional (black dashed line) wind stress and wind speed (purple solid line) of Box-2. (b-e) shows the climatological monthly variability for each 30-year.

periods. This result suggests that the monthly variability of internal CKWs at the BoB eastern boundary will significantly change in the second half of the 21st century under the high emissions pathway. The monthly climatology of the local wind is relatively stable, and it peaks around August, indicating that the KWI at D100-seg is significantly affected by the local wind in the last two 30-year.

The KWI at D20-seg shows a significant upward trend and the occurrence of a jump around the year 2040 (Figure 4.41). The local wind speed shows a high accordance with the KWI on the climatological scale, also showing a similar jump at around 2040, demonstrating that the KWI at D20-seg is influenced by the wind field, especially by the wind strength. The wind stress in the zonal and meridional directions also exhibits a long-term upward trend, indicating that the southwest monsoon is enhancing. The monthly climatologies show that the KWI at D20-seg is getting stronger around May and June (Figure 4.41b-e), but they do not show changes in the number of peaks. Results of the local wind stress also show a positive peak in summer, indicating that at the BoB western boundary the significant internal CKWs are excited during the southwest monsoon season. This agrees with the analysis presented in Figure 4.38b. The pycnocline depth is shallow at the BoB western boundary, making the pycnocline more susceptible to the local wind. Therefore, with respect to the long-term trend, unlike the internal CKWs at the eastern boundary, the internal CKWs at the western boundary always exhibit a high correlation with the local wind.

Besides the local wind, the intraseasonal variability of the thermocline in the eastern equatorial Indian Ocean is expected to influence the internal CKWs in the BoB. The 2-7-month band-pass-filtered temperature anomalies averaged from  $95^{\circ}E$ - $100^{\circ}E$  and  $80m$ - $120m$  at the equator is employed as a proxy for the external intraseasonal variability from the equator. The 30-year running Pearson correlation between the monthly KWI and the filtered temperature anomalies,

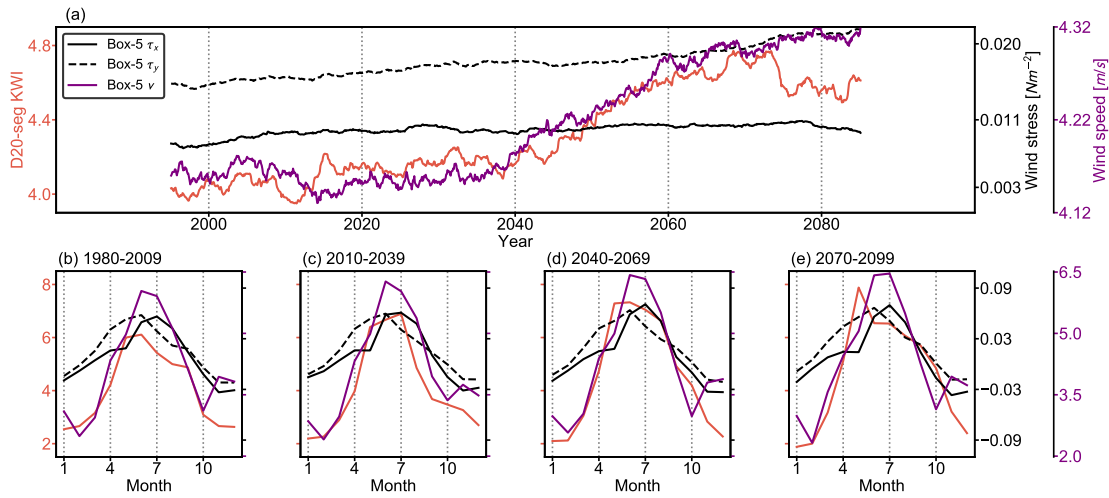


Figure 4.41: As in Figure 4.40, but for D20-seg (red solid line) and Box-5.

as well as between the monthly KWI and the local wind variables, is shown in Figure 4.42. For D100-seg (Figure 4.42a), the correlation between the KWI and the equatorial intraseasonal variability shows a downward trend, while the correlation with the local wind shows an upward trend, indicating that, along the BoB eastern boundary, the intraseasonal variability from the equator is losing influence on the internal CKWs and the local wind is gaining influence. Although the depth discussed here is 100m, as previously analyzed, the stratification will become stronger and shallower in the future, which may explain why the influence from local winds will become more significant. On the other hand, the model results imply that the impact of the equatorial ocean information in affecting the BoB conditions is getting smaller under the high emissions pathway. This in turn will affect the characteristics of further variables in the BoB that could become significantly different from the current climate state, as well in their mean as in their variability.

For D20-seg (Figure 4.42b), the KWI is maintaining its high correlation with the local wind and the relatively low correlation with the equatorial intraseasonal variability during the entire scenario forecast period. The weak negative correlation between the KWI and the equatorial intraseasonal variability indicates that the internal CKWs at the BoB western boundary have a significantly different source compared to the internal CKWs at the eastern boundary. However, this analysis does not imply that the internal CKWs cannot propagate from the eastern boundary to the western boundary, but indicates that the characteristics of internal CKWs at the western boundary are affected mostly by the local wind, as the shallow location of the pycnocline in this area would suggest.

### 4.3 Climate Change and Natural Variability

As discussed in the previous section, compared to the current climate state, the downscaled simulation under the RCP8.5 scenario indicates a warming tendency of the upper BoB, as well

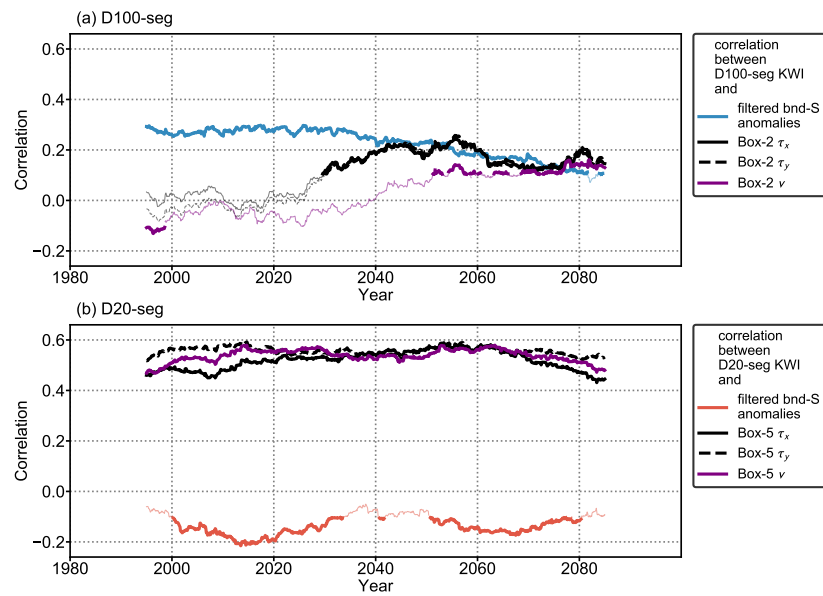


Figure 4.42: The 30-year running Pearson correlation between the monthly KWI of D100-seg and the 2-7-month band-pass-filtered temperature anomalies averaged from  $95^\circ E$ - $100^\circ E$  and  $80m$ - $120m$ , the domain-averaged (Box-2) zonal wind stress, meridional wind stress, and wind speed (a), correlation coefficients with  $p$ -value  $\geq 0.05$  are indicated by thin lines. (b) as in (a), but for D20-seg and Box-5.

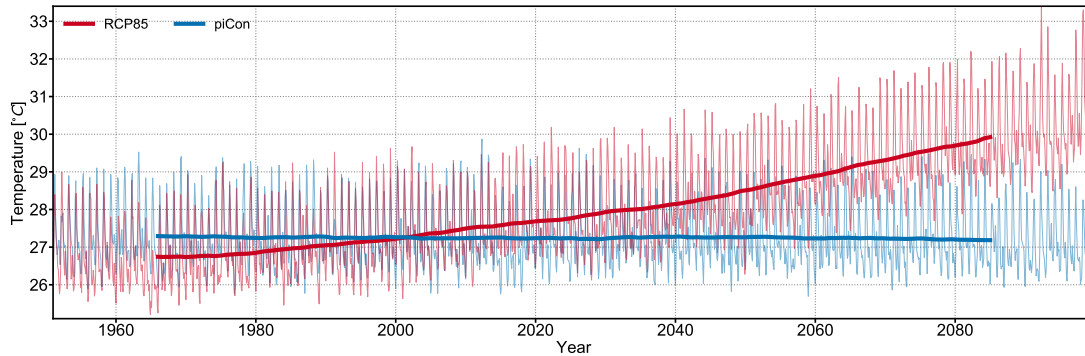


Figure 4.43: Monthly time series (thin lines) and 30-year running mean (thick lines) of domain-averaged sea surface temperature in the BoB from the experiment RCP85 (red) and piCon (blue), respectively.

as other long-term changes. However, the actual contribution of anthropogenic factors to these climate variabilities cannot directly be detected. Uncertainty in climate projections arises from three main sources: model forcing, model response, and internal model variability (Hawkins and Sutton, 2009; Deser et al., 2012). The internal variability refers to the intrinsic variability of the climate system that occurs in the absence of external forcing, and hence is also called ‘natural variability’ (Swanson et al., 2009; Hawkins, 2011; Deser et al., 2012). In this section, in addition to the primary experiment RCP85, the experiment piCon driven by the global forcing under the pre-industrial scenario is also analyzed. The experiment piCon represents the case without the influence of industrial activities, and therefore it describes the simulated climate system’s natural variability. Meanwhile, it can be assumed that the uncertainties involved in the two experiments are equivalent, since the same numerical configurations are used. Therefore, by comparing the results from these two experiments, the anthropogenic induced climate variabilities can be assessed.

Figure 4.43 shows the monthly time series and 30-year running mean of the BoB domain-averaged sea surface temperature for the two experiments. The sea surface warming tendency under the RCP8.5 scenario is clear. In contrast, under the pre-industrial scenario, the sea surface temperature keeps stable. This comparison indeed suggests that, on the climatological scale, the predicted sea surface warming in the BoB is mainly caused by industrial activities rather than by the inherent climate variabilities.

To further investigate the evolution of sea surface temperature in the BoB, a wavelet analysis (Meyers et al., 1993; Torrence and Compo, 1998; Torrence and Webster, 1999; Grinsted et al., 2004) is applied for these two experiments (Figure 4.44 and Figure 4.45). For the experiment RCP85, the monthly time series is first detrended by removing the long-term trend (Figure 4.44a). The wavelet power spectrum and the global wavelet spectrum indicate that the primary variabilities of the detrended time series are concentrated in the semiannual and the annual frequency band, reflecting the seasonality of the BoB. The scale-averaged power within the band from six months to one year shows an upward trend, which indicates the semiannual and annual

variabilities are strengthening with time under the RCP8.5 scenario.

The corresponding wavelet analysis for the experiment piCon also emphasizes the existence of variabilities in the semiannual and the annual frequency band (Figure 4.45). The wavelet analysis indeed suggests that the semiannual and annual fluctuations are inherent variabilities of the BoB sea surface temperature. However, the scale-averaged power of the experiment piCon does not show an upward trend (Figure 4.45a), with a value which is generally smaller than for the experiment RCP85 especially for the second half of the 21st century, indicating that industrial activities are responsible for a predicted enhancement of the seasonal variability of BoB sea surface temperature.

The sea surface warming and the enhancement of the seasonal variability is shown in Figure 4.46. Because the forcing is bias-corrected on the basis of the realistic current climate state, the seasonal cycle and its magnitude in the piCon run show a good agreement with the results of RCP85 during the period 1980-2009. However, the gap between these two experiments is getting larger in the following three 30-year periods (Figure 4.46a-d). The annual cycle in the piCon run stays constant showing a standard deviation in the range of  $0.73$  to  $0.77^{\circ}C$ . From these standard deviations, it can be estimated that the uncertainty of natural seasonal variability of sea surface temperature in the BoB is approximately  $0.04^{\circ}C$ . In contrast, the annual cycle of the RCP85 run shows an increasing standard deviation from  $0.80$  to  $0.96^{\circ}C$ . The change in standard deviation is  $0.16^{\circ}C$ , which is significantly larger than the estimated uncertainty of  $0.04^{\circ}C$ , indicating that industrial activities significantly cause an enhancement of the sea surface temperature seasonal variability under the RCP8.5 scenario. The standard deviation of each month is shown in the second row of Figure 4.46. For piCon, these standard deviations do not show a significant change with time. In contrast, for RCP85, the standard deviations are larger during the last two periods than during the first two periods. The change in the standard deviation for RCP85 is  $0.03^{\circ}C$  from the period 1980-2009 to 2010-2039 and  $0.07^{\circ}C$  from the period 2010-2039 to 2040-2069. It can be inferred that extreme sea surface temperature changes are becoming much more frequent at some point in the middle of the 21st century.

For the subsurface at a depth of  $100m$ , warming mainly occurs in summer (Figure 4.47). The natural seasonal variability of subsurface temperature shows two peaks in summer and winter, respectively. Under the RCP8.5 scenario, the peak in summer increases significantly. The standard deviation of the climatological annual cycle of piCon is in a range between  $0.25$  to  $0.32^{\circ}C$ . In contrast, the range for RCP85 increases from  $0.23^{\circ}C$  in the period 1980-2009 to  $0.45^{\circ}C$  in the period 2070-2099. The uncertainty of BoB subsurface temperature induced by the natural seasonal variability is  $0.07^{\circ}C$ , which is smaller than the change of  $0.22^{\circ}C$  under the RCP8.5 scenario, indicating the dominant role of the industrial activities. The standard deviation shows a sudden change from  $0.26^{\circ}C$  in 2010-2039 to  $0.44^{\circ}C$  in 2040-2069, implying the existence of a climate transition point in the middle of the 21st century.

The enhancement of seasonal variability under the RCP8.5 scenario can also be observed in the sea surface salinity field (Figure 4.48). The standard deviation of the climatological annual cycle of the piCon run is in a range between  $0.26$  to  $0.27psu$ , indicating that the annual cycle is stable in the absence of external forcing. In contrast, under the RCP8.5 scenario, the surface seawater will become saltier in summer and fresher in winter. The standard deviation of the climatological annual cycle of the RCP85 run is from  $0.29psu$  for the current climate state to

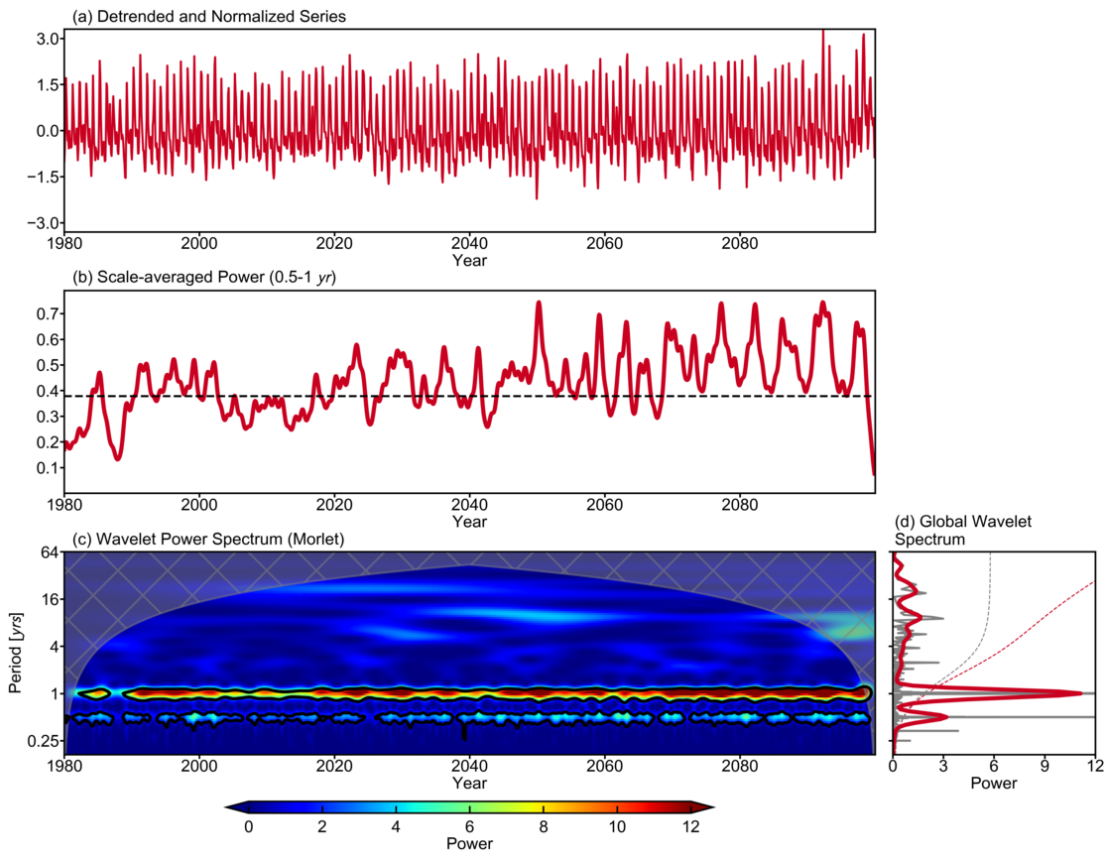


Figure 4.44: The detrended and normalized monthly time series of domain-averaged sea surface temperature in the BoB for the experiment RCP85 (a). (c) shows the wavelet power spectrum of time series in (a), black contours indicate the 95% Chi-squared confidence level, the cone of influence is hatched. (b) shows the scale-averaged power of the 0.5-1 year period, black dashed line indicates the 95% confidence level. (d) shows the global wavelet spectrum (red solid line), red dashed line indicates the 95% confidence level for the global wavelet spectrum, grey solid line indicates the normalized fast Fourier transform, grey dashed line indicates the 95% confidence level for the normalized fast Fourier transform.

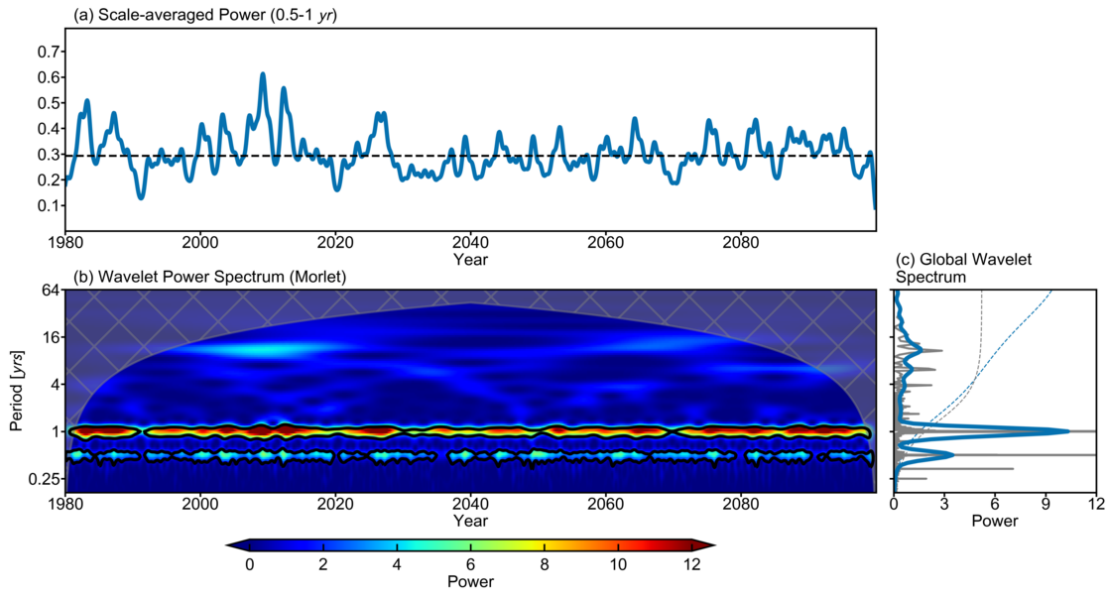


Figure 4.45: The wavelet power spectrum of normalized monthly domain-averaged sea surface temperature in the BoB for the experiment piCon (b), black contours indicate the 95% Chi-squared confidence level, the cone of influence is hatched. (a) shows the scale-averaged power of the 0.5-1 year period, black dashed line indicates the 95% confidence level. (c) shows the global wavelet spectrum (blue solid line), blue dashed line indicates the 95% confidence level for the global wavelet spectrum, grey solid line indicates the normalized fast Fourier transform, grey dashed line indicates the 95% confidence level for the normalized fast Fourier transform.

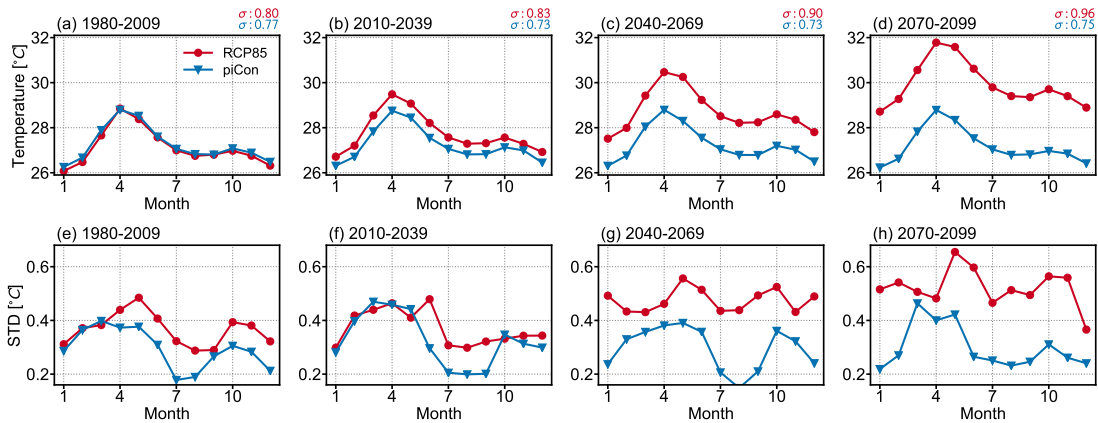


Figure 4.46: Climatological monthly variability of domain-averaged sea surface temperature from the experiment RCP85 (red) and piCon (blue) for the period 1980-2009 (a), 2010-2039 (b), 2040-2069 (c), and 2070-2099 (d), respectively, the standard deviation  $\sigma$  of climatological monthly variability is labelled with the corresponding color. The second row shows the standard deviation of each month for each period.

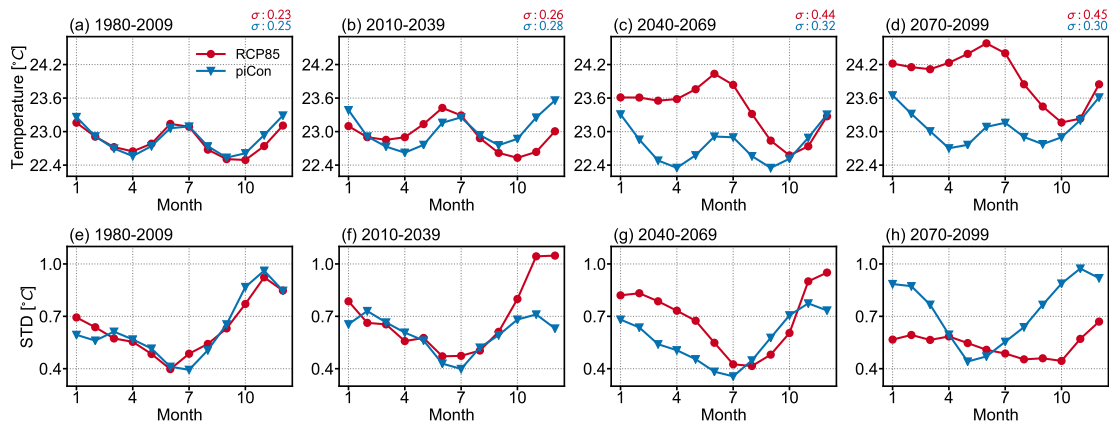


Figure 4.47: As in Figure 4.46, but for the subsurface temperature.

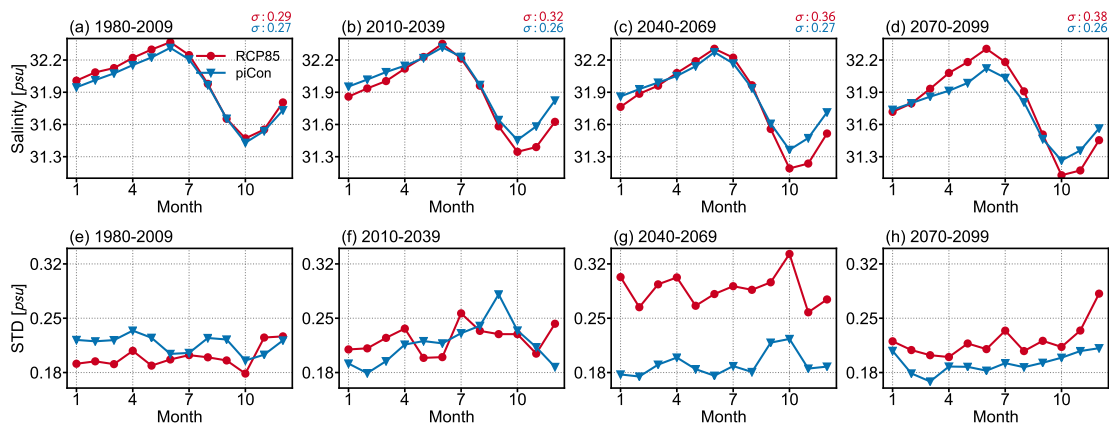


Figure 4.48: As in Figure 4.46, but for the sea surface salinity.

0.38 $psu$  for the last 30-year period, indicating a significant increase of seasonality caused by industrial activities. The standard deviations for each month also show a sudden change in the period 2040-2069 (Figure 4.48g) and a return to the previous level in the last 30-year period (Figure 4.48h), implying a climate transition point in the middle of the 21st century that has also been inferred from the temperature evolution.

For the subsurface salinity, the seasonality is relatively weak but still shows an anthropogenic influence (Figure 4.49). The uncertainty of natural variability suggested by the experiment piCon is 0.01 $psu$ . Under the RCP8.5 scenario, the standard deviation of the climatological annual cycle is 0.07 $psu$  in the fourth 30-year period, which is an increase of 0.04 $psu$  compared to the current climate state. Considering the uncertainty of natural variability, the change of 0.04 $psu$  is significant. The subsurface seawater shows a tendency to become saltier under the RCP8.5 scenario. However, salinity keeps almost unchanged under the pre-industrial scenario, demonstrating that the subsurface tendency to saltier conditions is also a consequence of industrial activities.

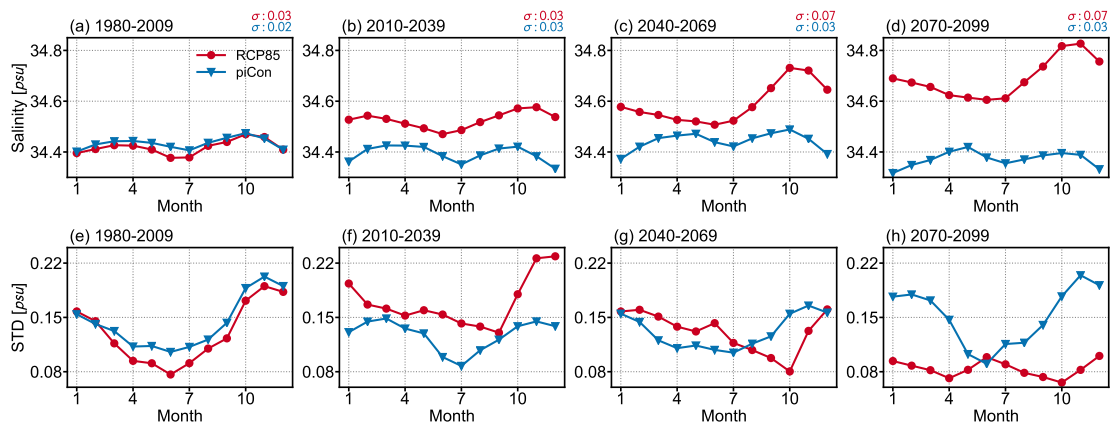


Figure 4.49: As in Figure 4.46, but for the subsurface salinity.

## Chapter 5

# Summary and Conclusions

The oceanic responses of the Bay of Bengal (BoB) under a global climate change scenario were investigated by means of a dynamic downscaling approach. The Hamburg Shelf Ocean Model (HAMSOM) was used to perform this downscaling study from 1951 to 2099, driven by an Earth System Model developed at the Max-Planck-Institute for Meteorology (MPI-ESM) that has been used in the context of the Coupled Models Intercomparison Project Phase 5 (CMIP5) process. To investigate the future ocean state and related processes of this bay under a high emissions pathway, the primary HAMSOM experiment was run with the historical scenario from 1951-2005 and the RCP8.5 scenario from 2006 to 2099. A supplementary HAMSOM experiment under the pre-industrial control conditions was also performed to distinguish the climate change signal from natural variability. In order to correct the systematic error in the open boundary forcing and to improve the downscaling result, a bias correction was applied.

The performance of HAMSOM was evaluated in terms of sea level anomaly, temperature, salinity, heat fluxes, and flow field. HAMSOM naturally inherited general features from its global forcing model MPI-ESM, such as the spatial pattern of sea surface variables and their long-term trends. Meanwhile, HAMSOM benefits from its high resolution and the bias correction, in turn, the HAMSOM experiment was more consistent with observations than MPI-ESM especially in terms of salinity distribution, stratification, and boundary current system. The well-known seasonality which is affected by the monsoon system in the BoB was also well reproduced for all related variables. In summary, the HAMSOM result was comprehensively evaluated and proved to be reliable.

By analyzing the two HAMSOM experiments, the following main conclusions were obtained:

- A delayed negative (positive) correlation between the subsurface temperature (salinity) anomaly of the BoB and the Indian Ocean Dipole is revealed, which is proven to be connected by coastal Kelvin waves and westward moving Rossby waves. This analysis demonstrates that the remote forcing from the equatorial Indian Ocean plays a crucial role in the interannual variability of subsurface properties in the BoB. By diagnosing the salinity budget, it is found that the contribution of advection to subsurface salinity variation plays an important role in this delayed correlation.

- Under the RCP8.5 scenario, the overall distribution of sea level height keeps unchanged, but its seasonal variability will be enhanced.
- Under the RCP8.5 scenario, the warming in the BoB shows a spatial difference in its magnitude. For the sea surface, the temperature increase is most significant in the central region and relatively small near the boundaries. The warming rate decreases from the surface to the thermocline depth at about  $100m$ , then increases again up to a depth of approximately  $300m$ . The annual oscillation of temperature at a depth of  $100m$  is more significant than at the surface, reflecting the complicated dynamics at the thermocline. Compared to the climate state of 1981-2009, the sea surface temperature in the BoB will rise by  $2.55$  to  $2.91^{\circ}C$  at the end of the 21st century, while the temperature at a depth of  $100m$  will rise by  $0.39$  to  $1.52^{\circ}C$ . For the sea surface temperature, the enhancement of seasonal changes is most significant in the northern and central basin. In contrast, for the subsurface temperature, the most significant enhancement of seasonal changes occurs in the area affected by the western boundary current.
- Under the RCP8.5 scenario, at the end of the 21st century, the surface seawater will be saltier in the western basin and fresher in the eastern basin, while the subsurface seawater at a depth of  $100m$  will be saltier in the entire basin. The seasonal variability of sea surface salinity exhibits an increasing trend, especially near the estuaries of the Irrawaddy and Salween rivers. In contrast, the seasonal variability of subsurface salinity shows a weakened trend.
- Under the RCP8.5 scenario, the overall spatial pattern of stratification keeps unchanged, but its strength is enhancing and the pycnocline depth is getting shallower in most areas of the BoB. For some areas, the depth of maximum buoyancy frequency even shows a notable jump from the depth of about  $100m$  to about  $30m$  at the end of the 21st century.
- Under the RCP8.5 scenario, the monsoon-controlled seasonal characteristics of the upper ocean circulation in the BoB remains unchanged, but the strength changes. The East Indian Coastal Current will become weaker in winter, its extension in depth will be smaller, and its seasonal variability will also become weaker.
- Under the RCP8.5 scenario, the variabilities of internal coastal Kelvin waves (CKWs) along the BoB coasts show remarkable changes. The occurrence of significant CKWs along the western boundary will become more frequent. The same holds true for the eastern boundary before 2070. In contrast, a decreasing number of significant CKWs is observed for the last 30-year period of the 21st century. The monthly variability of internal CKWs at the BoB eastern boundary exhibits two comparable peaks in the first half of the 21st century but only one significant peak in the second half. The long-term variability of internal CKWs at the BoB western boundary shows a significant upward trend with the occurrence of a jump around the year 2040, which is highly correlated with the local wind speed. By analyzing the correlations between the CKWs and other variables, the results indicate that the intraseasonal variability from the equator is losing influence on the internal CKWs along

the BoB eastern boundary, while the local wind is gaining influence, which is believed to be a consequence of the impact of climate change on stratification.

- By comparing the HAMSOM runs driven by the RCP8.5 scenario and the pre-industrial control scenario, the anthropogenic induced climate variabilities were assessed. The anthropogenic factor was proven to be responsible for the predicted long-term warming in the BoB. It could be shown that the uncertainty of internal variability on the monthly scale is smaller than the predicted seasonal changes of surface/subsurface temperature/salinity under the RCP8.5 scenario, demonstrating that the anthropogenic impact is responsible for the predicted changes in seasonal variabilities.

In summary, the oceanic state in the BoB will be significantly different compared to the current state under the high emissions pathway, especially in terms of temperature and stratification. This in turn affects the propagation of planetary waves such as Kelvin waves, and further affects the connection between the BoB and the equatorial Indian Ocean. It is well studied that the remote forcing from the equatorial Indian Ocean plays an important role for the variability of the BoB on multiple scales. The changes in the CKWs have a potentially dramatic impact on the climate state of the BoB, as well for their mean state as their variability. Meanwhile, the seasonal variations of most other variables also show an increasing trend, implying more extremes in the future. All these changes, whether they refer to long-term trends or seasonal variabilities, have been proven to be mainly induced by anthropogenic factors.

## Acknowledgements

I would like to express the deepest appreciation to Thomas Pohlmann, Bernhard Mayer, and Mihael de Souza. This dissertation would not have been possible without their kind help and valuable discussions. I acknowledge the China Scholarship Council for providing the financial support. The computing support from the DKRZ is also appreciated. In addition, thanks to my family and my girlfriend for their great love and encouragement.

# Bibliography

- Anandh, T. S., Das, B. K., Kuttippurath, J., and Chakraborty, A. (2020). A coupled model analyses on the interaction between oceanic eddies and tropical cyclones over the Bay of Bengal. *Ocean Dynamics*, 70(3):327–337.
- Ashok, K., Guan, Z., Saji, N. H., and Yamagata, T. (2004). Individual and combined influences of ENSO and the Indian Ocean Dipole on the Indian Summer Monsoon. *Journal of Climate*, 17(16):3141–3155.
- Ashok, K., Guan, Z., and Yamagata, T. (2001). Impact of the Indian Ocean Dipole on the relationship between the Indian monsoon rainfall and ENSO. *Geophysical Research Letters*, 28(23):4499–4502.
- Ashok, K., Guan, Z., and Yamagata, T. (2003). A look at the relationship between the ENSO and the Indian Ocean Dipole. *Journal of the Meteorological Society of Japan. Ser. II*, 81(1):41–56.
- Babu, M. T., Sarma, Y. V. B., Murty, V. S. N., and Vethamony, P. (2003). On the circulation in the Bay of Bengal during Northern spring inter-monsoon (March–April 1987). *Deep Sea Research Part II: Topical Studies in Oceanography*, 50(5):855–865.
- Backhaus, J. O. (1985). A three-dimensional model for the simulation of shelf sea dynamics. *Deutsche Hydrografische Zeitschrift*, 38(4):165–187.
- Becker, J. J., Sandwell, D. T., Smith, W. H. F., Braud, J., Binder, B., Depner, J., Fabre, D., Factor, J., Ingalls, S., Kim, S.-H., Ladner, R., Marks, K., Nelson, S., Pharaoh, A., Trimmer, R., Rosenberg, J. V., Wallace, G., and Weatherall, P. (2009). Global bathymetry and elevation data at 30 arc seconds resolution: SRTM30\_PLUS. *Marine Geodesy*, 32(4):355–371.
- Bhat, G. S., Gadgil, S., Hareesh Kumar, P. V., Kalsi, S. R., Madhusoodanan, P., Murty, V. S. N., Prasada Rao, C. V. K., Babu, V. R., Rao, L. V. G., Rao, R. R., Ravichandran, M., Reddy, K. G., Rao, P. S., Sengupta, D., Sikka, D. R., Swain, J., and Vinayachandran, P. N. (2001). BOBMEX: The Bay of Bengal Monsoon Experiment. *Bulletin of the American Meteorological Society*, 82(10):2217–2244.
- Budyko, M. I. (1974). *Climate and Life*. Academic Press.
- Busireddy, N. K. R., Osuri, K. K., Sivareddy, S., and Venkatesan, R. (2018). An observational analysis of the evolution of a mesoscale anti-cyclonic eddy over the Northern Bay of Bengal during May–July 2014. *Ocean Dynamics*, 68(11):1431–1441.

- Chamarthi, S., Ram, P. S., and Josyula, L. (2008). Effect of river discharge on Bay of Bengal circulation. *Marine Geodesy*, 31(3):160–168.
- Chatterjee, A., Shankar, D., McCreary, J. P., Vinayachandran, P. N., and Mukherjee, A. (2017). Dynamics of Andaman Sea circulation and its role in connecting the equatorial Indian Ocean to the Bay of Bengal. *Journal of Geophysical Research: Oceans*, 122(4):3200–3218.
- Chelton, D. B., Schlax, M. G., and Samelson, R. M. (2011). Global observations of nonlinear mesoscale eddies. *Progress in Oceanography*, 91(2):167–216.
- Chen, G., Han, W., Shu, Y., Li, Y., Wang, D., and Xie, Q. (2016). The role of Equatorial Undercurrent in sustaining the Eastern Indian Ocean upwelling. *Geophysical Research Letters*, 43(12):6444–6451.
- Chen, G., Li, Y., Xie, Q., and Wang, D. (2018). Origins of eddy kinetic energy in the Bay of Bengal. *Journal of Geophysical Research: Oceans*, 123(3):2097–2115.
- Chen, G., Wang, D., and Hou, Y. (2012). The features and interannual variability mechanism of mesoscale eddies in the Bay of Bengal. *Continental Shelf Research*, 47:178–185.
- Cheng, X., McCreary, J. P., Qiu, B., Qi, Y., Du, Y., and Chen, X. (2018). Dynamics of eddy generation in the central Bay of Bengal. *Journal of Geophysical Research: Oceans*, 123(9):6861–6875.
- Cheng, X., Xie, S.-P., McCreary, J. P., Qi, Y., and Du, Y. (2013). Intraseasonal variability of sea surface height in the Bay of Bengal. *Journal of Geophysical Research: Oceans*, 118(2):816–830.
- Church, J. A., White, N. J., Konikow, L. F., Domingues, C. M., Cogley, J. G., Rignot, E., Gregory, J. M., van den Broeke, M. R., Monaghan, A. J., and Velicogna, I. (2011). Revisiting the Earth’s sea-level and energy budgets from 1961 to 2008. *Geophysical Research Letters*, 38(18).
- Dandapat, S. and Chakraborty, A. (2016). Mesoscale eddies in the Western Bay of Bengal as observed from satellite altimetry in 1993–2014: Statistical characteristics, variability and three-dimensional properties. *IEEE Journal of Selected Topics in Applied Earth Observations and Remote Sensing*, 9(11):5044–5054.
- Dandapat, S., Gnanaseelan, C., and Parekh, A. (2020). Impact of excess and deficit river runoff on Bay of Bengal upper ocean characteristics using an ocean general circulation model. *Deep Sea Research Part II: Topical Studies in Oceanography*, 172:104714.
- Deser, C., Alexander, M. A., Xie, S.-P., and Phillips, A. S. (2010). Sea surface temperature variability: Patterns and mechanisms. *Annual Review of Marine Science*, 2(1):115–143.
- Deser, C., Phillips, A., Bourdette, V., and Teng, H. (2012). Uncertainty in climate change projections: The role of internal variability. *Climate Dynamics*, 38(3):527–546.
- Döll, P., Kaspar, F., and Lehner, B. (2003). A global hydrological model for deriving water availability indicators: Model tuning and validation. *Journal of Hydrology*, 270(1):105–134.

- Domingues, C. M., Church, J. A., White, N. J., Gleckler, P. J., Wijffels, S. E., Barker, P. M., and Dunn, J. R. (2008). Improved estimates of upper-ocean warming and multi-decadal sea-level rise. *Nature*, 453(7198):1090–1093.
- Durand, F., Shankar, D., Birol, F., and Shenoi, S. S. C. (2009). Spatiotemporal structure of the East India Coastal Current from satellite altimetry. *Journal of Geophysical Research: Oceans*, 114(C2).
- Eigenheer, A. and Quadfasel, D. (2000). Seasonal variability of the Bay of Bengal circulation inferred from TOPEX/Poseidon altimetry. *Journal of Geophysical Research: Oceans*, 105(C2):3243–3252.
- Fadnavis, S. and Chattopadhyay, R. (2017). Linkages of subtropical stratospheric intraseasonal intrusions with Indian Summer Monsoon deficit rainfall. *Journal of Climate*, 30(13):5083–5095.
- Fischer, A. S., Terray, P., Guilyardi, E., Gualdi, S., and Delecluse, P. (2005). Two independent triggers for the Indian Ocean Dipole/Zonal Mode in a Coupled GCM. *Journal of Climate*, 18(17):3428–3449.
- Fofonoff, N. P. and Millard, R. C. (1983). Algorithms for the computation of fundamental properties of seawater. *UNESCO*.
- Friehe, C. A. and Schmitt, K. F. (1976). Parameterization of air-sea interface fluxes of sensible heat and moisture by the bulk aerodynamic formulas. *Journal of Physical Oceanography*, 6(6):801–809.
- Gadgil, S. (2003). The Indian Monsoon and its variability. *Annual Review of Earth and Planetary Sciences*, 31(1):429–467.
- Gill, A. E. (1982). *Atmosphere-Ocean Dynamics*. Academic Press.
- Giorgetta, M. A., Jungclaus, J., Reick, C. H., Legutke, S., Bader, J., Böttinger, M., Brovkin, V., Crueger, T., Esch, M., Fieg, K., Glushak, K., Gayler, V., Haak, H., Hollweg, H.-D., Ilyina, T., Kinne, S., Kornbluh, L., Matei, D., Mauritsen, T., Mikolajewicz, U., Mueller, W., Notz, D., Pithan, F., Raddatz, T., Rast, S., Redler, R., Roeckner, E., Schmidt, H., Schnur, R., Segschneider, J., Six, K. D., Stockhause, M., Timmreck, C., Wegner, J., Widmann, H., Wieners, K.-H., Claussen, M., Marotzke, J., and Stevens, B. (2013). Climate and carbon cycle changes from 1850 to 2100 in MPI-ESM simulations for the Coupled Model Intercomparison Project phase 5. *Journal of Advances in Modeling Earth Systems*, 5(3):572–597.
- Girishkumar, M. S., Ravichandran, M., and Han, W. (2013). Observed intraseasonal thermocline variability in the Bay of Bengal. *Journal of Geophysical Research: Oceans*, 118(7):3336–3349.
- Gleckler, P. J., Santer, B. D., Domingues, C. M., Pierce, D. W., Barnett, T. P., Church, J. A., Taylor, K. E., AchutaRao, K. M., Boyer, T. P., Ishii, M., and Caldwell, P. M. (2012). Human-induced global ocean warming on multidecadal timescales. *Nature Climate Change*, 2(7):524–529.

- Gonaduwage, L. P., Chen, G., McPhaden, M. J., Priyadarshana, T., Huang, K., and Wang, D. (2019). Meridional and zonal eddy-induced heat and salt transport in the Bay of Bengal and their seasonal modulation. *Journal of Geophysical Research: Oceans*, 124(11):8079–8101.
- Good, S. A., Martin, M. J., and Rayner, N. A. (2013). EN4: Quality controlled ocean temperature and salinity profiles and monthly objective analyses with uncertainty estimates. *Journal of Geophysical Research: Oceans*, 118(12):6704–6716.
- Gopalakrishna, V. V., Murty, V. S. N., Sengupta, D., Shenoy, S., and Araligidad, N. (2002). Upper ocean stratification and circulation in the northern Bay of Bengal during southwest monsoon of 1991. *Continental Shelf Research*, 22(5):791–802.
- Gordon, A. L., Shroyer, E., Mahadevan, A., Sengupta, D., and Freilich, M. (2016). Bay of Bengal: 2013 northeast monsoon upper-ocean circulation. *Deep Sea Research Part II: Topical Studies in Oceanography*, 29(2):82–91.
- Gordon, A. L., Shroyer, E., and Murty, V. S. N. (2017). An intrathermocline eddy and a tropical cyclone in the Bay of Bengal. *Scientific Reports*, 7(1):1–8.
- Goswami, B. N. (1987). A mechanism for the west-north-west movement of monsoon depressions. *Nature*, 326(6111):376–378.
- Gouretski, V. and Koltermann, K. P. (2007). How much is the ocean really warming? *Geophysical Research Letters*, 34(1).
- Grinsted, A., Moore, J. C., and Jevrejeva, S. (2004). Application of the cross wavelet transform and wavelet coherence to geophysical time series. *Nonlinear Processes in Geophysics*, 11(5/6):561–566.
- Große, F., Lindemann, C., Pätsch, J., and Backhaus, J. O. (2015). The influence of winter convection on primary production: A parameterisation using a hydrostatic three-dimensional biogeochemical model. *Journal of Marine Systems*, 147:138–152.
- Hacker, P., Firing, E., Hummon, J., Gordon, A. L., and Kindle, J. C. (1998). Bay of Bengal currents during the northeast monsoon. *Geophysical Research Letters*, 25(15):2769–2772.
- Hase, H., Masumoto, Y., Kuroda, Y., and Mizuno, K. (2008). Semiannual variability in temperature and salinity observed by Triangle Trans-Ocean Buoy Network (TRITON) buoys in the eastern tropical Indian Ocean. *Journal of Geophysical Research: Oceans*, 113(C1).
- Hawkins, E. (2011). Our evolving climate: Communicating the effects of climate variability. *Weather*, 66(7):175–179.
- Hawkins, E. and Sutton, R. (2009). The potential to narrow uncertainty in regional climate predictions. *Bulletin of the American Meteorological Society*, 90(8):1095–1108.
- Hersbach, H., Bell, B., Berrisford, P., Hirahara, S., Horányi, A., Muñoz-Sabater, J., Nicolas, J., Peubey, C., Radu, R., Schepers, D., Simmons, A., Soci, C., Abdalla, S., Abellan, X., Balsamo,

- G., Bechtold, P., Biavati, G., Bidlot, J., Bonavita, M., De Chiara, G., Dahlgren, P., Dee, D., Diamantakis, M., Dragani, R., Flemming, J., Forbes, R., Fuentes, M., Geer, A., Haimberger, L., Healy, S., Hogan, R. J., Hólm, E., Janisková, M., Keeley, S., Laloyaux, P., Lopez, P., Lupu, C., Radnoti, G., de Rosnay, P., Rozum, I., Vamborg, F., Villaume, S., and Thépaut, J.-N. (2020). The ERA5 global reanalysis. *Quarterly Journal of the Royal Meteorological Society*, 146(730):1999–2049.
- Howden, S. D. and Murtugudde, R. (2001). Effects of river inputs into the Bay of Bengal. *Journal of Geophysical Research: Oceans*, 106(C9):19825–19843.
- Hunt, K. M. R. and Fletcher, J. K. (2019). The relationship between Indian monsoon rainfall and low-pressure systems. *Climate Dynamics*, 53(3):1859–1871.
- IPCC (2013). Climate Change 2013: The physical science basis. Contribution of Working Group I to the Fifth Assessment Report of the Intergovernmental Panel on Climate Change. *Cambridge University Press, Cambridge, United Kingdom and New York, NY, USA*.
- Jana, S., Gangopadhyay, A., Lermusiaux, P. F. J., Chakraborty, A., Sil, S., and Haley, P. J. (2018). Sensitivity of the Bay of Bengal upper ocean to different winds and river input conditions. *Journal of Marine Systems*, 187:206–222.
- Jensen, T., Wijesekera, H., Nyadjro, E., Thoppil, P., Shriver, J., Sandeep, K., and Pant, V. (2016). Modeling salinity exchanges between the equatorial Indian Ocean and the Bay of Bengal. *Oceanography*, 29(2):92–101.
- Jensen, T. G. (2001). Arabian Sea and Bay of Bengal exchange of salt and tracers in an ocean model. *Geophysical Research Letters*, 28(20):3967–3970.
- Jungclauss, J. H., Fischer, N., Haak, H., Lohmann, K., Marotzke, J., Matei, D., Mikolajewicz, U., Notz, D., and von Storch, J. S. (2013). Characteristics of the ocean simulations in the Max Planck Institute Ocean Model (MPIOM) the ocean component of the MPI-Earth system model. *Journal of Advances in Modeling Earth Systems*, 5(2):422–446.
- Khatiwala, S., Primeau, F., and Hall, T. (2009). Reconstruction of the history of anthropogenic CO<sub>2</sub> concentrations in the ocean. *Nature*, 462(7271):346–349.
- Kido, S. and Tozuka, T. (2017). Salinity variability associated with the positive Indian Ocean Dipole and its impact on the upper ocean temperature. *Journal of Climate*, 30(19):7885–7907.
- Kido, S., Tozuka, T., and Han, W. (2019a). Anatomy of salinity anomalies associated with the positive Indian Ocean Dipole. *Journal of Geophysical Research: Oceans*, 124(11):8116–8139.
- Kido, S., Tozuka, T., and Han, W. (2019b). Experimental assessments on impacts of salinity anomalies on the positive Indian Ocean Dipole. *Journal of Geophysical Research: Oceans*, 124(12):9462–9486.
- Kochergin, V. P. (2013). Three-dimensional prognostic models. In *Three-Dimensional Coastal Ocean Models*, pages 201–208. American Geophysical Union (AGU).

- Köhl, A. (2015). Evaluation of the GECCO2 ocean synthesis: Transports of volume, heat and freshwater in the Atlantic. *Quarterly Journal of the Royal Meteorological Society*, 141(686):166–181.
- Kondo, J. (1975). Air-sea bulk transfer coefficients in diabatic conditions. *Boundary-Layer Meteorology*, 9(1):91–112.
- Krishnamurthy, V. and Goswami, B. N. (2000). Indian Monsoon–ENSO relationship on interdecadal timescale. *Journal of Climate*, 13(3):579–595.
- Krishnamurthy, V. and Shukla, J. (2000). Intraseasonal and interannual variability of rainfall over India. *Journal of Climate*, 13(24):4366–4377.
- Kumar, K. K., Rajagopalan, B., and Cane, M. A. (1999). On the weakening relationship between the Indian Monsoon and ENSO. *Science*, 284(5423):2156–2159.
- Kumar, P. V. H., Kumar, N. M., Shyni, T. N., and Rao, A. R. (2013). Observed variability of thermohaline fields, currents and eddies in the western Bay of Bengal during BOBMEX-99. *Marine Geodesy*, 36(2):219–233.
- Kumar, S. P., Nuncio, M., Narvekar, J., Kumar, A., Sardesai, S., de Souza, S. N., Gauns, M., Ramaiah, N., and Madhupratap, M. (2004). Are eddies nature’s trigger to enhance biological productivity in the Bay of Bengal? *Geophysical Research Letters*, 31(7).
- Kumar, S. P., Nuncio, M., Ramaiah, N., Sardesai, S., Narvekar, J., Fernandes, V., and Paul, J. T. (2007). Eddy-mediated biological productivity in the Bay of Bengal during fall and spring intermonsoons. *Deep Sea Research Part I: Oceanographic Research Papers*, 54(9):1619–1640.
- Kurien, P., Ikeda, M., and Valsala, V. K. (2010). Mesoscale variability along the east coast of India in spring as revealed from satellite data and OGCM simulations. *Journal of Oceanography*, 66(2):273–289.
- Lee, C., Jinadasa, S., Anutaliya, A., Centurioni, L., Fernando, H., Hormann, V., Lankhorst, M., Rainville, L., Send, U., and Wijesekera, H. (2016). Collaborative observations of boundary currents, water mass variability, and monsoon response in the southern Bay of Bengal. *Oceanography*, 29(2):102–111.
- Levitus, S., Antonov, J. I., Boyer, T. P., Baranova, O. K., Garcia, H. E., Locarnini, R. A., Mishonov, A. V., Reagan, J. R., Seidov, D., Yarosh, E. S., and Zweng, M. M. (2012). World ocean heat content and thermosteric sea level change (0–2000 m), 1955–2010. *Geophysical Research Letters*, 39(10).
- Levitus, S., Antonov, J. I., Boyer, T. P., Locarnini, R. A., Garcia, H. E., and Mishonov, A. V. (2009). Global ocean heat content 1955–2008 in light of recently revealed instrumentation problems. *Geophysical Research Letters*, 36(7).
- Li, J., Liang, C., Tang, Y., Liu, X., Lian, T., Shen, Z., and Li, X. (2018). Impacts of the IOD-associated temperature and salinity anomalies on the intermittent equatorial undercurrent anomalies. *Climate Dynamics*, 51(4):1391–1409.

- Li, Y., Han, W., Ravichandran, M., Wang, W., Shinoda, T., and Lee, T. (2017a). Bay of Bengal salinity stratification and Indian summer monsoon intraseasonal oscillation: 1. Intraseasonal variability and causes. *Journal of Geophysical Research: Oceans*, 122(5):4291–4311.
- Li, Y., Han, W., Wang, W., Ravichandran, M., Lee, T., and Shinoda, T. (2017b). Bay of Bengal salinity stratification and Indian summer monsoon intraseasonal oscillation: 2. Impact on SST and convection. *Journal of Geophysical Research: Oceans*, 122(5):4312–4328.
- Lukas, R. and Lindstrom, E. (1991). The mixed layer of the western equatorial Pacific Ocean. *Journal of Geophysical Research: Oceans*, 96(S01):3343–3357.
- Marsland, S. J., Haak, H., Jungclaus, J. H., Latif, M., and Röske, F. (2003). The Max-Planck-Institute global ocean/sea ice model with orthogonal curvilinear coordinates. *Ocean Modelling*, 5(2):91–127.
- Mauritsen, T., Stevens, B., Roeckner, E., Crueger, T., Esch, M., Giorgetta, M., Haak, H., Jungclaus, J., Klocke, D., Matei, D., Mikolajewicz, U., Notz, D., Pincus, R., Schmidt, H., and Tomassini, L. (2012). Tuning the climate of a global model. *Journal of Advances in Modeling Earth Systems*, 4(3).
- Maykut, G. A. and Church, P. E. (1973). Radiation climate of Barrow Alaska, 1962–66. *Journal of Applied Meteorology*, 12(4):620–628.
- McCreary, J. P., Han, W., Shankar, D., and Shetye, S. R. (1996). Dynamics of the East India Coastal Current: 2. Numerical solutions. *Journal of Geophysical Research: Oceans*, 101(C6):13993–14010.
- McCreary, J. P., Kundu, P. K., and Molinari, R. L. (1993). A numerical investigation of dynamics, thermodynamics and mixed-layer processes in the Indian Ocean. *Progress in Oceanography*, 31(3):181–244.
- Meyers, S. D., Kelly, B. G., and O’Brien, J. J. (1993). An introduction to wavelet analysis in oceanography and meteorology: With application to the dispersion of Yanai waves. *Monthly Weather Review*, 121(10):2858–2866.
- Mishra, S. K., Sahany, S., and Salunke, P. (2017). Linkages between MJO and summer monsoon rainfall over India and surrounding region. *Meteorology and Atmospheric Physics*, 129(3):283–296.
- Montégut, C. d. B., Mignot, J., Lazar, A., and Cravatte, S. (2007). Control of salinity on the mixed layer depth in the world ocean: 1. General description. *Journal of Geophysical Research: Oceans*, 112(C6).
- Moore, D. W. and McCreary, J. P. (1990). Excitation of intermediate-frequency equatorial waves at a western ocean boundary: With application to observations from the Indian Ocean. *Journal of Geophysical Research: Oceans*, 95(C4):5219–5231.

- Moss, R. H., Edmonds, J. A., Hibbard, K. A., Manning, M. R., Rose, S. K., van Vuuren, D. P., Carter, T. R., Emori, S., Kainuma, M., Kram, T., Meehl, G. A., Mitchell, J. F. B., Nakicenovic, N., Riahi, K., Smith, S. J., Stouffer, R. J., Thomson, A. M., Weyant, J. P., and Wilbanks, T. J. (2010). The next generation of scenarios for climate change research and assessment. *Nature*, 463(7282):747–756.
- Murty, V. S. N., Sarma, Y. V. B., and Rao, D. P. (1996). Variability of the oceanic boundary layer characteristics in the northern Bay of Bengal during MONTBLEX-90. *Proceedings of the Indian Academy of Sciences - Earth and Planetary Sciences*, 105(1):41.
- Murty, V. S. N., Sarma, Y. V. B., Rao, D. P., and Murty, C. S. (1992). Water characteristics, mixing and circulation in the Bay of Bengal during southwest monsoon. *Journal of Marine Research*, 50:207–228.
- Nuncio, M. and Kumar, S. P. (2012). Life cycle of eddies along the western boundary of the Bay of Bengal and their implications. *Journal of Marine Systems*, 94:9–17.
- Nyadjro, E. S. and McPhaden, M. J. (2014). Variability of zonal currents in the eastern equatorial Indian Ocean on seasonal to interannual time scales. *Journal of Geophysical Research: Oceans*, 119(11):7969–7986.
- Pai, D. S., Bhate, J., Sreejith, O. P., and Hatwar, H. R. (2011). Impact of MJO on the intraseasonal variation of summer monsoon rainfall over India. *Climate Dynamics*, 36(1):41–55.
- Paul, S., Chakraborty, A., Pandey, P. C., Basu, S., Satsangi, S. K., and Ravichandran, M. (2009). Numerical simulation of Bay of Bengal circulation features from ocean general circulation model. *Marine Geodesy*, 32(1):1–18.
- Pettenuzzo, D., Large, W. G., and Pinardi, N. (2010). On the corrections of ERA-40 surface flux products consistent with the Mediterranean heat and water budgets and the connection between basin surface total heat flux and NAO. *Journal of Geophysical Research: Oceans*, 115(C6).
- Pohlmann, T. (1996). Predicting the thermocline in a circulation model of the North sea — part I: Model description, calibration and verification. *Continental Shelf Research*, 16(2):131–146.
- Pohlmann, T. (2006). A meso-scale model of the central and southern North Sea: Consequences of an improved resolution. *Continental Shelf Research*, 26(19):2367–2385.
- Potemra, J. T., Luther, M. E., and O'Brien, J. J. (1991). The seasonal circulation of the upper ocean in the Bay of Bengal. *Journal of Geophysical Research: Oceans*, 96(C7):12667–12683.
- Pramanik, S., Sil, S., Mandal, S., Dey, D., and Shee, A. (2019). Role of interannual equatorial forcing on the subsurface temperature dipole in the Bay of Bengal during IOD and ENSO events. *Ocean Dynamics*, 60:1253–1271.
- Rajeevan, M., Gadgil, S., and Bhate, J. (2010). Active and break spells of the Indian summer monsoon. *Journal of Earth System Science*, 119(3):229–247.

- Rao, R. R., Girish Kumar, M. S., Ravichandran, M., Rao, A. R., Gopalakrishna, V. V., and Thadathil, P. (2010). Interannual variability of Kelvin wave propagation in the wave guides of the equatorial Indian Ocean, the coastal Bay of Bengal and the southeastern Arabian Sea during 1993–2006. *Deep Sea Research Part I: Oceanographic Research Papers*, 57(1):1–13.
- Rao, R. R. and Sivakumar, R. (2000). Seasonal variability of near-surface thermal structure and heat budget of the mixed layer of the tropical Indian Ocean from a new global ocean temperature climatology. *Journal of Geophysical Research: Oceans*, 105(C1):995–1015.
- Roemmich, D. and Gilson, J. (2009). The 2004–2008 mean and annual cycle of temperature, salinity, and steric height in the global ocean from the Argo Program. *Progress in Oceanography*, 82(2):81–100.
- Rydbeck, A. V., Jensen, T. G., and Flatau, M. (2019). Characterization of intraseasonal Kelvin waves in the equatorial Pacific Ocean. *Journal of Geophysical Research: Oceans*, 124(3):2028–2053.
- Saji, N. H., Goswami, B. N., Vinayachandran, P. N., and Yamagata, T. (1999). A dipole mode in the tropical Indian Ocean. *Nature*, 401(6751):360–363.
- Sanchez-Franks, A., Webber, B. G. M., King, B. A., Vinayachandran, P. N., Matthews, A. J., Sheehan, P. M. F., Behara, A., and Neema, C. P. (2019). The railroad switch effect of seasonally reversing currents on the Bay of Bengal high-salinity core. *Geophysical Research Letters*, 46(11):6005–6014.
- Sato, T. and Kimura, F. (2007). How does the Tibetan Plateau affect the transition of Indian monsoon rainfall? *Monthly Weather Review*, 135(5):2006–2015.
- Schott, F. A. and McCreary, J. P. (2001). The monsoon circulation of the Indian Ocean. *Progress in Oceanography*, 51(1):1–123.
- Schott, F. A., Xie, S.-P., and McCreary, J. P. (2009). Indian Ocean circulation and climate variability. *Reviews of Geophysics*, 47(1).
- Seo, H., Subramanian, A. C., Song, H., and Chowdary, J. S. (2019). Coupled effects of ocean current on wind stress in the Bay of Bengal: Eddy energetics and upper ocean stratification. *Deep Sea Research Part II: Topical Studies in Oceanography*, 168:104617.
- Shankar, D., McCreary, J. P., Han, W., and Shetye, S. R. (1996). Dynamics of the East India Coastal Current: 1. Analytic solutions forced by interior Ekman pumping and local alongshore winds. *Journal of Geophysical Research: Oceans*, 101(C6):13975–13991.
- Shankar, D., Vinayachandran, P. N., and Unnikrishnan, A. S. (2002). The monsoon currents in the north Indian Ocean. *Progress in Oceanography*, 52(1):63–120.
- Shetye, S. R., Gouveia, A. D., Shankar, D., Shenoi, S. S. C., Vinayachandran, P. N., Sundar, D., Michael, G. S., and Nampoothiri, G. (1996). Hydrography and circulation in the western Bay of Bengal during the northeast monsoon. *Journal of Geophysical Research: Oceans*, 101(C6):14011–14025.

- Shetye, S. R., Gouveia, A. D., Shenoi, S. S. C., Sundar, D., Michael, G. S., and Nampoothiri, G. (1993). The western boundary current of the seasonal subtropical gyre in the Bay of Bengal. *Journal of Geophysical Research: Oceans*, 98(C1):945–954.
- Shetye, S. R., Shenoi, S. S. C., Gouveia, A. D., Michael, G. S., Sundar, D., and Nampoothiri, G. (1991). Wind-driven coastal upwelling along the western boundary of the Bay of Bengal during the southwest monsoon. *Continental Shelf Research*, 11(11):1397–1408.
- Shroyer, E. L., Gordon, A. L., Jaeger, G. S., Freilich, M., Waterhouse, A. F., Farrar, J. T., Sarma, V. V. S. S., Venkatesan, R., Weller, R. A., Moum, J. N., and Mahadevan, A. (2020). Upper layer thermohaline structure of the Bay of Bengal during the 2013 northeast monsoon. *Deep Sea Research Part II: Topical Studies in Oceanography*, 172:104630.
- Siegismund, F. and Schrum, C. (2001). Decadal changes in the wind forcing over the North Sea. *Climate Research*, 18(1-2):39–45.
- Sikka, D. R. and Gadgil, S. (1980). On the maximum cloud zone and the ITCZ over Indian longitudes during the southwest monsoon. *Monthly Weather Review*, 108(11):1840–1853.
- Sinha, N., Chattopadhyay, R., and Chakraborty, S. (2019). Bay of Bengal branch of Indian summer monsoon and its association with spatial distribution of rainfall patterns over India. *Theoretical and Applied Climatology*, 137(3):1895–1907.
- Sprintall, J. and Tomczak, M. (1992). Evidence of the barrier layer in the surface layer of the tropics. *Journal of Geophysical Research: Oceans*, 97(C5):7305–7316.
- Sreenivas, P., Gnanaseelan, C., and Prasad, K. V. S. R. (2012). Influence of El Niño and Indian Ocean Dipole on sea level variability in the Bay of Bengal. *Global and Planetary Change*, 80-81:215–225.
- Stevens, B., Giorgetta, M., Esch, M., Mauritsen, T., Crueger, T., Rast, S., Salzmann, M., Schmidt, H., Bader, J., Block, K., Brokopf, R., Fast, I., Kinne, S., Kornbluh, L., Lohmann, U., Pincus, R., Reichler, T., and Roeckner, E. (2013). Atmospheric component of the MPI-M Earth System Model: ECHAM6. *Journal of Advances in Modeling Earth Systems*, 5(2):146–172.
- Swanson, K. L., Sugihara, G., and Tsonis, A. A. (2009). Long-term natural variability and 20th century climate change. *Proceedings of the National Academy of Sciences of the United States of America*, 106(38):16120–16123.
- Taylor, K. E. (2001). Summarizing multiple aspects of model performance in a single diagram. *Journal of Geophysical Research: Atmospheres*, 106(D7):7183–7192.
- Thakur, R., Shroyer, E. L., Govindarajan, R., Farrar, J. T., Weller, R. A., and Moum, J. N. (2019). Seasonality and buoyancy suppression of turbulence in the Bay of Bengal. *Geophysical Research Letters*, 46(8):4346–4355.

- Todd, R. E. (2020). Equatorial circulation in the western Indian Ocean during onset of the 2018 summer monsoon and links to the Bay of Bengal. *Geophysical Research Letters*, 47(10):e2020GL087215.
- Torrence, C. and Compo, G. P. (1998). A practical guide to wavelet analysis. *Bulletin of the American Meteorological Society*, 79(1):61–78.
- Torrence, C. and Webster, P. J. (1999). Interdecadal changes in the ENSO–Monsoon system. *Journal of Climate*, 12(8):2679–2690.
- Trott, C. B., Subrahmanyam, B., Murty, V. S. N., and Shriver, J. F. (2019). Large-Scale Fresh and Salt Water Exchanges in the Indian Ocean. *Journal of Geophysical Research: Oceans*, 124(8):6252–6269.
- van Vuuren, D. P., Edmonds, J., Kainuma, M., Riahi, K., Thomson, A., Hibbard, K., Hurtt, G. C., Kram, T., Krey, V., Lamarque, J.-F., Masui, T., Meinshausen, M., Nakicenovic, N., Smith, S. J., and Rose, S. K. (2011). The representative concentration pathways: An overview. *Climatic Change*, 109(1):5.
- Varkey, M., Murty, V., and Suryanarayana, A. (1996). Physical oceanography of the Bay of Bengal and Andaman Sea. *Oceanography and Marine Biology*, 34:1–70.
- Vecchi, G. A. and Harrison, D. E. (2002). Monsoon breaks and subseasonal sea surface temperature variability in the Bay of Bengal. *Journal of Climate*, 15(12):1485–1493.
- Vidya, P. J. and Kumar, S. P. (2013). Role of mesoscale eddies on the variability of biogenic flux in the northern and central Bay of Bengal. *Journal of Geophysical Research: Oceans*, 118(10):5760–5771.
- Vinayachandran, P. N. and Kurian, J. (2007). Hydrographic observations and model simulation of the Bay of Bengal freshwater plume. *Deep Sea Research Part I: Oceanographic Research Papers*, 54(4):471–486.
- Vinayachandran, P. N., Masumoto, Y., Mikawa, T., and Yamagata, T. (1999). Intrusion of the Southwest Monsoon Current into the Bay of Bengal. *Journal of Geophysical Research: Oceans*, 104(C5):11077–11085.
- Vinayachandran, P. N., Murty, V. S. N., and Babu, V. R. (2002). Observations of barrier layer formation in the Bay of Bengal during summer monsoon. *Journal of Geophysical Research: Oceans*, 107(C12):SRF 19–1–SRF 19–9.
- Vinayachandran, P. N., Shetye, S. R., Sengupta, D., and Gadgil, S. (1996). Forcing mechanisms of the Bay of Bengal circulation. *Current Science*, 71(10):753–763.
- Wang, B., Wu, R., and Lau, K.-M. (2001). Interannual variability of the Asian Summer Monsoon: Contrasts between the Indian and the Western North Pacific–East Asian Monsoons. *Journal of Climate*, 14(20):4073–4090.

- Webster, P. J., Moore, A. M., Loschnigg, J. P., and Leben, R. R. (1999). Coupled ocean–atmosphere dynamics in the Indian Ocean during 1997–98. *Nature*, 401(6751):356–360.
- Webster, P. J. and Yang, S. (1992). Monsoon and ENSO: Selectively interactive systems. *Quarterly Journal of the Royal Meteorological Society*, 118(507):877–926.
- Wijesekera, H. W., Jensen, T. G., Jarosz, E., Teague, W. J., Metzger, E. J., Wang, D. W., Jinadasa, S. U. P., Arulananthan, K., Centurioni, L. R., and Fernando, H. J. S. (2015). Southern Bay of Bengal currents and salinity intrusions during the northeast monsoon. *Journal of Geophysical Research: Oceans*, 120(10):6897–6913.
- Wu, R., Chen, J., and Chen, W. (2012). Different types of ENSO influences on the Indian summer monsoon variability. *Journal of Climate*, 25(3):903–920.
- Yu, L., O’Brien, J. J., and Yang, J. (1991). On the remote forcing of the circulation in the Bay of Bengal. *Journal of Geophysical Research: Oceans*, 96(C11):20449–20454.
- Zheng, X.-T., Xie, S.-P., Du, Y., Liu, L., Huang, G., and Liu, Q. (2013). Indian Ocean Dipole response to global warming in the CMIP5 multimodel ensemble. *Journal of Climate*, 26(16):6067–6080.